INVESTIGATIONS ON STRUCTURAL AND TRANSPORT PROPERTIES OF MIXED OXIDE SYSTEMS

THESIS

Submitted to the
Saurashtra University, Rajkot

For
The Degree of

Doctor of Philosophy

in Science

In the subject of **Physic**s

By

Rayaprol Sudhindra

Under the supervision of
Dr. D. G. Kuberkar
M.Sc., Ph.D.

DEPARTMENT OF PHYSICS
SAURASHTRA UNIVERSITY
RAJKOT – 360 005
INDIA

SEPTEMBER - 2002

Dedicated to my beloved parents and family...

Acknowledgements

"Right knowledge is the supreme purifier, the greatest secret of all the Vedas and gods"
His Holiness Adi Sankaracharya

It gives me immense pleasure to express my gratitude to my research guide and guru ***Dr. D. G. KUBERKAR****. His words of motivation have been my source of inspiration, both in academic as well as in personal life. Working with him, has indeed helped me to mature both as a student and person.*

My sincere regards to Prof. R. G. KULKARNI, Prof. B. S. SHAH & Prof. K. N. IYER, who in their capacity as Heads of Department, during the tenure of this work have been very helpful in extending the departmental facilities to me. I also wish to extend my acknowledgements to all the faculty members of the Department of Physics for their moral support.

I also thank IUC-DAEF and Dr. P.S.GOYAL, for providing financial support to me in the form of Project Assistantship, during the entire course of this work. I also wish to thank Dr. M. RAMANADHAM, Dr. S. K. PARANJAPE and Ms. KEKA R. CHAKRAVORTY, my project collaborators, for their invaluable cooperation and help in carrying out neutron diffraction measurements and analysis at Dhruva Reactor, BARC. Acknowledgements are also due to Prof. R. PINTO (Chairman), Prof. S. K. MALIK and group members of CMP & MS Division, TIFR namely Mr. J. JOHN, Mr. NILESH KULKARNI and Mr. R. SANNABHATI for their help in carrying out thin film deposition and characterizations at TIFR.

I am very much indebted to DR. S. I. PATIL, Department of Physics, University of Pune, Pune for his timely help in the time of crisis. I am also thankful to Dr. K. P. ADHI, Dr. ARUN BANPURKAR, Mr. MANDAR SAHASRABUDHE, Mr. PANKAJ SAGDEO and Mr. S. SADAKALE. Their cooperation and hospitality made my stay at Pune a memorable one.

My sincere thanks to Dr. LACHLAN M. D. CARNSWICK (IUCr) and Dr. CHENG DONG (Beijing University, China) for providing me with latest softwares for carrying out structural analysis. These softwares have been very useful for me and all the group members at our department.

I thank Mr. SHOVIT BHATTACHARYA and Mr. MANGLESH DIXIT for their help in carrying out resistivity measurements on few samples.

I feel very fortunate for having a faithful domain of die-hard friends. I have all reasons to acknowledge the efforts of my best friends, Mr. ACHYUT RAM MURTHY (ICICI, Mumbai) and Ms. ANJANA DOGRA (NSC, New Delhi). Their timely help and encouraging words kept my morale high and sailed me through difficult times. I also thank my former classmates for inspiring me to go for higher studies.

I sincerely appreciate the cooperation of my research colleagues, Mr. C. M. THAKER, Ms. KRUSHNA MAVANI and Mr. D. S. RANA. It has been a memorable time working with them.

I acknowledge my seniors Dr. N. A. SHAH, Dr. B. T. SAVALIA, Dr. R. S. THAMPI, Dr. KALPESH JANI, and my colleagues Mr. DARSHAN KUNDALIYA, Ms. REETA VIJ, Mr. NILAY PANCHASARA, Mr. SUKESH LAGHATE, Mr. RAVI JADHAV, Mr. NIRAJ PANDYA, Mr. UDAY TRIVEDI and Ms. MANISHA CHANTBAR for their friendly help and advice.

My acknowledgements are also due to Mrs. PREETI D. KUBERKAR and Ms. MADHURA KUBERKAR. I sincerely thank them for the homely reception and hospitality given to me.

I feel short of words when I put on record the efforts of my family members in supporting me throughout these years with all the hardships they have faced for me. My heartfelt regards to my parents, my brothers and sisters, without whom this day would not have been possible. I wish to thank my mother Mrs. JANAKI and my father Mr. R. VISWANATH SARMA for bearing my nuisance yet comforting and supporting me during the entire duration of my Ph.D work.

"End of one story is the beginning of a new one…."

Rajkot *(Sudhindra Rayaprol)*

September 2002.

INDEX

INDEX

CHAPTER – II ***Synthesis and Experimental characterization of the HTSC materials***

INDEX

CHAPTER – III ***Characterization methods used***

INDEX

CHAPTER – IV ***Studies on $La_{2-x}Dy_xCa_yBa_2Cu_{4+y}O_z$ system***

INDEX

CHAPTER – V ***Studies on Pr and Mo substituted La – 2125 system***

Abstract

Since the discovery of the phenomenon of Superconductivity in 1911 by Kammerling Onnes, tremendous efforts have been put in by various scientists around the world, in understanding this unusual property and also in developing new compounds. Several theories were put forward for explaining the mechanism and properties of superconductivity in elements and alloys. But since the transition temperature (T_c) of these elements was less, the endeavor to increase the T_c up to room temperature persisted. A major breakthrough in these efforts came with the discovery of superconductivity in oxide compounds ($La_{2-x}A_xCuO_4$) in 1986. The dream of applying superconductors to reap their potential benefits received a major boost with the discovery of superconductivity in $YBa_2Cu_3O_z$ (Y-123) compounds with transition temperature around 90K, above the boiling point of easily available liquid nitrogen (77 K). The interest in studying oxides grew by many folds because of the reason that the properties of oxides can be tailor made to specific roles by altering the synthesis methods. But till date, there is no such clear-cut explanation for the "Superconductivity" in these high T_c compounds. Several efforts are made to understand the mechanism responsible for superconductivity phenomenon in high T_c superconductors.

An attempt has been made in the present work to focus on the investigations on the structural, transport and magnetic properties of Lanthanum based 2125 type mixed oxide superconductors. This system is derived from the tetragonal RE-123 type superconductors. Due to the interesting properties exhibited by the La-2125 type tetragonal superconductors, an attempt has been made to investigate the role of dopants in

modifying the superconducting properties of these compounds and to establish a structure – property correlation in them.

The thesis highlights the studies on rare earth doping at La site in $La_{2-x}RE_xCa_yBa_2Cu_{4+y}O_z$ [La-2125 for RE = Pr, Dy] system and metal ion doping at Cu site in $La_{1.5}Nd_{0.5}Ca_1Ba_2(Cu_{1-x}Mo_x)_5O_z$ system, in order to understand the structural, transport and magnetic properties of system studied. A comparative study between RE-123 and La-2125 system has been carried out to understand and explore the mechanism of superconductivity in these mixed oxide systems.

The major part of the thesis deals with the structural studies carried out on La-2125 type compounds using X-ray diffraction (XRD) and Neutron Diffraction (ND) measurements and the detailed analysis of the observed data by using Rietveld refinement method. The Rietveld analysis was done by assuming a tetragonal Y-123 structure with P 4 / MMM space group. All the samples fit well into this structure and confirm single-phase tetragonal structure.

The other aspect of carrying out detailed study on the superconducting properties of La-2125 system, apart from the polycrystalline bulk samples, is the study of superconducting properties in thin film form. The thesis introduces the synthesis of thin films of $La_{2-x}Dy_xCa_yBa_2Cu_{4+y}O_z$ system using the Pulsed Laser Deposition (PLD) technique. PLD is an extremely simple and probably the simplest among all the thin film growth techniques. It is such a versatile technique that with the choice of an appropriate laser, it can be used to grow thin films of any kind of material. The thin films were grown on $LaAlO_3$ single crystal substrates.

The results obtained on various La-based 2125 systems using various techniques provide a wealth of information regarding various properties of the system under investigations. Various techniques have been used to understand the structural, morphological, transport and magnetic properties of the La-2125 and doped La-2125 systems.

Chapter 1 – 3 introduces to superconductivity, synthesis and characterization techniques, experimental tools used in the present work. **Chapter 4** deals with the "***Structural and superconducting property studies on $La_{2-x}Dy_xCa_yBa_2Cu_{4+y}O_z$ system – Bulk and thin film form".*** It is a proven fact that the superconductivity in RE-123 superconductors is governed by the oxygen content which in turn is responsible for the carrier concentration in the system. Due to the oxygen dependent property, RE-123 superconductors undergo structural phase transformation from orthorhombic to tetragonal as a function of oxygen content. It would be interesting to obtain a stable, tetragonal oxygen independent superconductor having dependence of its carrier concentration and T_c on the nature and amount of the substituted cation. Keeping this in mind, an attempt was made to synthesize a La-based mixed oxide superconductor by adding equal amounts of CaO and CuO to a non-superconducting, anti-ferromagnetic $La_2Ba_2Cu_4O_z$ (La-224) system. The resultant stoichiometric composition $La_{2-x}Dy_xCa_yBa_2Cu_{4+y}O_z$ [LaDyCaBCO], where y = 2x; x = 0.1 – 0.5, shows a maximum T_c ~ 75K. The selection of rare earth Dy^{3+} ion has been made due to its strong magnetic moment and large neutron scattering length as compared to La^{3+} ion.

The detailed structural investigations on polycrystalline LaDyCaBCO system were carried out using XRD and ND techniques. The Rietveld analysis of the XRD and

ND data shows interesting results regarding the site occupancies of various dopants at La and Ba sites. The superconducting property measurements using d.c. resistivity, a.c. & d.c. susceptibility and d.c. magnetization measurement show a strong dependence of T_c on the hole concentration in conducting CuO_2 sheets. The Ca-doping plays an important role in "turning on" of superconductivity into this system. The morphological studies on all the bulk samples studied using SEM techniques show the modification in the grain microstructure.

From application point of view, it is preferred to obtain the stable thin films of presently studied La-2125 mixed oxide superconductors. For this purpose, the superconducting thin films of LaDyCaBCO were synthesized for the first time using PLD technique. Due to the stochiometric variation from RE-123, it has been found that the experimental conditions and deposition parameters for the synthesis of La-2125 thin films using PLD technique are different. The thin films of La-2125 materials grown on $LaAlO_3$ substrate were characterized for their structural, morphological, electrical and magnetic properties using XRD, AFM, d.c. resistivity, d.c. susceptibility and d.c. magnetization measurements.

Chapter 5 is devoted to two systems, namely the LaPrCaBCO (Pr doped) and LaNdCaBCMoO (Mo doped) systems.

Structural studies on $La_{2-x}Pr_xCa_yBa_2Cu_{4+y}O_z$ system

Pr-123 is a non-superconductor with non-metallic nature. But there is marked difference in the properties of Pr-123 and Pr doped 123 systems. In Pr doped RE-123 systems ($RE_{1-x}Pr_xBa_2Cu_3O_z$) the superconducting transition temperature decreases linearly with increasing Pr concentration and for a critical Pr concentration the

superconductivity is completely quenched. Also, for a given critical Pr concentration in $RE_{1-x}Pr_xBa_2Cu_3O_z$, T_c decreases linearly with increasing radius of RE^{3+} ion.

In order to understand the role of Pr in influencing the structural and superconducting properties in the La-2125 system, an attempt is made to study $La_{2-x}Pr_xCa_yBa_2Cu_{4+y}O_z$,; x = 0.1 – 0.5; y = 2x system using XRD, d.c. resistivity, and d.c. susceptibility measurements. An interesting observation made is that, the results of Pr doped RE-123 system are different from those obtained for Pr doped La-2125 system. The detailed structural and site occupancy studies were done by the analysis of X-ray data using Rietveld refinement method.

Studies on the $La_{1.5}Nd_{0.5}Ca_1Ba_2(Cu_{1-x}Mo_X)_5O_z$ & $La_{1.5-y}Nd_{0.5}Ca_{1+y}Ba_2(Cu_{0.8}Mo_{0.2})_5O_z$ systems

Cu - O layers (planes and chains) play a vital role in inducing superconductivity in these mixed oxide compounds. Due to their vital role only, these superconductors are also called 'Cuprate' superconductors. It has been observed in La-2125 system that superconductivity depends on the number of holes in the copper oxide (CuO_2) planes and not on the oxygen content. The correlation between the hole concentration in sheets (p_{sh}) and T_c has been established. The difference in rate of suppression of T_c due to Mo-doping at Cu site in RE-123 and La-2125 system can be attributed to more number of Cu-O layers and the possibility of different charge transport mechanism in La-2125 system. The Mo substitution at Cu-sites also contributes in creating pinning centers in the structure, which helps in enchancing current density up to lower Mo-doping concentration.

Unlike the role of Ca-doping in reviving the superconductivity of RE - 123 system, in La - 2125, increasing Ca content in the form

$$La_{1.5-y}Nd_{0.5}Ca_{1+y}Ba_2[Cu_{0.8}Mo_{0.2}]_5O_z$$

does not help in reviving the T_c of Mo doped La - 2125 system. This prompts us to propose that the stoichiometric composition

$$La_{1.5}Nd_{0.5}Ca_1Ba_2Cu_5O_z$$

has an optimum level of hole concentration due to the doping of Ca and further increase in Ca content to Ca_{1+y} leads to excess hole doping thereby resulting into no change in the superconducting properties. The above system has been studied by XRD, d.c. resistivity, d.c. magnetization, d.c. susceptibility and iodometric double titration methods.

List of Publications in International / National Journals

1] *Superconducting and Hole Concentration of $La_{2-x}R_xBa_2Ca_yCu_{4+y}O_z$; R = Nd, Gd; y = 2x system*
D. G. Kuberkar, R. S. Thampi, N. A. Shah, Krushna Mavani,
S. Rayaprol, S. K. Malik, W. B. Yelon, R. G. Kulkarni
Journal of Applied Physics, **89**, 11, (2001)

2] *Effect of Sr-substitution on the restitution of superconductivity in Pr-substitution at rare earth and Ba-site in $EuBa_2Cu_3O_z$*
R. S. Thampi, **S. Rayaprol**, Krushna Mavani, D. G. Kuberkar,
M. R. Gonal, Ram Prasad, R. G. Kulkarni
Physica C **355**, 23, (2001)

3] *Effect of hole filling by Co and hole doping by Ca on the superconductivity of $GdBa_2Cu_3O_{7-\delta}$*
D.G. Kuberkar, Nikesh A. Shah, R.S. Thampi, **S. Rayaprol**,
M.R. Gonal, Ram Prasad, R.G. Kulkarni
Int. Jour. of Inorg. Mat. **3,** 59, (2001)

4] *Structural Investigations of La-2125 mixed oxide superconducting system*
S. Rayaprol, Krushna Mavani, D. S. Rana, C. M. Thaker, R. S. Thampi, D.G. Kuberkar, S.K. Malik and R. G. Kulkarni
J. of. Supercond. **15** (No. 3) 211 (2002)

5] *Structural studies and T_c dependence in $La_{2-x}Dy_xBa_2Ca_yCu_{4+y}O_z$ type mixed oxide superconductors*
S. Rayaprol, Krushna Mavani, C.M. Thaker, D.S. Rana,
Nilesh A. Kulkarni, Keka Chakravorty, S.K. Paranjape,
M. Ramnadham and D.G. Kuberkar
Pramana - Journal of Physics, **58** (No. 5 & 6), 877 (2002)

6] *Effect of Pr-Ca substitution on the transport and magnetic behavior of $LaMnO_3$ perovskite*
C.M. Thaker, **S. Rayaprol**, Krushna Mavani, D.S. Rana,
M. Sahasrabudhe, S.I. Patil and D.G. Kuberkar
Pramana - Journal of Physics, **58** (No. 5 & 6), 1035 (2002)

7] *Superconductivity in $La_{2-x}R_xBa_2Ca_yCu_{4+y}O_z$; R=Nd & Gd, y=2x systems*
R.S. Thampi, Nikesh A. Shah, **S. Rayaprol**, D.G. Kuberkar,
S.K. Malik, W.B. Yelon, M.R. Gonal, Ram Prasad and R.G. Kulkarni
Communicated to Physica B

8] *Superconductivity in La-2125 mixed oxide thin films*
S. Rayaprol, Krushna Mavani, C. M. Thaker, D.S. Rana, J. John, Nilesh A. Kulkarni, R. Pinto, D.G. Kuberkar and R.G. Kulkarni
Physica C (In press)

9] *Effect of Sr-substitution at Eu and Ba sites on the Superconductivity in* $Eu(Ba_{2-x}Pr_x)Cu_3O_z$ *system*
R. S. Thampi, D.G. Kuberkar, **S. Rayaprol**, C.M. Thaker, M.R. Gonal, Ram Prasad and R.G. Kulkarni
Solid State Physics (India) **42**, 453, (1999)

10] *Effect of Mo-substitution on the superconductivity in La-2125 perovskite system*
S. Rayaprol, Krushna Mavani, R. S. Thampi, C. M. Thaker, D. G. Kuberkar, R. G. Kulkarni
Solid State Physics (India) **43**, 384, (2000)

11] *Revival of* T_c *by Ca doping at Y site in* $YBa_2(Cu_{1-x}Zn_x)_3O_{7-\delta}$
Krushna Mavani, **S. Rayaprol**, D.S. Rana, C. M. Thaker, S. K. Paghdar, R. Nagarajan, Nilesh. A. Kulkarni & D.G. Kuberkar
Solid State Physics (India) Vol. **44** (In press)

12] *Anomalous behavior in* $Y_{0.8}Mo_{0.2}MnO_3$ *system*
C.M. Thaker, D.S. Rana, Krushna Mavani, **S. Rayaprol**, M. Sahasrabudhe, S. I. Patil, Nilesh. A. Kulkarni & D.G. Kuberkar
Solid State Physics (India) Vol. **44** (In press)

CHAPTER - I

Superconductivity – an overview

1.1 INTRODUCTION

Superconductors, the materials do not possess resistance to the flow of charge carriers, are one of the last great frontiers of scientific discovery. Dutch physicist, Heike Kammerlingh Onnes, discovered "Superconductivity" in 1911, three years after he successfully liquefied Helium gas [1]. This discovery has lot to do with the advances in low-temperature refrigeration during 19^{th} century. It had been known for many years that, the resistance of metals fell when cooled below room temperature, but it was not known what limiting value the resistance would approach, if the temperatures were reduced to very close to 0 K. Some scientists, such as William Kelvin, believed that electrons flowing through a conductor would come to a complete halt as the temperature approached zero. But other scientists, including Onnes, felt that a cold wire's resistance would dissipate. This suggested that there would be a steady decrease in electrical resistance allowing for better conduction of electricity. At some very low temperature there would be a leveling off as the resistance reached some ill-defined minimum value allowing the current to flow with little or no resistance.

In 1911, Onnes began to investigate the electrical properties of metals in extremely cold temperatures. He passed a current through a very pure mercury wire and measured its resistance as he steadily lowered the temperature [2]. There was no leveling off of resistance nor was any stopping of electrons as suggested by Kelvin. At 4.2 K the resistance suddenly vanished. Current was flowing through the mercury wire and nothing was stopping it, resistance was "ZERO" (Figure 1.1).

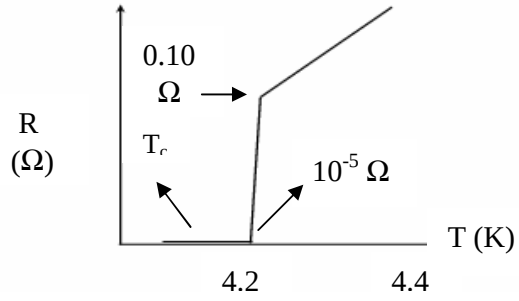

Figure 1.1 Vanishing of resistance at critical temperature (T_c) for Hg metal

According to Onnes, "*Mercury has passed into a new state, which on account of its extraordinary electrical properties may be called the* ***superconducting state****"*. The temperature (4.2 K) at which the transition from normal metal to superconducting state took place was called the "***transition temperature****"*. Onnes and other scientists started to test other metals also and found that many of them behaved in the same manner when at extremely cold temperature. An electrical conductor with no resistance could carry current to any distance with no losses. In one of the Onnes experiment he started a current flowing through a loop of lead of wires cooled to 4 K. A year later the current was still flowing without significant current loss. Onnes found that the superconductors exhibited what he called "***persistent currents***", electric currents that continued to flow without an electric potential driving them. Onnes was awarded Nobel Prize in 1913 for his discovery of "***Superconductivity***".

The important signatures of a superconductor can be highlighted as:

a) **Zero Resistance**: Superconductors offer almost zero resistance to the flow of current below its transition temperature. The benefit of superconductors over other conductors is that they will not generate any heat.

b) **Perfect Diamagnetism**: A superconductor will not allow a magnetic field to penetrate its interior. It causes currents to flow that generate a magnetic field inside the superconductor which just balances the field that would have otherwise penetrated the material. This effect is called the "***Meissner Effect"*** after Walther Meissner and R. Ochsenfeld made this discovery in superconductors [3].

1.2 CONVENTIONAL AND HIGH T_C SUPERCONDUCTORS (HTSC)

Superconductors are classified as either conventional (**Type I & Type II**) or high T_c superconductors on the basis of their response to the applied magnetic field, the former applying to the original elemental and alloy superconductors and the later referring to the mixed oxide compounds such as Yttrium Barium Cuprate. In a very weak magnetic field both the types of superconductors act in similar fashion i.e., they both expel the field entirely. Differences appear when the applied field is made stronger. Figures 1.2 (a) and (b) clearly shows this difference [4].

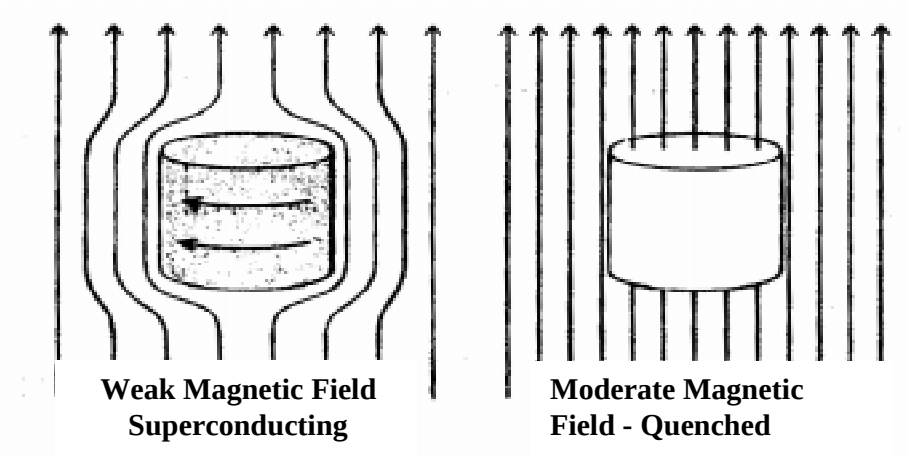

Figure 1.2 (a) In Type I superconductor the currents collapse when the field is raised to a moderate intensity, usually less than 0.1 Tesla; the field then penetrates the metal and the superconductivity is abolished.

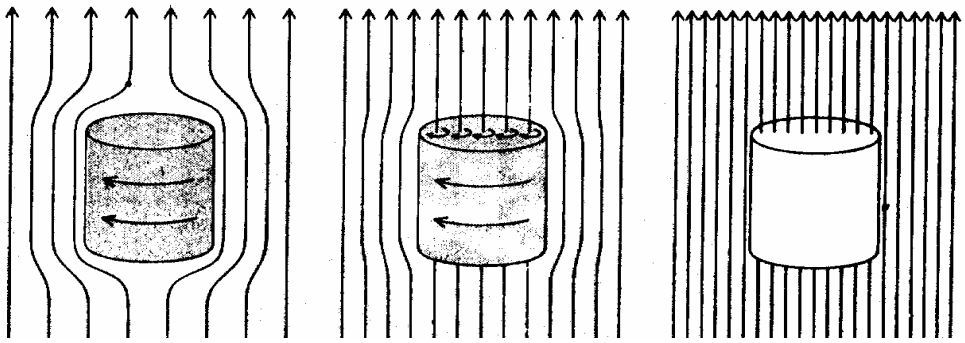

Figure 1.2 (b) In Type II superconductors, the quanta of magnetic flux begin to enter at a moderate field but are isolated from the surrounding superconductive regions by vortical supercurrents. The last trace of superconductivity is not eliminated until the field reaches a higher-level.

a) ***Type - I Superconductors***: This category of superconductors mainly comprises of pure metals that normally show some conductivity at room temperature. They require incredible cold to slow down molecular vibrations sufficiently to facilitate unimpeded electron flow in accordance with what is known as BCS theory. They have one critical magnetic field for any given temperature. If they are in a magnetic field that is weaker than the critical magnetic field, they have zero resistance and show perfect diamagnetism. Figure 1.3 (a) shows the magnetic behavior of Type I superconductors under the applied external field.

If the magnetic field is stronger than the critical magnetic field, resistance is greater than zero, and there is flux penetration. These superconductors are characterized by a very sharp transition to a superconducting state and by "***perfect diamagnetism***". The Table 1.1 gives a list of some of the known Type I superconductors.

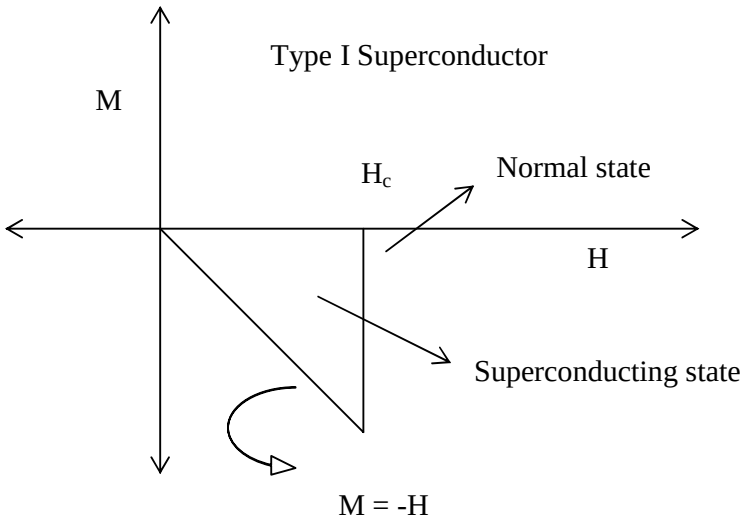

Figure 1.3 (a) ***Plot of induced magnetic field (M) inside a Type I superconductor as a function of the external applied field (H)*** [5]***.***

Table 1.1 ***Some reported Type I and Type II conventional Superconductors***

Element	**T_c (^{0}K)**	**Element**	**T_c (^{0}K)**
Technetium	7.8	Lead	7.2
Lanthanum	4.9	Tantalum	4.47
Mercury	4.15	Tin	3.72
Indium	3.40	Rhenium	1.697
Thallium	1.70	Thorium	1.38
Aluminium	1.175	Zinc	0.85
TiZr	1.5	NbTi	9.5
Zr_3Bi	3.4	Nb_3Ge	23.2
$CaIr_2$	6.2	NbN	17
UPt_3	0.43	$LiTi_2O_4$	13.7
$CuRh_2Se_4$	3.5	$La_3Ni_2B_2N_3$	12

b) ***Type - II Superconductors***: Conventional Type II superconductors mainly comprise of alloys and mixtures of metal oxides which looses their superconducting property totally under the application of high magnetic field, through a more gradual process. The magnetic flux begins to penetrate at low field intensity (the lower critical field), but the last trace of superconductivity is not eliminated until a much stronger field is applied (the upper critical field) [6 - 8]. Figure 1.3 (b) gives the pictorial description of this fact. Thus, the Type II superconductors differ from Type I in their transition from a normal to a superconducting state, which is gradual across a region of '*mixed state*' behavior. A Type II will also allow some penetration by an external magnetic field into its surface, but a Type I will not.

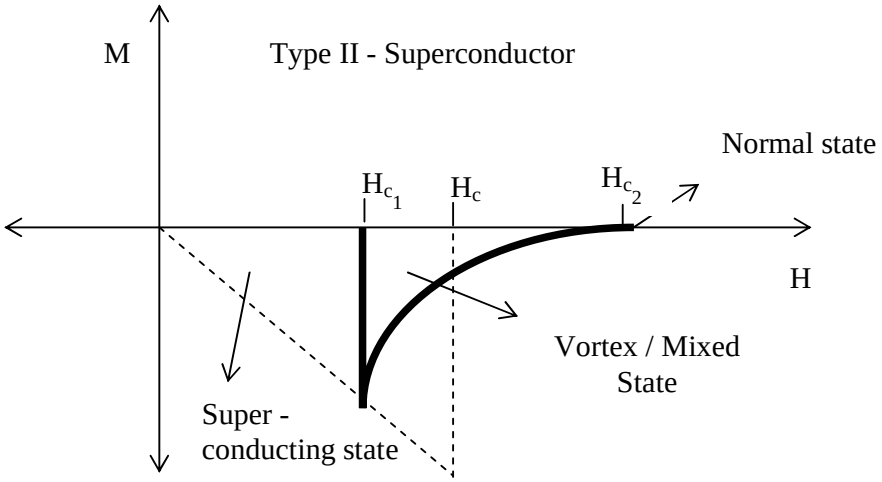

Figure 1.3 (b) Plot of Induced magnetic field (M) inside a Type II superconductor as a function of the external applied field (H) [4].

(c) ***High T_c Superconductors***: In 1986, K Alex Muller and J. Georg Bednorz discovered the first high T_c superconductor in a ceramic oxide compound of Lanthanum, Barium and Copper ($La_{1.85}Ba_{0.15}CuO_4$) at IBM Research Laboratory in Zurich [9]. The high T_c or Type II superconductors are comprised of metallic

compounds and alloys with elements like Vanadium and Niobium as exceptions. The superconducting '*perovskite*' (metal – oxide ceramics that normally have a ratio of 2 metal atoms to every 3 oxygen atoms) also belong to this category. They achieve higher T_c s than Type I superconductors by a mechanism that is still not completely understood. Some postulates into the mechanism hold that, the relation of the planar layering within the crystalline structure is responsible for conduction. It is also believed that holes of hypo-charged oxygen in the charge reservoirs are responsible (hole being the positively-charged vacancies within the lattice).

The Table 1.2 gives a list of some interesting Type II superconductors

Table 1.2 List of High T_c perovskite superconductors along with their respective T_c values

Element	T_c (^{0}K)	Element	T_c (^{0}K)
$HgBa_2Ca_2Cu_3O_8$	133	$HgBa_2CaCu_2O_6$	123
$HgBa_2CuO_4$	94-98	$Tl_2Ba_2Ca_2Cu_3O_{10}$	125-127
$TlBa_2Ca_3Cu_4O_{11}$	112	$Tl_2Ba_2CuO_6$	70
$Bi_2Sr_2Ca_2Cu_3O_{10}$	110	$Bi_2Sr_2CaCu_2O_{9/8}$	110 / 80
$Ca_{1-x}Sr_xCuO_2$	110	$TmBa_2Cu_3O_7$	101
$YBa_2Cu_3O_{7-\delta}$	93	$Y_2Ba_4Cu_7O_{15}$	93
$YBa_2Cu_4O_8$	80	$(Ba, Sr)CuO_2$	90
$La_2CaBa_2Cu_5O_{11}$	78	$(Sr, Ca)_5Cu_4O_{10}$	70
$(La, Ba)_2CuO_4$	35 – 38	$La_{1.85}Ba_{0.15}CuO_4$	35

1.3 APPLICATIONS OF SUPERCONDUCTORS

Soon after Onnes discovered superconductivity, scientists began dreaming up practical applications for this strange new phenomenon [10, 11]. Powerful new ***superconducting magnets*** could be made much smaller than a resistive magnet, because the windings could carry large currents with no energy loss. ***Generators*** wound with superconductors would generate the same amount of electricity with smaller equipment and less energy. Once the electricity was generated it could be distributed through ***superconducting wires***. Energy could be stored in superconducting coils for long periods of time without significant loss. The ability of superconductors to conduct electricity with zero resistance can be exploited in the use of ***electrical transmission lines***.

The field of electronics holds great promise for practical applications of superconductors. The generation of heat and the charging time of capacitors due to the resistance of the interconnecting metal films limit the miniaturization and increased speed of computer chips. The use of new ***superconductive films*** may result in more densely packed chips which could transmit information more rapidly by several orders of magnitude. Superconducting electronics have achieved impressive accomplishments in the field of digital electronics. Logic delays of 13 picoseconds and switching times of 9 picoseconds have been experimentally demonstrated. Through the use of basic Josephson junctions' scientists are able to make very sensitive ***microwave detectors***, ***magnetometers***, ***SQUIDS*** and very stable ***voltage sources***.

The use of superconductors for ***transportation*** has already been established using liquid helium as a refrigerant. Prototype levitated trains have been constructed in Japan by using superconducting magnets.

Superconducting magnets are already crucial components of several technologies. ***Magnetic Resonance Imaging*** (MRI) is playing an ever-increasing role in diagnostic medicine. The intense magnetic fields that are needed for these instruments are a perfect application of superconductors. Similarly, particle accelerators used in high-energy physics studies are very dependent on ***high-field superconducting magnets***.

In general the applications of superconductors can be pictorially depicted as shown in Figure 1.4.

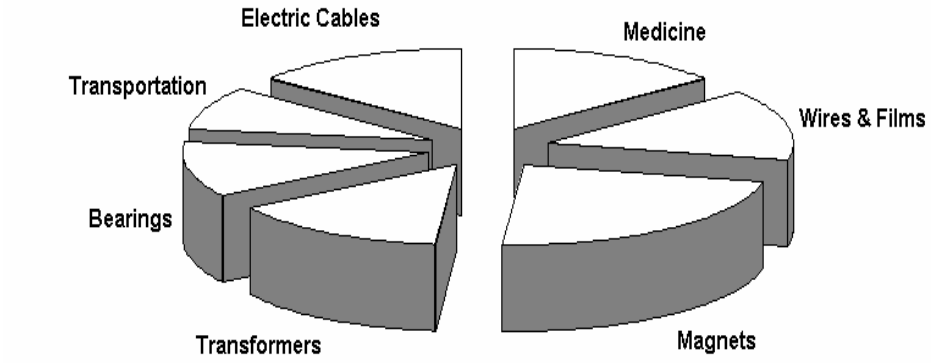

Figure 1. 4 Some applications of superconductors [12]

1.4 CURRENT STATUS OF DEVELOPMENTS IN HTSC

The development of High T_c superconductivity provides both the intellectual challenge as well as technological promise. Since its discovery, the transition temperature has been quadrupled, several crucial aspects of HTSC have been understood, various models have been proposed, numerous material processing techniques have been developed, and a wide variety of prototype devices have been or are being constructed and tested.

1.4.1 Basic Research

From the Figure 1.5, we can see the increase of T_c with time.

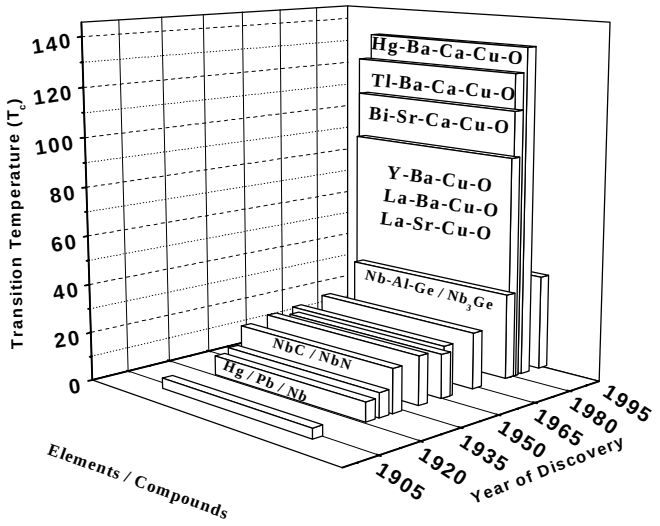

Figure 1.5 Superconductivity timeline

As can be seen from the above figure, the road to higher T_c was very slow in spite of enormous research for developing a novel HTSC material [13]. Until 1986, the highest T_c observed was in a film of inter-metallic alloy Nb_3Ge with T_c of 23 K an increase of 19 K since the first superconductor with T_c of 4.2 K over a span of 75 years. Alex Muller and Georg Bednorz synthesized a new type of superconducting material, which consisted of a ceramic oxide of Lanthanum, Barium and Copper (La-Ba-Cu-O). They observed a dramatic drop in resistivity at 35 K [9, 14] and recognized the possibility of this type of material being a high temperature superconductor. Soon after this pioneering work there has been an explosion of worldwide interest in superconductivity, particularly in oxide superconductors. In December of 1986, Tanaka et.al determined the structure of this new ceramic superconductor and found its molecular formula to be $La_{1.85}Ba_{0.15}CuO_4$ [15, 16]. In early 1987, it was observed that the critical temperature of the new ceramic superconductor could be raised by five degrees to 40 K by replacing the Barium atoms with Strontium [17, 18]. But the most significant '*Jewel in the crown'* ceramic superconductor was the $YBa_2Cu_3O_7$ (Y-123) superconductor synthesized and developed by Chu and Wu's groups in March of 1987 [19]. It was the first superconductor with T_c of ~ 90 K, well above liquid nitrogen temperature. The unusual feature of these new types of superconductors is that, almost all rare earth elements will substitute in the Yttrium position (except Pr, Ce, Tb) of the 1-2-3 structure and still yield materials with transition temperature in the 80 - 90 K range. The next round of discoveries began in early 1988 with higher T_c observed in Bi-Ca-Sr-Cu-O [20, 21] and Tl-Ca-Ba-Cu-O [22, 23] systems in early 1988. The years between 1988 and 1996 represent a period of solid advancement and many

cuprate superconductors were discovered. They may be considered to belong to or be derivable from the layered compound systems of R_2CuO_4 (R-214) with R = La, Nd, Sm, Eu and Gd, $RBa_2Cu_3O_7$ (R-123) where R = rare earths (except Ce, Pr and Tb).

Michael et al reported the occurrence of superconductivity in Bi-Sr-Cu-O at 8 K, which turned out to be n = 1 member of the $Bi_2Sr_2Ca_{n-1}Cu_nO_{2n+4}$ (Bi-22(n-1)n, with n = 1, 2, 3…) system [24]. Maeda et al while replacing R-123 elements by V-b group elements (such as Bi, Sb) detected superconductivity above 105 K in multiphase samples of BSCCO [20]. The crystal structures of three members of the homologous series Bi-12(n-1)n with n = 1, 2 and 3 with T_c 22, 80 and 110 K respectively, were determined showing a layered stacking sequence of $(BiO)_2(BaO)(CuO_2)…(Ca)(CuO_2)(BaO)$ with $n(CuO_2)$ layers separated by n-1(Ca)-layers. With increasing n > 3, the T_c decreased.

Sheng and Hermann in 1987, working on the similar lines of forming R-123 by replacing rare earth elements used the trivalent non-magnetic Tl for R. After proper synthesis methods were established, they detected superconductivity above 90 K in a multiphase sample of the composition $TlBa_2Cu_3O_x$ [22]. By partially replacing Ba by Ca in the following composition, they discovered $T_c \sim 120$ K in the multiphase sample of Tl-Ba-Ca-Cu-O in February of 1988 [23]. The structures of members of the homologous series were found to be similar to Bi-2223 but with no modulation in the $(TlO)_2$ – double layer. T_c of 90, 110 and 125K were observed for n = 1, 2 and 3 in the $Tl_2Ba_2Ca_{n-1}Cu_nO_{2n+4}$ (Tl-22(n-1)n) system. The highest T_c thus obtained for n = 3 system, was further enhanced to 131 K by the application of pressure.

Putilin et al synthesized $HgBa_2CuO_{4+\delta}$ then n = 1 member of $HgBa_2Ca_{n-1}Cu_nO_{2n+2+\delta}$ (Hg-12(n-1)n, with n = 1,2,3,..) series and found a T_c = 94 K, the highest T_c detected in a single layered cuprate [25]. It was observed that T_c increases with n at least up to 3 or 4. Schilling et al succeeded in raising the T_c to 133 K in a multiphase sample of Hg-12(n-1)n with n = 2 and 3. Later studies demonstrated that n = 1, 2 or 3 members of Hg-12(n-1)n possess T_c = 97, 127 and 134 K, when optimally doped [26]. The crystal structure of Hg-12(n-1)n displays the stacking sequence of $(HgO_\delta)(BaO)(CuO_2)(Ca)(CuO_2)….(Ca)(CuO_2)(BaO)$, with $n(CuO_2)$-layers separated by n-1(Ca)-layers. This layered structure is similar to $TlBa_2Ca_{n-1}Cu_nO_{2n+\delta}$, except Hg-12(n-1)n exhibits a large vacancy concentration in the (HgO_δ)-layer for oxygen to occupy. Due to these local structures of the HgO_δ-layers, unusually large T_c enhancement by pressure was achieved, pushing T_c first to ~ 154 K at ~ 16 GPa, and then to 164 K at ~ 30 GPa, setting new T_c records.

The highest T_c of 124 K was observed in a non-toxic element cuprate with the nominal composition $CuBa_2Ca_{n-1}Cu_nO_{2n+2+\delta}$ (Cu-12(n-1)n, with n = 1,2,3,..) [27]. The compound $CuBa_2Ca_{n-1}Cu_nO_{2n+2+\delta}$ with n = 3 and 4 were formed under high pressure with T_c of 60 and 117 K respectively. $Cu_2Ba_2Ca_2Cu_3O_{9+\delta}$ was also synthesized under high pressure to show a T_c ~ 110 K.

So far it has been observed that T_c increases with n, the number of CuO_2 layers per unit formula. Smith et al, in 1991, synthesized electron doped $Sr_{1-y}Nd_yCuO_2$ under 2.4 GPa which showed T_c ~ 40 K [28]. Later, Takano et al detected superconductivity up to 110 K in $(Sr_{1-x}Ca_x)_{0.9}CuO_2$ prepared under 6 GPa [29]. Superconductivity up to 90 K has been reported in layered Sr_2CuO_4 synthesized

under high pressures [30, 31]. The samples thus prepared exhibit a structure similar to that of R-214 (1T). According to the Cu-valence effect on T_c, Sr_2CuO_4 was not expected to be superconducting, but the superconductivity at 90 K is due to the impurity such as $S_3Cu_2O_{5+\delta}$ present in the samples.

One of the most prominent discoveries of superconductivity in recent times has been the superconductivity in the non-oxide binary compound MgB_2 [32, 33]. Magnesium diboride (MgB_2) was known since the early 1950s but was tested for its superconducting property very recently by Akimitsu and Nagamatsu et al observed a remarkably high T_c = 40 K, for binary compound. The simple crystal structure (hexagonal), high T_c, large coherence lengths, high critical current densities and fields, and transparency of grain boundaries to current make MgB_2 a very suitable candidate for both large-scale applications and electronic devices. In the framework of the BCS theory the low-mass elements result in higher frequency phonon modes, which may lead to enhanced transition temperature. The discovery of superconductivity in MgB_2 confirms the predictions of higher T_c in compounds containing light elements, because it is believed that the metallic B layers play a crucial role in the superconductivity of MgB_2 [34]. With T_c (~ 40 K) close to or above the theoretical value predicted by BCS theory, MgB_2 presents a strong argument to be considered as a non-conventional superconductor.

1.4.2 Applications: Challenges for HTSC materials

High-temperature superconductors are brittle ceramic materials in which elements such as Yttrium and Barium, or Lanthanum and Strontium, are sandwiched between layers of Copper and Oxygen atoms. This layered atomic structure causes the materials to have highly anisotropic physical and superconducting properties. There

are two key physical properties related to granular high-temperature superconductors. First, the 'coherence length' – the length over which the superconducting wavefunction extends beyond a grain boundary. And second, the 'upper critical field' - the maximum magnetic field below which the material remains superconducting. The two properties are inversely related: the longer the coherence length, the lower the upper critical field. High temperature superconductors have a very high upper critical field (~ 18 T), which could open up a range of applications in extreme magnetic fields. In turn, the coherence length is very short, less than 2 nm. This means that the polycrystalline grains tend to be weak-linked unless the grain boundaries are both smooth at the single-atom level and free from disorder over a length scale significantly less than 2 nm. The high temperature superconductors are quasi-two-dimensional structures comprising weakly coupled copper-oxide (CuO_2) layers. They are therefore highly anisotropic. These two factors – the coherence length and the anisotropy – mean that a polycrystalline HTSC wire must be dense, have a high degree of grain alignment and have high-quality grain boundaries. Although there are more than 50 known HTSC materials, only two have been used successfully to form long-length HTSC wires: the $Bi_2Sr_2Ca_2Cu_3O_{10}$ (Bi-2223) and $Bi_2Sr_2CaCu_2O_8$ (Bi-2212).

With the discovery of higher temperature superconductors, many applications of these materials have been prototyped in recent years [35 - 37]. These applications can be divided into two categories: bulk (as wires, tapes, cables etc) and film based (for electronic device applications).

a) Superconductors in bulk form

i). ***Supermagnets***: The latest medical diagnostic tool, the MRI (Magnetic Resonance Imagining) is commonly found in hospitals, where it is used to obtain detailed images of the interiors of a human body. The MRI uses a superconducting magnet to align hydrogen nuclei in the body. Radio pulses jostle the nuclei, as they wobble; the nuclei emit weak radio signals of their own that can be detected. With the advent of superconductors, this can be done without exposing the patient to X-rays or having to inject them with some kind of dye. Because MRI uses low temperature superconductors, this process is very expensive. But, when higher temperature superconductors take their place in the MRI, this process will become more affordable and may some day do away with X-rays. As of now, the MRI is considered the most successful use of superconductors.

The second most important potential use of superconductors is in the development of powerful magnets for generating high fields. Niobium-Titanium and Niobium-3-Tin achieve current densities of about 400,000 amperes per square centimeter 1000 times as much current as the copper wire. Bulk samples (not wires!) of Y-Ba-Cu-O have been made at the AT&T Bell laboratories that carry 4,000 amperes per square centimeter at 77 K in a one-tesla field and without field it carries 17,000 amperes per square centimeter.

ii). ***Generators and Power lines*****:** In electric generators mechanical power provided by a spinning turbine rotates a magnet, which induces an electric current. Superconducting magnets could increase the efficiency of such generators. Large superconducting generators are projected to be about 99.5 % efficient. HTSC cables offer a two-to tenfold increase in power capacity for the same cross-sectional area of

cable. And impressively, the total HTSC conductor weighs 70 times less than the copper cables it replaces.

iii). ***Transformers*:** Another promising area for applications of superconductors is in transformers. A large HTSC system (> 30 MV A) is expected to weigh about half as much as a conventional transformer. Also the HTSC offer the opportunity to eliminate the oil that is used for cooling and dielectric purposes.

iv). *Storing Electrical Energy*: An energy-storage system would enable a utility to store excess energy during times of overproduction and then tap it when demand exceeds. A system made of superconductors would be able to hold a massive amount of direct current with almost no energy loss.

On a smaller and less expensive scale, SMES could be put to a different use to smooth the transmission of power generated by highly erratic sources, such as an array of windmills. SMES units of this type are capable of switching large amounts of power but do not have to store much energy, and so they do not require expensive containment systems.

v). *Levitating Trains*: One of the most widely discussed and debated applications of superconductor is the Maglev (Magnetically Levitating) train, which could cruise at high speed, suspended above a guide way of magnetic forces. As the train advances over aluminium coils in the guide way, the magnets induce opposing fields that levitate the train. High temperature superconductors would offer greater engineering reliability for Maglev trains.

b) Superconductors in the form of films

i). *Superconducting computers*: Ever since Brian D. Josephson realized the superconducting effects in an electronic device (now known as Josephson effect) the

dream of building a superconducting computer took shape. In simple words, the Josephson effect is the 'jumping of electrons from one superconductor to another across an insulating barrier'. It is also known as tunneling [38].

A ***Josephson junction*** consists of a thin layer of insulating material sandwiched between layers of a superconducting material.

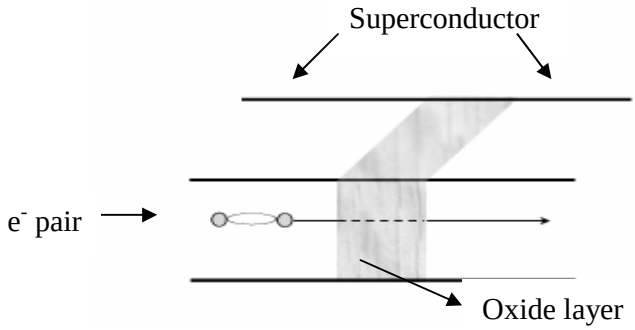

Figure 1.6 Josephson Junctions

It switches voltages very fast while consuming several orders of magnitude less energy than conventional devices. Their low power consumption promised more compact computers.

ii). *SQUID*: The Superconducting Quantum Interference Device (SQUID) is an important application of Josephson junction. It consists of one or two Josephson junctions inserted into a loop of superconducting wire. The device is extraordinary sensitive to changes in electromagnetic fields. The magnetic flux contained within a superconducting loop is quantized: it occurs only in integer multiples of a basic unit called fluxon (about 2 X 10^{-7} Gauss cm^2). The current in the SQUID is a periodic function of the total fluxons contained by the loop and is extremely sensitive to any change in the magnetic flux.

A SQUID can measure voltage differences as small as 10^{-18} volt, currents as small as 10^{-18} ampere (only several electrons per second!) and magnetic fields of less than 10^{-14} tesla (one ten-billionth of the earth's magnetic field). When a SQUID is operated at four degrees K, thermal noise is virtually eliminated and the SQUID's sensitivity approaches the fundamental limits imposed by quantum mechanics.

The SQUID is and in some cases will be used in future for the following applications:

- ✓ For building detectors (SONAR) for submarines
- ✓ To detect faint magnetic signals associated with electrically activity in the heart and brain.
- ✓ *Magnetoencephalography* detects signals from the brain that are only slightly greater than 10^{-13} tesla and can determine the source of the nerve signal to within a few millimeters.

Some other applications of high temperature superconductors is in fault-current limiters and low-thermal-conductivity current leads, which are used to reduce heat leaks into the cryo-environment of low-temperature superconducting high-field magnets. The thin films also find applications for microwave antennas and filters.

1.5 BRIEF THEORETICAL BACKGROUND

(i). *The BCS Theory*

The complete explanation to the mechanism of superconductivity was given by the macroscopic theory of John Bardeen, Leon N. Cooper, and J. Robert Schrieffer (known as the BCS theory) in 1957 [39]. The BCS theory accounts for (a) Second

order phase transition, (b) an electronic specific heat varying as $\exp(-T_0/T)$ near $T = 0\ ^0K$ and other evidence for an energy gap for individual particle-like excitations, (c) Meissner effect ($B = 0$), (d) effects associated with infinite conductivity ($E = 0$) and (e) dependence of T_c on isotopic mass $T_c\sqrt{M} = \text{constant}$ [40].

The normal conductors have an orderly arrangement of lattice surrounded by a "sea of electrons". This sea is a body of electrons that are shared by many nuclei; it is caused by the atoms losing their valence electrons to obtain the preferred electronic configuration of noble gases. According to the Pauli exclusion principle, no two electrons in an atom can have the same four quantum numbers. Similarly, in a sea of electrons, no two electrons can have the same energy. Therefore, the electrons in a metal range from having the lowest amount of kinetic energy possible to the highest energy possible, known as the Fermi energy. The energies of the electrons are in discrete energy levels, and the groupings of levels are called energy bands. In a metallic conductor, the valence band is not full, so if an electrical potential is applied across the materials, electrons can easily flow and produce a current. The conduction band in metallic conductors is mostly empty.

Inside a superconductor the behavior of electrons is vastly different. The impurities and lattice are still there, but the movement of the superconducting electrons through the obstacle course is quite different. As the superconducting electrons travel through the conductor they pass unobstructed through the complex lattice, because they bump into nothing and create no friction. They can thus transmit electricity with no appreciable loss in the current and no loss of energy. The

explanation of the BCS theory is based on the "***electron-phonon-electron***" interaction, now also known as "***Cooper pair formation***".

Band theory can explain the behavior of normal metals, but it is not applicable to superconductors as the electron pairs or Cooper pairs cannot be treated like individual objects. In normal conductors, there is a small electron-phonon interaction, that is, the vibrations of the lattice (phonons) have a small effect on the electrons. However, a large electron-phonon interaction is also the cause of superconductivity. This is why most good conductors such as Gold and Silver don't superconduct, and most of the best superconductors tend to be poor ordinary conductors.

Formation of Cooper pairs

As an electron moves through a superconductor, it distorts the lattice because the electron's negative charge attracts the surrounding positive nuclei, as shown in the Figure 1.7 (a).

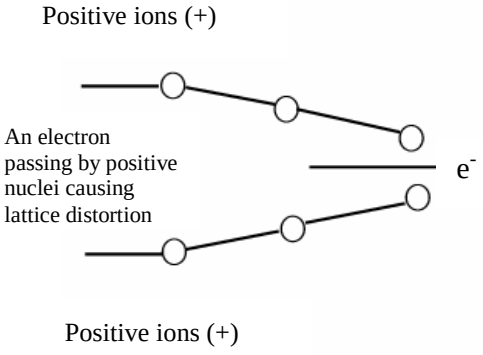

Figure 1.7 (a) Wave of lattice distortion due to attraction to a moving electron

If a second electron comes close enough to the first electron, it gets drawn to the area of the lattice that is distorted because the positive charges are more concentrated there. In other words, there is an effective attraction between the two

electrons that overcomes their repulsive forces. This weakly bound pair, called a Cooper pair, results in a lower state of energy. In this pair, there is a transfer of momentum between the two electrons. The electrons that form these pairs are called "***superconducting electrons***" as shown in Figure 1.7(b).

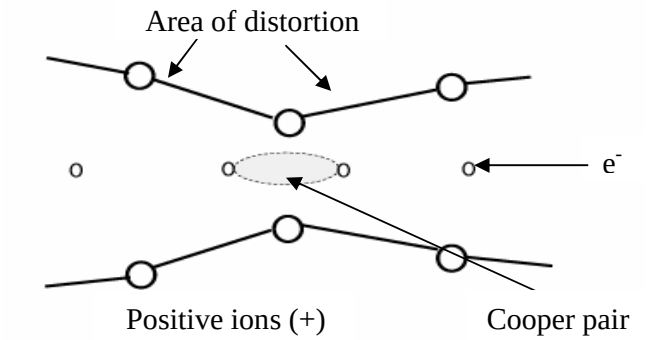

Figure 1.7 (b) Two electrons, called Cooper pairs, become locked together and travel though the lattice

These electrons are responsible for superconductivity, and the other normal electrons in the material do not have much of a role. In a superconductor, the Cooper pairs are constantly breaking and re-pairing with new partners because a large distance separates the electrons in a pair and they overlap. There is an optimal number of pairs that can form and the superconductor obtains the lowest energy possible when the maximum number of pairs are made. At the transition temperatures, the superconducting state becomes the more favorable, lower energy state, and electrons begin to form pairs. When a superconductor is warmed, the heat is first used to break the Cooper pairs before raising the temperature of the material. This explains the change in specific heat when a material moves from the normal state into the superconducting state. Superconductivity is different from other states of matter

because in phases such as liquid phase or solid phase, the molecules settle and condense in physical space. However, when a material becomes a superconductor, the electrons condense in momentum space. Unlike liquid and gas phases, superconductivity is a second-order phase transition, that is, when a material is cooled so that it becomes a superconductor, the transition takes place almost instantaneously without any latent heat.

According to the BCS theory T_c is given as

$$\mathbf{T_c = 1.14\Theta_D \exp [-1/N(E_F)V]}$$

Where, Θ_D = Debye temperature,

N (E_F) = electron-density of state at Fermi surface,

V = electron-phonon interaction.

(ii) ***Ginzburg – Landau Theory***

The background of the Ginzburg – Landau (G-L) theory [41] is the London Theory given by F. London and H. London [42]. The London theory is purely classical. According to the London theory, the extension of Maxwell's equation to the superconductivity applies, and can be given as:

$$\mathbf{B (x) = \lambda^2 \nabla^2 B}$$

This is the London equation, where B decays exponentially with x (x = depth). The value $\lambda = \sqrt{\alpha}$ (where α = constant = $m_s/\mu_0 n_s e^2$); is called the London penetration depth. λ is temperature dependent, tending to infinity as T approaches T_c. In non-cubic superconductors, and especially high temperature superconductors, penetration depths are anisotropic. They depend on crystallographic orientations with respect to both magnetic field and specimen surface.

The superconducting carriers have a free energy. In a magnetic field there are two opposing components in the surface energy. One component is due to the magnetic energy and the other due to the free energy of the superconducting state. The superconducting state is defined by three very important factors: critical temperature (T_c), critical field (H_c), and critical current density (J_c). Each of these parameters is very dependent on the other two properties present. The phase diagram of Figure 1.8, demonstrates the relationship between T_c, H_c and J_c.

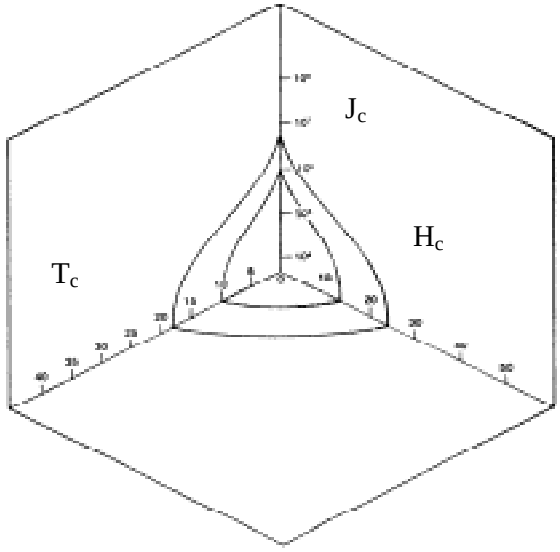

Figure 1.8 Relationship between T_c, H_c and J_c – Phase diagram

The two theories are consistent with some exceptions. They are useful because the more complete BCS theory is a microscopic theory, so that additional application of many body theory is needed to reach the same results. The basic concept of G-L theory is the order parameter 'ψ', which represents the ordering of superelectrons, formed during the superconducting phase transformation. The theory is used to predict B_{c1}, B_{c2}, the penetration depth, coherence length, the criteria for

Type I and Type II superconductors etc. Most macroscopic properties are predicted by this theory.

1.6 AIM OF THE PRESENT WORK

Many superconducting structures have been synthesized by various groups all over the world, both in oxides and from inter-metallic compounds with varying T_c, H_c and J_c values. But till date, there has been no satisfactory explanation for the occurrence of superconductivity in ceramic oxides, which have a rather complex structure. The widely studied structure of all the high T_c compounds is the 1-2-3 type of superconductors. There are many approaches by which this 1-2-3 structure can be formed. In the present work, an attempt has been made to study this fascinating structure from a different point of view. The approach is from a La-224 ($La_2Ba_2Cu_4O_z$) non-superconductor, which has been made superconducting by the simultaneous addition of CaO and CuO, thus yielding the La-2125 ($La_2Ca_1Ba_2Cu_5O_z$) superconductor [43, 44]. Both the starting La-224 and final La-2125 phases are derivatives of the La-123 superconductors [45].

The exact mechanism of any superconducting system can be best studied by the role played by dopants in the structure. Keeping this in mind the following three series of samples were studied

(i) $La_{2-x}Dy_xCa_yBa_2Cu_{4+y}O_z$ (LaDyCaBCO)

(ii) $La_{2-x}Pr_xCa_yBa_2Cu_{4+y}O_z$ (LaPrCaBCO)

(iii) $La_{1.5}Nd_{0.5}Ca_1Ba_2[Cu_{1-y}Mo_y]_5O_z$ and

$La_{1.5-z}Nd_{0.5}Ca_{1+z}Ba_2[Cu_{1-y}Mo_y]_5O_z$ (LCBMO)

The main emphasis in this work has been on establishing the structure – property relation in the La-2125 type of mixed oxide superconductors. For this purpose, the Neutron Diffraction (ND) studies on powder samples were carried out for the structural investigations of LaDyCaBCO system. The analysis of the ND data was carried out for the determining structural information like space group, phase purity, atomic positions, occupancy of constituent elements, unit cell parameters etc., by Rietveld Refinement method using the Fullprof program. Rietveld refinement method was also used to refine the X-ray Diffraction (XRD) data of LaPrCaBCO system along with LaDyCaBCO system. Rietveld refinement has emerged as a very powerful tool in refining the structure of any material. It gives very precise information about the crystal structure.

La-2125 types of superconductors possess stable tetragonal structure – isostructural to tetragonal Y-123 superconductors. The Rietveld analysis of ND and XRD data are in agreement on the fact that, the structure is stable tetragonal throughout the doping range, and the unit cell parameters are also in good agreement. Since, ND measurements are expensive and rarely available; rest of the series (i.e., LaPrCaBCO and LaNdCaBCO) were characterized by XRD for structural studies. Also, the oxygen content, a very important ingredient in oxide superconductors for superconductivity, has been determined by ND and crosschecked by Iodometric titration method. The values are in good agreement. Thus, for other samples, it was assumed that the oxygen content thus obtained is near the true values.

Another aspect of studying the superconducting property of the oxide materials is the study in thin film form. The tetragonal superconducting thin films are reported to be more stable against degradation by atmosphere and water. Thus, they

promise to be eligible candidates for practical applications of tetragonal superconductors. The thin films of LaDyCaBCO system (La-2125) were synthesized for the first time during the course of this work. Though, La-2125 is a derivate of La-123 structure; it was found that the deposition parameters for both are different. After many attempts the superconducting tetragonal thin films were successfully synthesized using Pulsed Laser Deposition (PLD) technique. PLD is one of the simplest yet very efficient thin films growing technique. The stochiometric composition of the films is fairly maintained during ablation by PLD.

In summary, the present work deals with two aspects of the doped La-2125 superconductors. One is the crystal structure determination by ND studies and another, synthesis of thin films using PLD technique. The results of both these techniques are presented in this thesis.

The role of different dopants in La-2125 like fluctuating valence Pr at La and Mo at Cu sites were also studied during the course of this work. The results of these studies are also presented.

REFERENCES

[1] H. Kammerling Onnes, Leiden Commun. **1226** 124 (1911)

[2] Frank J. Owens and Charles P. Poole Jr.
"The New Superconductors", Plenum Press

[3] W. Meissner and R. Ochsenfeld; Naturewiss **21**, 787 (1933)

[4] T. H. Geballe and J. K. Hulm
Scientific American 112 (August – 1990)

[5] Paul A. Tipler
"Physics for Scientists and Engineers" Worth Publishers,
N. Y (1991)

[6] Allon Percus
"The History of Superconductors", Los Almos National Labs URL

[7] Robert W Dull and H. Richard Kerchner
"A Teacher's Guide to Superconductivity"
Oak Ride National Laboratory URL (ORNL/M-3063/R1)

[8] Ari Briskman, Dan For, Steven Meier, Marcus Perlman
"Superconductivity", Rice University URL

[9] J. G. Bednorz and K. A. Muller; Z. Physik, B **64**, 189 (1986)

[10] Charles W. Billings
"Superconductivity: From discovery to breakthrough"
Cobblehill Books, N.Y (1991)

[11] Bruce Schechter
"The Path of No resistance", Simon & Schuster Pub., N.Y (1989)

[12] "What is Superconductivity?"

BICC General Superconductors URL

[13] A. Bourdillon and N.X. Tan Bourdillon

"High Temperature Superconductors – Processing & Science"

Academic Press Inc. (1993)

[14] J. G. Bednorz, M. Takashige and K. A. Muller;

Europhys. Lett **3**, 379, (1987)

[15] H. Takagi, S. Uchida, K. Kitazawa and S. Tanaka

Jpn. J. App. Phys. **26**, Part 2, L123 (1987)

[16] S. Uchida, H. Takagi, K. Kitazawa and S. Tanaka

Jpn. J. App. Phys. **26**, Part2, L151 (1987)

[17] S. Uchida, H. Takagi, K. Kitazawa and S. Tanaka

Jpn. J. App. Phys. **26**, L1-L2 (1987)

[18] P. Ganguly and C. N. R. Rao

Proc. Indian. Acad. Sci. Chem. Sci **97**, 631 (1987)

[19] M. K. Wu, J. R. Ashburn, C. J. Torng, P. H. Hor, R. L. Meng, L. Gao, Z. J. Huang, Y. Q. Wang and C. W. Chu

Phys. Rev. Lett. **58**, 908 (1987)

[20] H. Maeda, Y. Tanaka, M. Fukutomi and A. Asana

Jpn. J. App. Phys. **27**, L209 (1988)

[21] C. W. Chu, J. Bechtold, L. Gao, P. H. Hor, Z. J. Huang, R. L. Meng, Y. Y. Sun, Y. Q. Wang and Y. Y. Xue

Phys. Rev. Lett. **60**, 941 (1988)

[22] Z. Z. Sheng and A. M. Hermann; Nature **332**, 55 (1988)

[23] Z. Z. Sheng and A. M. Hermann; Nature **332**, 138 (1988)

[24] C. Michel et.al; Z. Phys B **68**, 21 (1987)

[25] S. N. Putilin et.al; Nature **362**, 226 (1992)

[26] A. Schilling et.al; Nature **363**, 56 (1993)

[27] L. Gao et.al; Mod. Phys. Lett. B **9**, 1397 (1995)

[28] M. O. Smith et.al; Nature **351**, 519 (1991)

[29] M. Takano et.al; Physica C **176**, 441 (1991)

[30] Z. Hiroi et.al; Nature **364**, 315 (1993)

[31] P. D. Han et.al; Physica C **228**, 129 (1994)

[32] J. Akimitsu
"Symposium on Transition Metal Oxides"- Sendai
Japan (10-01-2001)

[33] J. Nagamatsu, N. Nakagawa, T. Muranaka, Y. Zenitami and J. Akimitsu; Nature **410**, 63 (2001)

[34] J. Kortus, I. I. Mazin, K. D. Belashchenko, V. P. Antropov and L. L. Boyer; Phys. Rev. Lett. **86**, 4656 (2001)

[35] Alan M. Wolskey, Robert F. Giese and E. J. Daniels
Scientific American, **45** (February – 1989)

[36] Randy Simon; Physics Today **64** (June – 1991)

[37] John Clarke; Scientific American **36** (August – 1994)

[38] B. D. Josephson; Phys. Rev. Lett **1**, 25 (1962)

[39] J. Bardeen, L. N. Cooper and J. R. Schrieffer
Phys. Rev. **106**, 162 (1957)

[40] J. Bardeen, L. N. Cooper and J. R. Schrieffer
Phys. Rev. **108**, 1175 (1957)

[41] V. L. Ginzburg and L. D. Landau; J.E.T.P **20**, 1064 (1950)

[42] F. London and H. London; Z. Physik **96**, 359 (1935)

[43] D. G. Kuberkar, N. A. Shah, M. V. Subbarao, A. G. Joshi and
R. G. Kulkarni; Materials Letters **37**, 68 (1998)

[44] D. G. Kuberkar, N. A. Shah, M. R. Gonal, Ram Prasad and
R. G. Kulkarni; J. of. Supercond. **13**, 37 (2000)

[45] D. G. Kuberkar, R. S. Thampi, Nikesh A. Shah, Krushna Mavani,
S. Rayaprol, S. K. Malik, W. B. Yelon and R. G. Kulkarni
J. Appl. Phys. **89**, 7657 (2001)

CHAPTER – II

Synthesis and Experimental Characterizations of HTSC materials

2.1 SYNTHESIS METHODS – BULK AND THIN FILMS

2.1.1 Synthesis of Bulk samples

– The 'shake & bake' method: The shake and bake method of preparing the samples involves two steps. First is the 'shake' method i.e., to prepare the starting compounds for actual sample preparation. It involves, pre-heating (i.e., to remove the unwanted moisture from the compounds) and weighing accurately in stochiometric quantities. The second step is the 'bake' method, which involves sintering of the samples with intermittent grinding to obtain homogeneous mixture. The homogenous mixture can be obtained either by fine grinding, ball milling, co-precipitation, sol-gel etc., methods.

(a) *Solid State Reaction route (Chemical Reaction method)*: The starting compounds used for the preparation of high T_c superconductors are pure, anhydrous powders of oxides, carbonates or nitrates of the metallic elements. Prior to reacting, these compounds are broken down by mixing with other compounds so that neighbouring grains react in furnace to form new stable phases. For example, the carbonates (say $BaCO_3$) decompose, releasing carbon dioxide, at temperatures, which are comparable to typical sintering temperatures. It decomposes and reacts with CuO to form ternaries such as $BaCuO_2$ or other compounds. This initial decomposition of stable starting powders, by heating below their melting points in known as ***calcination***.

Decomposition is typically endothermic. The rate at which calcination occurs depends on

(1) The rate of reaction at the reacting surface,

(2) The rate of heat transfer and,

(3) The rate of gas transport.

The enthalpy (ΔH^{0}_{298}) of decomposition reaction of $BaCO_3$:

$$\mathbf{BaCO_3(s) \rightarrow BaO(s) + CO_2\ (g)}$$

is –1.218 J mol^{-1}. The reaction rate depends on a balance of heat flow to the reaction interface and gas flow away from it. The heat flow depends also on the thermal conductivity of the porous BaO and on the heat transfer rate from the furnace. The solid BaO, which is one product of the decomposition, then reacts with neighbouring grains by chemical processes, which are common to sintering [1]. The reactions can be idealized as follows:

$$\mathbf{BaCO_3(s) + CuO(s) \rightarrow CO_2\ (g) + BaCuO_2(s)}$$

$$\mathbf{4BaCuO_2 + Y_2O_3 + 2CuO \rightarrow}\ \boldsymbol{2\ YBa_2Cu_3O_{7-\delta}}$$

In sintering, all grains in adjacent particles react and bond. In homogeneous reactions, i.e., when all of the reactants are in the same phase, the reaction rate, *dc/dt,* is described by classical chemical-reaction kinetics. The rate is proportional to the concentrations of the reactants, c_1, c_2, c_3, *etc.*, raised by powers corresponding to respective order of reaction$\alpha,\beta\ \gamma$ etc.

$$\mathbf{dc/dt = Kc_1^{\alpha}c_2^{\beta}c_3^{\gamma}\ldots}$$

The reaction constant, K, is related to the activation energy, Q, through the Arrhenius equation:

$$\mathbf{K = A\ exp\ (-Q/RT)}$$

where A is a constant.

In ceramic systems, the reactions generally occur at interfaces between different phases and are therefore heterogeneous. The reaction rate depends on

(1) Transport of reactants to the phase boundary,

(2) Reaction at the phase boundary and,

(3) Transport of the products away from the phase boundary.

The rate-limiting factor can be either the slowest of the transport mechanisms or slowest of the chemical reactions.

Repeated grinding, mixing and re-sintering are needed to make a reaction to complete so as to form single-phase high T_c compounds. Surface contact between particles can be maximized by pressing the powders into pellets before sintering and the initial shape of the compacted material can often be retained, with more or less shrinkage or expansion, depending on the processing conditions.

The dominant physical factor controlling sintering is temperature. In traditional ceramics a typical sintering temperature is three-quarters of the melting temperature expressed on the absolute scale. However, the high temperature superconductors require accurate control.

Two features, which occur during sintering, are necking between grains and the consequent change in pore shape. The necking results due to the reduction in surface energy. Broad interfaces between grains determine both mechanical and electrical properties. However, in the processing of high T_c materials, it is even more important to ensure that chemical reaction goes to completion and that the material product contains only the desired homogeneous single phase. Chemical inhomogeneity results in intergranular phases, which constitute weak links.

Homogeneity is enhanced by fine grain size and also by good mixing, especially of starting powders.

The fine powders, or homogeneous mixtures of the starting compounds can be achieved by any of the following methods:

(i) ***Milling media (Ball milling)***: Ball mill is commonly used for mixing and grinding larger quantities of ceramic powders. Careful selection of the milling media is required to avoid the contamination of the samples by the media. Balls or cylinders of selected materials are mixed with the ceramic compounds in a volatile organic lubricant (e.g. Acetone, Propanol etc), and the mixture is poured into suitable jars. These jars are sealed and made to rotate for long periods, e.g., several days, on motorized rollers. The balls generally used for the preparation of high T_c superconductors are made up of *partially stabilized Zirconia* (PSZ) [2]. Finer powders require smaller balls for effective milling. A typical volume ratio of powder to balls is 3:1. The typical particle sizes after milling range above 10 μm. Powder can be further grounded to finer particle sizes, about 1 μm, by *attrition milling.* The powder is suspended in slurry and pumped through a mill containing fine ball milling media, which are rapidly shaken in a cylindrical container by a central rotating screw shaft. Attrition milling has the advantage in speed, since the process takes hours instead of days.

(ii) ***Co-precipitation method***: The reaction rate can be speeded up by reducing the particle size and by mixing of pre-reacted compounds. In the co-precipitation method, soluble compounds, typically nitrates, are firstly dissolved in a suitable solvent, typically aqueous. Sometimes warming is required, e.g., Ba salts. Solutions, which

contaminate the final product, such as chlorides or sulfates, are usually avoided. The various ionic species then form chemical bonds, for example with added oxalate anions, and precipitate from the liquid phase. With the control of pH and temperature, it is possible to promote simultaneous co-precipitation of the various species [3]. Anions commonly used for co-precipitation of high T_c superconducting compounds are carbonates, oxalates, hydroxides, citrates, etc. Many variations in procedure have been used, some with the use of precursors to overcome differences in solubility between ions. The co-precipitated powders are then calcined.

(iii) ***Aerosol Techniques***: Fine, well mixed particles can be formed from the same nitrate solutions by atomization in a jet of gas such as O_2. The aerosol formed can be either frozen and dried in a freezer drier, or alternatively dried and reacted by passing in a flow of O_2 gas through a furnace, which is called *spray drying* or as *spray calcination* if the furnace temperature is sufficiently high to promote chemical reaction. An aerosol is formed by an atomizer. If an aerosol flow rate of 3 standard liters per minute (slm) is passed with a residence time of 25 seconds, through a furnace raised to 950 ^{0}C, powders formed from the nitrates of Y, Ba and Cu decompose and react [4]. Dried, calcined powder is collected on a warmed filter at the end of the furnace. Typical particle sizes are in the 2 – 10 μm range.

Freezing can be performed by passage of the aerosol through liquid nitrogen or through a cold liquid, such as *n-hexane* at –100 ^{0}C. If the frozen aerosol is transferred to a vacuum chamber at pressure less than 27 kPa (0.2 Torr), the droplets in the aerosol are dried by sublimation, and sub-micron sized particles can be prepared. Typically the frozen powders are hydrated, and heating drives off the water

molecules. If melting occurs before calcination reactions, the phase separation takes place, and the chief benefit of the frozen aerosol mixture is lost. Phase separation is reduced by rapid heating, but for best results either the anhydrous nitrate should be prepared by heating in vacuum, or other solutions must be used, e.g., acetates. If the nitrates are used, the sub-micron sized, dried powders of high T_c starting compounds are heated to 50 ^{0}C in vacuum and transferred quickly to preheated crucibles for calcination at 700^0 – 940 ^{0}C. The effectiveness of freeze-drying for the formation of fine mixed particles is reduced if precipitation before the aerosol is frozen. For this reason, concentration and pH are important parameters. Mass quantities can be mixed with drying times of 24 hours or more.

(iv) ***Sol-gel***: "Sol" describes the dispersion of colloids, i.e., particles in the range of 1 – 100 nm diameter, in liquids. If the viscosity of the sol is made to increase sufficiently, e.g., by partial loss of the liquid phase, it becomes a rigid "gel". Sol-gel technique can be used for several purposes including the formation of fine powders, homogeneous thin and thick films, fibers, homogeneous bulk material, porous solids and powders [5]. "Sol-gel" methods have been used to prepare both Y-123 and Bi-2212 superconductors. There has been considerable development in sol-gel techniques resulting from applications dependent on organic solvents, as even nano-scale particles can be prepared. An example of the use of organic solvents is the use of metal alkoxide precursor method. The chief difficulties in using this technique lie in the relative insolubility of Cu alkoxides in organic solvents and different hydrolysis rates for the different metal alkoxides. For these reasons, stochiometric and homogeneous oxides are not easily prepared. In the alternative aqueous route, water-soluble starting powders, typically nitrates or acetates are first dissolved as in the co-

precipitation technique. These solutions are generally simply prepared. Gels are subsequently formed in a variety of ways, such as by ethylene glycol solutions with nitrates, or by the addition of ammonium hydroxide or pH control of acetate solution. Among with the benefits, especially homogeneity, which are found in the sol-gel technique products, there lie many disadvantages. These include

(a) Residual carbon left from the organic solvents after firing,

(b) Long processing times and,

(c) Health hazards of organic solvents.

(v). ***Precursor routes***: The sol-gel technique is one example of the use of organic solvents as precursors in the formation of high T_c compounds. In processing with inorganic compounds, advantages are frequently obtained by sequencing the reactions and forming intermediate precursors. Single phase Y-123 is formed comparatively easily, precursors are not often used in forming this compound but they have important uses in forming the $A_aB_2Ca_nCu_{n+1}O_{6+2n}$ compounds e.g., Tl-2223. Precursor routes have been applied with several aims: to reduce multiphase components, e.g., Bi-2201 and Bi-2212 in Bi-2223, to reduce processing times or to increase density. Standard metallurgical processes in inert atmospheres can form metallic precursors. As the metallic elements generally have low miscibilities, rapid solidification is required to reduce segregation.

– *Pelletizing & Shaping:* Once the samples have been prepared in the powder form, it is imperative to give them a definite shape for practical purposes. Unlike, metals, ceramics are generally shaped prior to firing rather than after firing. This is not only because they are more brittle and difficult to handle, but also because pressure is normally required before sintering so as to ensure large areas of surface contact

between grains. Large areas of surface contact not only increase reaction rates, but also tend to increase the density and strength of the final product. The grain morphologies of the final products depend on processing conditions and determine their mechanical and electrical properties. Some high T_c materials, like Y-123, tend to densify during sintering, and the densification can be increased with sintering aids. On the other hand, Bi-2223 has strong preferred growth directions, which cause the material to expand during sintering and yield a product, which is, except with specialized processing, porous. The high T_c samples are usually palletized, formed into wires and tapes.

(i) ***Pelletization***: Pellets are most easily formed by axial pressure applied with a hydraulic press to powder in a die. The effects of pressure are

(a) To reduce pore size,

(b) To break up particles especially at surfaces in contact, &

(c) To introduce strain and plastic flow.

After pressing, the pellets are handled carefully to avoid mechanical stress. The pellets are placed on chips or powder of the same (superconductor) material to avoid contamination from underlying brick during firing. Cracks, introduced by inhomogeneous compression, tend to grow during sintering for reasons of stress relief.

(ii) ***Wire formation***: Wires can be formed by extrusion or by drawing. Drawing can only be used with materials having sufficient density, but not with brittle materials such as the high T_c ceramics. Two methods are commonly used for preparing superconducting wires, one being the powder-in-tube method and the other being the organic-binder method.

(a) *Powder-in-tube method*: In this method, superconducting material is packed in a metal tube made from relatively inert material such as Ag, and the tube is either extruded or drawn. Besides providing a sheath in which compaction occurs, the Ag tube supplies the ductility necessary for drawing. The compaction is, however, greater in extrusion. The attainable reduction in wire diameter depends on the thickness of the Ag tube, which tears under large reductions, while the uniformity of the wire cross-section along its length depends on uniform rates of drawing or extrusion.

The fabrication of long wires requires continuous processes in which the wire is slowly moved along a tube furnace with a hot zone matched to require sintering temperatures. Oxygenation can be induced in the cooler zone towards the edge of the furnace, depending upon the sample being used. Multifilament wires can be formed by repeated extrusion of tubes filled with bundles of previously reduced wires.

(iii) ***Tapes formation***: Tapes present the greatest promise for bulk high T_c materials in applications requiring large current flow. This is because Bi-2223 and Bi-2212, which grow with platellar morphologies, can be aligned in tapes.

Tapes can be formed either with Ag sheaths or with organic binders. Plate-shaped particles in Ag-sheathed wire can be aligned by the mechanical stress applied in rolling. With repeated sintering and grain growth interspersed with a gradual reduction in tape thickness, high performance tapes can be formed into long lengths or coils.

Slurry containing superconducting powder is mixed with

(a) An organic binder,

(b) A solvent to regulate the viscosity of the slurry,

(c) A deflocculant or wetting agent and

(d) A plasticizer to prevent cracking in the green phase before sintering.

The slurry is poured onto a moving organic carrier film and passed under a '*doctor blade*', which scrap the film of uniform thickness. The film is dried, formed into its final shape and sintered. The highest J_c in bulk high temperature superconductors have been recorded from Ag-sheathed tapes.

(iv) ***Coils***: Superconducting coils for producing magnetic fields require materials which pass high current densities, and which have mechanical strength sufficient to withstand large Lorentz forces. High T_c coils have potential for uses either as resistance less coils with simple cryogenic requirements, or as inserts for conventional, low-temperature, high field magnets. The requirement for high currents implies that the high T_c material must be textured. Moreover, the anisotropic transport found in high T_c materials can be used to advantage in the flat ribbon geometry to avoid severe flux creep, which occurs when the field direction is perpendicular to the ribbon surface.

To provide the necessary mechanical strength, the coil is contained in a steel sheath and impregnated with epoxy resin. The layers of tape are insulated by glass fiber.

2.1.2 Synthesis of Thin films

The fabrication of high T_c thin films is motivated by their potential applications in electronic devices, sensors, bolometers, interconnects etc. It is generally assumed that high T_c thin films should, if properly prepared, have properties approaching those measured in single crystals. In low T_c material, that is not a valid assumption. The majority of high T_c thin films have been made is of Y-123 because

stoichiometry can more easily be reproduced in these compounds than in Bi-based superconductors. The Tl-based superconductors also have the disadvantage in producing thin films along with the toxicity and volatility of Tl.

For the purpose of device fabrication, it is necessary that thin films should be easily reproducible, with transition temperatures close to those observed in bulk material and with comparable transition widths. Also, the thin films should be compatible with conventional electronic devices grown on Si or GaAs for inter connectivity in electronic circuits. The growth of high quality thin films depends on the following conditions.

(i) ***Deposition environment***: Base vacuum and the annealing play a vital role in modifying the properties of the thin films. High T_c films grown *in-situ* superconduct on removal from the vacuum chamber. Film grown *ex-situ* are removed from a deposition chamber and placed in a reaction chamber, where they are annealed in oxygen-rich environment to form the superconducting phase. *In situ* films are grown layer by layer on heated substrates, with surface diffusion playing an important role, enabling the atoms to migrate to their equilibrium sites. *Ex situ* films are deposited in the amorphous state, and the crystal structure of the superconductor is formed subsequently by bulk diffusion with solid phase epitaxy during an anneal. The bulk diffusion process requires higher processing temperatures than are needed for the surface diffusion *in situ*. *Ex situ* films are often deposited onto cold substrates using a simple experimental arrangement.

(ii) ***Oxygen pressure***: The composition of compounds formed during deposition depends on partial oxygen pressures. For example, during the deposition of Y-123 superconductors, all the deposition techniques, which operate at higher substrate

temperatures and higher oxygen partial pressure, favor the formation of $YBa_2Cu_3O_6$. This compound is subsequently transformed to superconducting, orthorhombic $YBa_2Cu_3O_{7-\delta}$ by annealing in O_2 at pressures between 10^{-1} to 10^{-3} Torr.

(iii) ***Stoichiometry***: Prior to deposition, the elements can be evaporated from a single source or from multiple sources. Whichever is used, the properties of the resulting films, including T_c, transition width ΔT_c, and J_c depend critically on the stoichiometry of the deposited film. With good deposition monitoring and with good control, stoichiometric compositions can be achieved from multiple sources though deposition from a single source is less complex and less expensive. The deposition from single source is more reproducible.

(iv) ***Co-deposition from multiple sources***: In thermal evaporation from substrates of Y-123 powders, for example, elemental evaporation rates and sticking factors are not uniform, so that stoichiometry is lost. These problems can be overcome by co-evaporation from multiple sources. In this case especially, *in situ* monitoring of evaporation and deposition rates is required for fabrication of reproducible, high quality films.

(v) ***Substrates***: Among the most important considerations in processing high quality films is the selection of substrate material. The substrates must be available as large single crystals. The ideal substrate should have the following properties [6-8]:

(a) A smooth, clean surface, free of twins and other structural inhomogeneity;

(b) Matched lattice parameters between substrate and film;

(c) Chemical compatibility

(d) Matched coefficients of thermal expansion;

(e) No phase transformations between room temperature and deposition or annealing temperatures; and

(f) Electrical properties, such as dielectric constant compatible with required applications.

Lattice parameter mismatch results in coherency strains in the films. The corresponding stress leads to cracks or micro-cracks, which increase in magnitude and frequency with increasing film thickness. *Ex situ* crystal growth during post-deposition annealing is accompanied by diffusion, so chemical compatibility is required between substrate and thin film. Substrates, which undergo phase transformations during annealing cycles or which have different coefficients of expansion from that of the thin film also produce defects in the deposited film.

Commonly used substrates and growth planes are $SrTiO_3$ (100) or (110), MgO (100), YSZ (100) – Yttrium stabilized Zirconia, Al_2O_3 ($1\underline{1}02$), $LaAlO_3$ (100), $LaGaO_3$ and $NdGaO_3$ (100). The properties of some of these commonly used substrates are listed in Table 2.1. All these substrates are available in singe crystal form. Films of Y-123 have been successfully grown on polycrystalline substrates, including Hastelloy, stainless steel and YSZ [9].

(vi) ***a - axis films***: On substrates of (100) orientation, epitaxial growth normally occurs with the thin film c-axis normal to the plane of the film. However, processing conditions can control the orientation of the films. This is particularly true in the case of Y-123 in which the c-parameter is close to three times the ‘a’ or ‘b’ parameters.

Table 2.1 ***Properties of some commonly used substrates for the deposition of high T_c superconducting thing films***

Substrate	**Structure**	**a-axis lattice parameter 'a' (in nm)**	**Melting point (mp in ^{0}C)**
$SiTiO_3$	Cubic (perovskite)	0.3905	2080
$LaAlO_3$	Rhombhohedral (perovskite)	0.3793	2100
$LaGaO_3$	Orthorhombic (perovskite)	0.3890	1750
MgO	Cubic (NaCl)	0.4213	2800
YSZ	Cubic	0.5240	2700
Sapphire	Trigonal	0.4758	1370
Si	Cubic (diamond)	0.5431	1150
GaAs	Cubic (zincblende)	0.5650	1238

(vii) ***Heterostructures***: Heterostructures are compounds containing alternating layers of different compounds e.g., $YBa_2Cu_3O_{7-\delta}$ / $PrBa_2Cu_3O_{7-\delta}$ [10]. Heterostructures must be grown by *in situ* methods, in order to limit bulk diffusion. The T_c s of these structures depends on the thickness of both the $YBa_2Cu_3O_{7-\delta}$ and $PrBa_2Cu_3O_{7-\delta}$ layers. Heterostructures can be produced by selection of deposition temperatures, with either c- or a-axis orientation.

(viii) ***Film Quality***: The quality of the films can be checked in many ways. Comparison of T_c s and J_c s with those of single crystals is a normal first step.

Frequently, the sharpness of the drop in magnetic susceptibility at the superconducting transitions,$\Delta\chi$, and the minimum value of the real part of the magnetic susceptibility, χ_{min}, recorded at temperatures below T_c, provides a further guide to film quality. The morphology of an ideal epitaxially grown film is flat and featureless. In practice, pinholes, surface roughness and other defects are usually observed. They affect electrical and magnetic properties of the films depending on the size of the defects.

Different deposition techniques: Most of the deposition techniques employed for the synthesis of high T_c superconducting thin films was previously used for the depositions of thin films of semiconductors. The techniques are based either on Physical Vapor Deposition (PVD) or on Chemical Vapor Deposition (CVD). Different deposition techniques, which are commonly used for the synthesis of thin films, are as follows

(a) ***Thermal Evaporation***: The simplest deposition technique involves thermal evaporation from a single source, e.g., of Y-123 alone or of Y-123 with selected additions. In single source evaporation there is little control over deposition rates, so that films are often deficient in one or more elements. Individual elements are contained in furnaces and their vapor fluxes controlled through individual furnace temperatures. A typical chamber is pumped by a turbo molecular pump and by cryo panels. A deposition rate between 0.1 and 1 mm/s is normally achieved.

In its most sophisticated form, ***Molecular Beam Epitaxy (MBE)*** occurs layer by layer, controlled by shutters. Artificial compounds, not possible in bulk form, can be fabricated. For epitaxial growth, the specimen substrate is mounted to a heater

holder and is tilted toward each furnace in turn during evaporation. To grow films *in situ*, oxygen is fed into the chamber and plasma is formed by high-tension discharge close to the specimen and substrate. The atomic structure of the film is monitored by ***Reflection High-Energy Electron Diffraction (RHEED)*** of electrons directed towards the specimen at a glancing angle from an electron gun. Electron beam (e-beam) evaporation requires high vacuum at pressures $\approx 10^{-4}$ Pa, so that, for *in situ* growth with a reactive gas, differential pumping is needed between the specimen and target. Alternatively, electron beam evaporation is well suited to *ex situ* methods.

(b) ***Sputtering***: Sputter deposition of thin films is carried out at pressures, from 1 to 100 Pa, considerably higher than those used in thermal or e-beam evaporation. A working inert gas, usually Ar, is introduced into the sputtering chamber. The sputtering gas may contain some oxygen. Plasma is created either by dc discharge or by RF excitation. A typical rf coil operates at 2 MHz and 5 kV, Ar^+ ions are accelerated out of the plasma by the potential of the target, and they strike the target, releasing atoms, which are collected on the substrate to form the film.

Sputtering is performed either with a single target or with multiple targets. In the simplest configuration, the substrate faces the target. This is known as *on – axis* sputtering, and typically deposition rates are more rapid than 0.1 nm/s. In *off-axis* sputtering, the substrate is oriented at 90 ^{0}C with respect to the target so as to lie outside the plasma to avoid resputtering effects, but the deposition rates are low, around 0.03 nm/s.

In magnetron sputtering, the plasma, excited by either an rf or dc potential, is confined by the magnetic field produced by a permanent magnet. The resputtering

problem is solved in this method by using an 'unbalanced' magnetic field configuration. Under dc operation, the discharge typically runs at about 115 V and 1.2 A. For *in situ* films, sputtering occurs in Ar/O_2 atmosphere typically above 1 Pa. The system can also be used to produce *ex situ* films.

A typical dc sputtering arrangement consists of a vacuum chamber for *in situ* deposition with a heated substrate, a shutter and several sputtering targets operated by dc or rf power. Flow controllers are used to define the Ar and O_2 gas mixtures.

(c) ***Laser Ablation***: When a pulsed excimer laser, with energy fluence about 3 J/cm^2, is focused onto target material, ablated species including atoms, molecules and radicals are transferred to the nearby substrate [11, 12]. The Figure 2.1 shows the typical experimental arrangement of deposition by laser ablation.

The laser optics are contained outside the vacuum chamber, with the entry widow is often geometrically shielded from ejected material. The pressures of reactive gases, such as O_2 or N_2O, are adjustable and may be as high as 0.5 atm. The target is typically oriented at 45^0 to the beam. The ablated species are emitted in a plume with maximum emission normal to the target surface. The substrate is normally heated to enable epitaxial film growth. Deposition rates up to 10 nm/s are obtainable in high quality films. The deposition rate depends on the pulse repetition rate, which depends simply on what is commercially available; say around 10 Hz. Higher repetition rates allow faster growth rates. Figure 2.1 shows gives a typical laser ablation setup, which is generally used for depositing thin films using a single target holder, or multiple target holders.

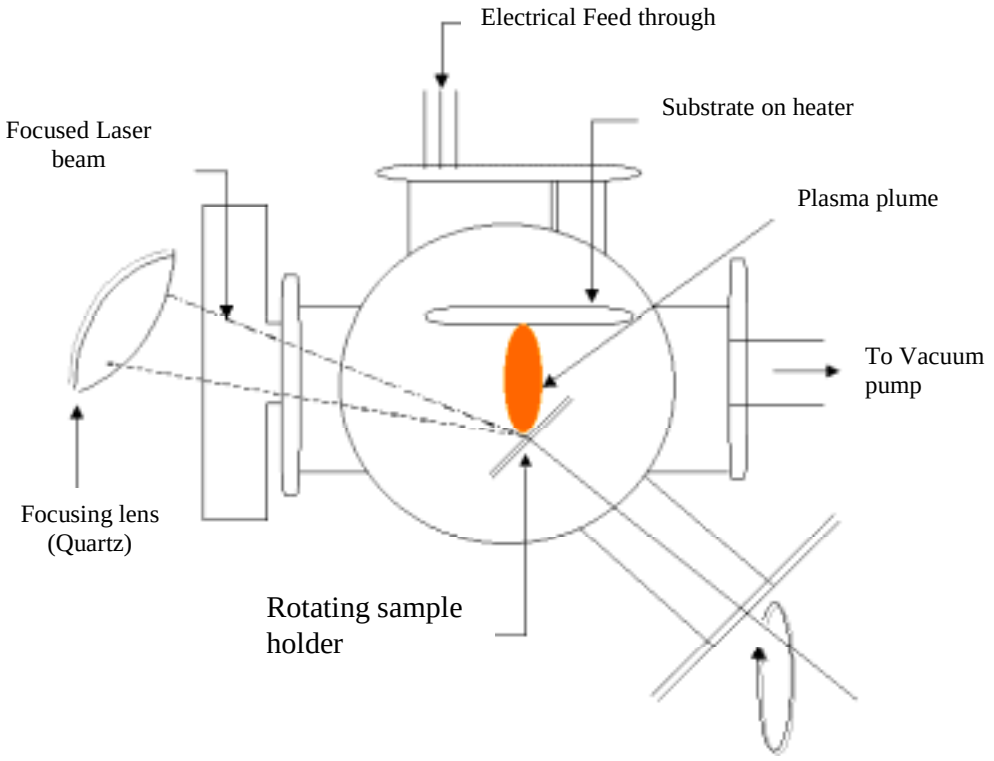

Figure 2.1 Schematic representation of a PLD setup for laser ablation

Each pulse of laser energy causes localized melting and evaporation, and leaves a crater in the target. The crater contains resolidified melt with various phases, so the target is moved between pulses to preserve stoichiometry in the deposited film. If the target is made of porous material, particulates are ablated and deposited on the substrate along with atoms, molecules and radicals. The deposition of particulates is alleviated by the use of dense targets.

(d) ***Chemical Vapor Deposition***: All the techniques discussed above were physical vapor deposition methods (PVD). The draw back of PVD method is that deposition rates are generally slow, and vacuum apparatus is required. Often only small areas of film can be deposited with uniform composition. High quality thin films have been made by MOCVD (metal-organic chemical vapor deposition). It is

comparatively simple to deposit large-area thin films rapidly by this technique. The technique depends on the production of volatile metal-organic precursors as sources of the metal elements. Properties required in a suitable precursor include

(i) Sufficiently high vapor pressure for vapor transport;

(ii) Stability at operating temperatures without losing volatility; and

(iii) Stability at room temperatures for long-term storage.

The chief difficulty experienced in MOCVD is the identification of suitably volatile metal-organics, particularly for Ba. Also some contamination from the organics is inevitable and does degrade the properties of the films when compared with those made by physical vapor techniques.

(e) ***Metal-organic Solution Deposition***: One of the most successful condensed states *ex situ* deposition techniques is the metal-organic solution deposition method. A solution of metal-organics is coated onto a spinning substrate, which is subsequently heat-treated to form a superconducting film. For example, 2-ethylhexanoates of Bi, Ca and Cu and strontium cyclohexanoate are used for forming Bi-2212. Films can be formed on various substrates including stainless steel with a buffer layer, e.g., of HfO_2, Ag and single crystal MgO. After deposition the films are annealed in air at 845^0C. The current densities of these films are several orders of magnitude lower than those measured for thin films deposited by PVD, supposedly due to the residual carbon contamination.

2.2 STRUCTRUAL STUDIES

For the understanding of superconductivity in cuprate superconductors, it is necessary to understand the crystal chemistry, which actually determines the property

and structure of the superconductors. The crystal structures are derived mainly from X-ray powder diffraction patterns, but they can also be derived from single crystals. Neutron diffraction has been the most powerful method for structural determination because the scattering cross-sections are significant for all of the atoms occurring in the high T_c materials whereas in X-ray and electron diffraction, the cross-sections are strongly weighted towards the heavier atoms. The cross-sections depend on the wavelengths of radiation used. The Table 2.2 briefly gives the idea of the discrepancies in the values of mass absorption coefficients for various elements.

A second reason for the comparative usefulness of neutron diffraction in structural analysis is the smaller absorption coefficients than corresponding coefficients in X-ray and electron diffraction. In the following sections, a review of the present day techniques widely used for structural studies is discussed.

2.2.1 ***X-ray diffraction***: The easy availability and accessibility of X-ray diffraction makes it a useful technique not only for phase identification, but also for initial identification of lattice structure and for modeling of the basic unit cell.

The wavelengths of the X-rays are of the order of the inter-atomic distances in the crystal, which are of the orders of few Angstroms. Hence, the X-rays scatter very well from the array of atoms from a crystalline structure. The property of crystals, i.e., the repeated arrangement of atoms appears as a grating to the imping X-rays, hence the outgoing X-rays forms a diffraction pattern. Just as in optical diffraction pattern, X-rays interfere destructively except at points where special conditions are met.

Table 2.2 ***Mass absorption coefficients (μ / ρ) and Linear absorption coefficients (μ) for various elements and systems respectively***

	μ / ρ		μ		
Element	**Neutrons (1.08 Å)**	**X-rays (1.54 Å)**	**Compound**	**Neutrons (1.08 Å)**	**X-rays (1.54 Å)**
O	10^{-5}	11.5	$La_{1.85}Ba_{0.15}CuO_4$	0.13	1717
Cu	2.1 X 10^{-2}	52.9	$La_{1.85}Sr_{0.15}CuO_4$	0.13	1642
Sr	5.0 X 10^{-3}	125	$YBa_2Cu_3O_7$	0.05	1091
Y	6.0 X 10^{-3}	134	$YBa_2Cu_3O_6$	0.05	1074
Ba	2.6 X 10^{-3}	330	$Bi_2Sr_2Ca_2Cu_3O_{10}$	0.033	932
La	2.3 X 10^{-2}	341	$Bi_2Sr_2CaCu_2O_8$	0.027	1024
Pb	3.0 X 10^{-4}	232			
Bi	6.0 X 10^{-5}	240			
Ca	3.7 X 10^{-3}	162			

If we consider a crystal as a series of planes with their inter-atomic distance being'd'. Then the incoming X-ray, with wavelength, λ, will undergo scattering and interfere constructively only with that from adjacent planes at special angles 'θ', that meet the *Bragg condition*,

$$\mathbf{n.\lambda = 2dsin\theta}$$

A crystal contains parallel planes along three different axes, so the actual measured values of θ vary with the alignment between the crystal planes and the incoming beam of X-rays. A plane perpendicular to the crystallographic a-axis is called the [100] plane; one perpendicular to b-axis is called [010] plane, and so on.

For complicated crystals like, the triple perovskite HTSC s, there are many choices of planes that can contribute to the X-ray diffraction pattern.

With the knowledge of chemical composition of a solid and of ionic sizes, structural models can be built and used in refinement procedures with either X-ray or neutron diffraction spectra. One of the building blocks commonly used in the structural models is the $CaTiO_3$ (or ABO_3) cubic perovskite structure. The building block is similar to the cube centered on Ba in Y-123, with charges being balanced by adjacent layers. Other building blocks used in structural models are K_2NiF_4 layered perovskite structure (i.e., the structure of La_2CuO_4) and $Bi_4Ti_3O_{12}$ Auruvillius structure.

2.2.2 ***SEM & EDAX***: Scanning Electron Microscope (SEM) is one of the important tools to identify the micro structural properties of the HTSC compounds since like many other physical properties, superconductivity in HTSC ceramics depends on microstructures. SEM is the workhorse of micro-structural characterization. This is because of the variety of signals that can be recorded, each providing its own peculiar information, including elemental analysis by *energy-dispersive x-ray spectroscopy* (***EDAX***). The two signals most commonly used in SEM imagining are the secondary electron signal and the backscattered signal. These two signals provide different information corresponding to the different physical processes involved.

From the SEM studies, structural information can be obtained from microscopic areas of specimen with resolution approaching 0.1 mm. This is partly because electron scattering cross-section is large compared to those of X-rays and neutrons. Heavy elements scatter electrons more than the lighter ones. Absorption coefficients are also generally high. In consequence, the specimens must be thinned

and viewed in transmission. Diffraction angles are small owing to the short wavelengths of high-energy electrons typically $\lambda \sim 10^{-12}$ m in an electron microscope.

2.2.3 ***Neutron Diffraction***: Neutron scattering cross-sections are generally so small that large specimens are required for structural analysis, i.e., much larger than the single crystals of high T_c materials that can be homogeneously grown. Diffraction patterns are therefore obtained from compressed powders or sintered pellets. The powder diffraction patterns are used to identify the Bravais lattice, and from this an informed guess is made concerning the detailed crystal structure. In the case of cuprate superconductors the information required is, the conditions required for perovskite (ABO_3) and layered perovskite (K_2NiF_4 structure) building blocks for the lattice. Structural refinement proceeds by fitting calculated structure factors for diffraction from structural models to diffraction data, and by adjusting atomic sites and occupancies. During the structural refinement, instrumental and theoretical line widths and shapes are taken considered. Either a neutron beam with a wide energy spread is directed onto a specimen and diffracted beams recorded at a single scattering angle as a function of wavelength or the beam is first monochromated and the diffracted beams recorded as a function of scattering angle.

Neutron scattering is a powerful tool for investigating other features of high T_c systems. The magnetic moment of the neutron can be used to probe spin states in the compounds. Neutrons are also powerful tool for examining phonon densities of states. It has been found, in the case of Y-123, that significant changes occur when $YBa_2Cu_3O_6$ transforms to $YBa_2Cu_3O_{7.}$

2.2.4 ***Atomic Force Microscopy***: As compared to SEM, Atomic Force Microscopy (AFM) provides extraordinary topographic contrast, direct height measurement and unobscured views of surface features without any coating [13]. AFM is being used to solve processing and materials problems in a wide range of technologies affecting the electronics, telecommunications, biological, chemical, automotive, aerospace, and energy industries. AFM can be used to investigate thin and thick film coatings, ceramics, composites, glasses, synthetic and biological membranes, metals, polymers and semiconductors. AFM is also used to study the phenomena such as abrasion, adhesion, cleaning, corrosion, etching, friction, lubrication, plating, and polishing. By using AFM one can not only image the surface in atomic resolution but also measure the force at nano-newton scale. Like all other scanning probe microscopes, the AFM utilizes a sharp probe moving over the surface of a sample in a raster scan. In the case of the AFM, the probe is a tip on the end of a cantilever, which bends in response to the force between the tip and the sample. AFMs can achieve a resolution of 10 pm, and can image samples in air and under liquids.

2.3 TRANSPORT MEASUREMENTS

In the case of high temperature superconductors, no consistent theoretical framework exists to the present day, which can describe all the typical transport properties. In the concentration range corresponding to improved superconducting properties, where normal transport properties look somewhat metallic, most of the discussion is usually in the framework of semi-classical approximation, which is described by the Boltzmann transport equation:

$$v\Delta_r f + F\frac{1}{\hbar}\Delta_k f = \left(\Delta_t f\right)_{collision}$$

The above equation describes, the modifications introduced by the external driving forces (***F***) and by single electron scattering on the local distribution of carriers (***f(r, k)***) as a function of the real (***r***) and momentum space (***k***). In this model, it is assumed that the steady state (***f***) that corresponds to the state of the system after a response to external forces does not depart very far from the equilibrium state.

However, in the regime of low conduction, the transport properties are often described in terms of hopping conduction. The resulting model, principally based on the work of Hubbard, Mott and Anderson, describes the situation where either disorder or electron-electron correlation becomes important and may even result in localization of charge carriers.

2.3.1 ***R-T measurements***: The dc resistivity of a sample is measured by the voltage drop across a specimen when a current of known magnitude, which is typically around 1 mA, passes. The terminals used for measuring the voltage pass little current when connected to a high impedance voltmeter. These terminals are distinct from those used for passing the main part of the current through the specimen, where voltage drops in both leads and contacts are significant. The Figure 2.2 shows a schematic diagram of four probes connected to a specimen whose temperature is measured by a temperature sensor in thermal contact with the specimen [14].

A similar four-probe apparatus can be used for elementary measurements of J_c, defined according to the sensitivity of the apparatus or to a selected criterion. In bulk material, the specimen, e.g., Y-123 is mounted on a thermally compatible, insulating substrate (say quartz film) for mechanical strength. The contacts must have low resistance to reduce heating effects. The heating effect of the high currents at contacts and neck is further reduced by use of a pulsed current source. Starting with a low

current, this is increased until the voltage drop, observed with a rapid voltage monitor, such as an oscilloscope, reaches a defined level corresponding to E_c.

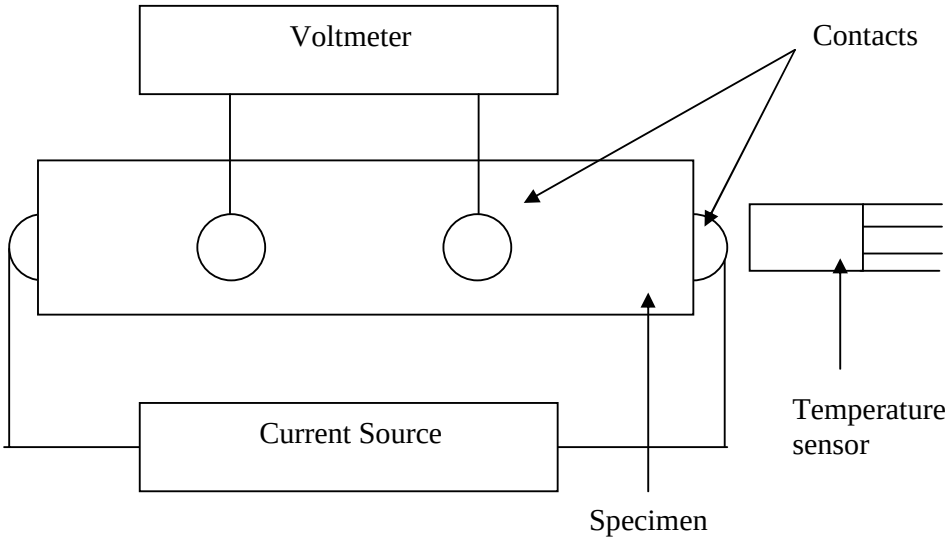

Figure 2.2 Schematic diagram of a four-probe setup

A C resistivity can be measured by a similar four-probe arrangement, but using an a.c. current source and lock-in amplifier for voltage measurement. Signal noise is reduced by the use of a preamplifier close to the specimen. Alternatively, if a specimen is biased with voltage V and microwave ac frequencies ν applied across a junction, the ac Josephson effect is observed.

2.3.2 ***Specific Heat studies***: The specific heat measurements provide useful information about the electronic and vibrational excitations present in the sample both, in the normal state above T_c and superconducting state below T_c. Specific heat measurements are usually performed with standard heat pulse technique using an adiabatic calorimeter (relaxation method) [15, 16].

2.3.3 ***Thermo power measurements***: The thermo electric power (TEP) studies offer a sensitive probe to understand the nature of charge carriers participating in the

transport mechanism of high T_c superconductors. The sign of TEP gives an indication of the nature of charge carriers in the sample. For HTSC samples this sign is generally positive, indicating that the charge carriers in HTSC are holes.

2.3.4 ***Thermal conductivity***: For understanding theoretically, the electronic and vibrational properties of the HTSC materials, it necessary to understand the thermal conductivity of these materials. The thermal conductivity of the superconductors provides information about how efficiently and by what means does the heat flows in these superconductors. The magnitude and temperature dependence of the thermal conductivity are parameters, which have an impact on a broad spectrum of superconducting devices. It provides information about the charge carriers and phonons and scattering process between them. The traditional *galvanometric* and *thermoelectric probes* such as the electrical resistivity, the *Hall effect* and *thermoelectric power* are inoperative in the wide temperature range below T_c. the contributions from the electronic K_e and the lattice K_g yields the thermal conductivity K as;

$$\mathbf{K = K_e + K_g}$$

While the phonon contribution is always present, the magnitude of the carrier contribution depends on the type of solid because it is directly proportional to free carrier density and to their mobility.

2.4 MAGNETIC MEASUREMENTS

Magnetic properties of superconductors represent the bulk behavior of the sample, while resistivity properties depend on the microscopic nature of the sample. Magnetic properties can be measured in either applied a.c. or d.c. fields.

2.4.1 ***a.c. susceptibility***: Susceptibility is the ratio of the intensity of magnetization (M) to the applied magnetic field (H), given as

$$\chi = \mathbf{M} / \mathbf{H}$$

while measuring the a.c. susceptibility, the real and imaginary parts of magnetic susceptibility can be conveniently measured with a mutual inductance susceptometer containing null-balance sense coils. Figure 2.3 is a schematic block diagram showing the arrangement of coils and specimen. The primary coil is connected to an a.c. current source. Two secondary coils are wound in opposition so that the field induced by the primary produces, after compensation adjustment and specimen withdrawal, zero potential, V = 0, at a step-up transformer which feeds a lock-in amplifier. When a specimen is introduced into one of the secondaries, the phase and voltage of the signal received by the lock-in amplifier are fed to a computer, and signals are recorded as a function of specimen temperature.

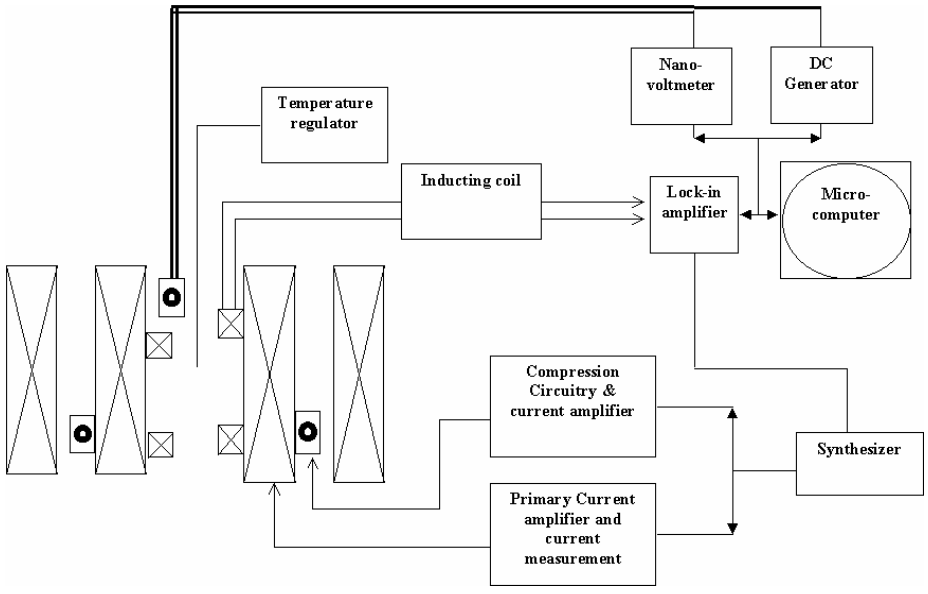

Figure 2.3 ***Block diagram of susceptibility apparatus showing magnet configuration with a.c. current source and detection*** [17]

In order to measure the field dependence of the susceptibility, superconducting coils are energized to provide uniform field around the specimen. The magnitude of the off-balance, induced voltage, V, depends on the rate of change of magnetic flux given by

$$|\mathbf{V}| = | -d\phi/dt | = \zeta n_1 \nu \mu_0 H_0 \omega | \chi |$$

Where, ζ is a filling factor, n_1 is the number of turns in the secondary coil, ν is the volume of the sample, H_0 is the amplitude of the applied ac magnetic field, and ω is the angular frequency. $| \chi |$ is the measured susceptibility, which approximates to the true susceptibility when the specimen is small and demagnetizing fields can be ignored. For a type I superconductor, when $B < B_c$, $\chi = -1$. The d.c. coil is not essential to measure the susceptibility of the sample at low fields because a field is applied by the primary coil. The response in the secondary coils is generally out of phase with the impulse supplied by the primary coil. The real and imaginary parts of the magnetic susceptibility, measured from the voltage induced in the secondary coils vary with the applied field strength. The real part, in phase with the current in the primary coil, corresponds to a diamagnetic moment, which screens the applied field from the specimen core. The imaginary part, out of phase with the current in the primary coil, is the part of the response due to energy loss by resistive heating of flux motion, eddy current losses, surface losses, etc.

2.4.2 ***d.c.susceptibility***: D.C. magnetic susceptibility measurements can be used to determine the superconducting volume fraction in a given material. In the simplest case, the Meissner effect compels the susceptibility of a homogeneous Type I superconductor that contains no trapped flux to be –1. In inhomogeneous materials the superconducting volume fraction can be a fraction of –1 for several reasons,

including insulating second phases, voids, non-superconducting grain boundaries, surface flux penetration, inhomogeneities in layered unit cells, etc. Measured susceptibility is further increased if magnetic flux is trapped in the specimen.

2.4.3 ***d.c.magnetization***: At higher field strengths the magnetization produced in a specimen by a d.c. coil can be used to characterize the superconducting material. This is commonly by two methods, one by using VSM (vibrating sample magnetometer) and SQUID (superconducting quantum interference device). Both the methods employ the voltage induced in secondaries by movement of the specimen.

(a). **SQUID**: In the SQUID magnetometer, the cooled specimen is drawn slowly through two secondary coils, wound in opposite direction. The field induced in the coils is amplified by a transformer and the flux change detected by a SQUID device, when this device is used as a null field detector with a feedback circuit, it is sensitive to individual quanta of magnetic flux.

(b). **Vibrating Specimen magnetometer**: The specimen is typically immersed in a magnetic field and attached to a rigid rod which is made to vibrate by a piezoelectric crystal or by an ac driven electromagnet. A lock-in amplifier connected to a detection circuit detects the a.c. field induced in secondary coils. The response is rapid so that the magnetization of the specimen can be measured in a continuously swept field.

2.4.2 ***Hall effect***: The basic physical principle underlying the Hall effect is the Lorentz force. When an electron moves along a direction perpendicular to an applied magnetic field, it experiences a force acting normal to both directions and moves in response to this force and the force effected by the internal electric field. Assume that a constant current I flow along the x-axis from left to right in the presence of a z-directed magnetic field. Electrons subject to the Lorentz force initially drift away

from the current line toward the negative y-axis, resulting in an excess surface electrical charge on the side of the sample. This charge results in the Hall voltage, a potential drop across the two sides of the sample. (Note that the force on holes is toward the same side because of their opposite velocity and positive charge.) This transverse voltage is the Hall voltage V_H and its magnitude is equal to IB/qnd, where I is the current, B is the magnetic field, d is the sample thickness, and q (1.602×10^{-19} C) is the elementary charge. In some cases, it is convenient to use layer or sheet density ($n_s = n_d$) instead of bulk density. One then obtains the equation

$$\mathbf{n_s = I.B/q.\ |V_H|}$$

Thus, by measuring the Hall voltage V_H and from the known values of B, q, and I one can determine the sheet density n_s of charge carriers in superconductors.

2.5 OXYGEN CONTENT DETERMINATION

The properties of the mixed oxide systems are very sensitive to the value of oxygen present in them. Since, oxygen is important for both structure and properties of the high temperature superconductors, it is imperative to have a reliable oxygen determination method, to ensure that the structure – property correlation exists and can be explained accordingly. In the following section an attempt is made to highlight the few of the present day reliable oxygen content determination techniques.

2.5.1 ***Iodometry***: In volumetric analysis, a standard solution of the reagent is put in a measuring vessel known as burette and is then gradually added to the solution to be analyzed (in a titration flask). The process is continued until it is found by a suitable

method that the amount of reagent, which has been added, is equivalent to the substance being determined. This operation is called *Titration* and, therefore, volumetric analysis is also called **titrimetric analysis** or **titrimetry.**

Therefore, one of the solutions is taken in a burette and the second is taken in the titration flask. The exact point at which a chemical reaction is completed during the titration is called the **end point** or **equivalent point**. In order to determine the completion of the reaction (or end point) a substance is used known as **indicator**. These show changes in color just at the stage when the reaction is complete.

The reactions involved in titrimetric analysis may be divided into two main types:

(i) The reactions in which no changes in oxidation state occur. These simply undergo combination of ions.

(ii) The reactions in which there is change in Oxidation State or other wise expressed as transfer of electrons.

For the purpose of convenience, the above two types of reactions are divided into the following four types:

(a) Acid-base titration (Acidimetry and alkalimetry): These involve titrations of free acids or those formed from salts of weak bases by hydrolysis with a standard base (alkalimetry) or a titration of a free base or those formed from salts of weak acids by hydrolysis with a standard acid (Acidimetry). We know that an acid-solution has pH value less than 7 while a basic solution has a pH value greater than 7. Therefore, when an acidic solution is reacted a basic solution, its pH changes. These pH changes can be measured by different

methods. Generally volumetric titrations involving acid-base reactions are carried out by the following methods:

1. Visual method,
2. Electrical conductivity method,
3. E.m.f. titrations.

(b) Oxidation reduction (or redox) titrations: Oxidation involves loss of electrons while reduction involves gain of electrons. In these titrations an oxidizing agent (accepting electrons) is titrated against a reducing agent (losing electron). Such types of reactions in which oxidation and reduction occur at the same time are called ***Redox reaction*** and titrations involving redox reactions are called ***redox titration***.

Our interest is in the study of reactions involving iodine. The redox reactions involving iodine are of two types:

Iodimetry: The titrations involving the direct use of iodine solution are called iodimetry. The iodine solution is used to estimate reducing agents such as Sodium thiosulphate, sodium sulphite, arsenites, antimonates, etc.

Iodometry: The titrations involving the titration of iodine, which is liberated in a chemical reaction [18, 19]. In iodometry, a solution of I_2 in KI is used as

$$KI + I_2 \Leftrightarrow KI_3$$

In this reaction iodine is liberated from KI by strong oxidizing agents such as $KMnO_4$, $K_2Cr_2O_7$, H_2O_2 and Cu^{2+} ions and then liberated iodine is estimated by titration against standard sodium thiosulphate solution. For example, to estimate the strength the $KMnO_4$, the solution of known volume of $KMnO_4$ is taken in the titration flask.

About same volume of dil. H_2SO_4 is added to the solution and then 10% solution of KI is added. The liberated iodine is titrated against standard solution of $Na_2S_2O_3$.

In iodometry and iodimetry, ***starch*** is used as an indicator, which gives intense blue color at the end point. This intense blue color is due to the formation of a complex I_2 with the starch in the presence of iodide ions.

2.5.2 ***T.G.A and D.T.A***: **Thermo Gravimetric Analysis** (T.G.A) is another method for the determination of oxygen content in the oxide superconductors [20]. This method gives the amount of oxygen in the starting material, from the weight loss observed in the compound as a function of increasing temperature, under the reducing atmosphere (usually N_2 or Ar).

Differential Thermal Analysis (D.T.A) gives the information about the type of reaction (endothermic or exothermic reaction) taking place in the sample as a function of temperature. This technique, along with the analysis of the XRD date for phase formations, gives a clear understanding of the chemistry and structure of high T_c superconducting oxides. D.T.A relies on the fact that the heat is evolved or absorbed during a phase change. By observing temperature changes due to this heat transfer, one can summarize that a phase change is taking place.

2.5.3 ***E.R.D.A***: Elastic Recoil Detection Analysis (E.R.D.A) is a technique specially suited for the depth profiling of lighter elements overcoming the limitations of the RBS (Rutherford Back Scattering) technique [21]. RBS provides depth profiling, using alpha particles of energy of few MeV's, on surface of few microns. RBS channeling measurement allow the quantification of crystallization, dopant atom location, determination of strain in superlattices, etc. RBS has poor sensitivity to the detection of light elements such as, C, N and O in the presence of substrate (used in

thin film depositions) due to low Rutherford scattering cross-section, which is proportional to product of atomic numbers of the projectile and scatter. The disadvantages of RBS are overcome by ERDA, first demonstrated by L'Ecuyer et al, in 1976 [22].

Basically ERDA is similar to RBS technique, but instead of scattered projectile detection at back angle, the recoils are detected (resulting from elastic collision of the incident particle and the atoms in the sample) in forward direction. ERDA technique is further strengthened in terms of its capabilities by the use of particle identifying techniques. Some salient features of ERDA with the use of heavy ions are:

(i) Large recoil cross sections with heavy ions, hence good sensitivity,

(ii) Almost same recoil cross section for a wide mass range of target atoms,

(iii) Elemental depth profiling of a wide range of elements from hydrogen to rare earth elements using particle-identifying techniques.

2.5.4 ***Neutron Diffraction***: Neutron diffraction technique is one of the most prominent and reliable technique for the determination of the structure as well as the composition of the structure. Unlike in the case of X-rays, the scattering cross-section of neutron is very less. The scattering length of neutron is independent of atomic number (or the number of electrons surrounding the nucleus), but instead depends on the nuclear energy levels. Hence, the sensitivity of neutrons is same for all ions, except for neutron absorbers or killers. This enables, during analysis of the neutron diffraction data, to estimate and calculate the exact site occupancies of all constituent atoms, including the most important light ion in the case of mixed oxide superconductors, the oxygen. During the Rietveld refinement of the neutron data, the

oxygen content can be varied to see the marked changes in the diffraction pattern. The difference in X-ray diffraction and Neutron diffraction also lies in their sensitivities to light and heavy ions. The neutron diffraction patterns also indicate the peaks observed due to oxygen, which cannot be seen in the X-ray diffraction patterns.

REFERENCES

[1] A. Bourdillon and N. X. Tan Bourdillon
"High Temperature Superconductors – Processing and Science"
Academic Press Inc (1993)

[2] S. X. Dou, H. K. Liu, A. J. Bourdillon, J. P. Zhou, N. X. Tan, X. Y. Sun and C.C. Sorrell
J. Am. Ceram. Soc., **71C**, 329 (1988)

[3] J. A. Voight, B. C. Bunker, D. H. Doughty, D. L. Lamppa and K. M. Kimball
"High Temperature Superconductors" Edited by: M. Bordsky, R. C. Dynes, K. Kitazawa and H. L. Tuller, M.R. S, Pittsburgh (1987) p. 635

[4] T. L. Ward, T. T. Kodas, A. H. Carim, D. M. Kroeger and H. Hsu
J. Matter. Res, **7**, 827 (1992)

[5] C. J. Brinkered and G. W. Scherer
"Sol-Gel Science", Academic Press Inc, Boston (1990)

[6] R. W. Simon
"Processing of Films for High Temperature Superconducting electronics" Edited by T. Venkatesan, SPIE, Vol **1187**, (1989), Page 2

[7] R. D. Hilty and R. N. Wright
AIP Conference Proceedings, 291, Edited by Y. H. Kao, P. Coppens and H. S. Kwok, AIP (1991), Page 678

[8] S. Blakemore
J. Appl. Phys. **53**, R123 (1982)

[9] D. T. Shaw

M.R.S Bulletin, **17**, 39 (1992)

[10] D. H. Lownder, D. P. Norten and J. P. Budhai

Phys. Rev. Lett. **65**, 1160 (1990)

[11] H. S. Kwok, D. T. Shaw, Y. Ying, J. P. Zheng, S. Witanachchi, E. Petrou and H. S. Kim

"Processing of Films for High Temperature Superconducting Electronics"

Edited by T. Venkatesan, SPIE, Vol-**1187**, (1989), Page 161

[12] N. Biunno, J. Narayan and A. R. Srivatsa

Proc. SPIE, **1190**, 118 (1989)

[13] Hong-Qiang Li

"Introduction to Atomic Force Microscopy (AFM)"

On Internet - hli@uoguelph.ca (1997)

[14] L. J. Van der Paw

Philips. Res. Repots, **16**, 187 (1961)

[15] V. Gottwiek, R. Hela, G. Spam, F. Stejlich, H. Rietschel, D. Ewart, B. Renker, W. Baunoter, S. Vonmolar, M. Wilhelm and H. E. Huening

Europhys. Lett. **4**, 1183 (1987)

[16] J. Dutzi, S.M. Pattalwar, R. N. Dixit and S. Y. Shete

Pramana, **31**, 253 (1988)

[17] M. Couach and A. F. Khoder

"Magnetic Susceptibility of Superconductors and other spin systems"

Edited by R. A. Hein, T. L. Franeavilla and D. H. Liebenberg

Plenum, New York (1992), Page 25

[18] D. C. Harris and T. A. Hewston

J. Solid State. Chem. **69**, 182 (1987)

[19] E. H. Appelman, L. R. Morss, A. M. Kini, U. Geiser, A. M. Umezawa, G. W. Crabtree and K. D. Karlsen

Inorg. Chem., **26**, 3237 (1987)

[20] H. Verweij and W. H. M. Bruggink

J. Phys. Chem. Solids. **49**, 1063 (1988)

[21] D. K. Awasthi and W. Assmann

Curr. Sci., **80**, 1532 (2001)

[22] J. L'Ecuyer, C. Brassard, C. Cardinal and B. Terreault

Nucl. Instrum. Method. **B149**, 271 (1978)

CHAPTER – I I I

Characterization methods used

3.1 SYNTHESIS

During the course of the present work, La based mixed oxide superconductors of the type $La_2Ca_1Ba_2Cu_5O_z$ (La-2125) were studied in two forms, bulk and thin film. It was for the first time that an attempt was made to synthesize superconducting thin films of La-2125 composition. Owing to the stochiometric and property differences with the pristine La-123 type of superconductors, it is interesting to synthesize the La-2125 superconducting thin films. From the application point of view, a good film is that which possess all the features of the bulk sample. And for synthesizing a good film the first and foremost requirement is a very good quality bulk target, which can be easily reproducible and which possesses stable properties.

3.1.1 ***Synthesis of bulk samples***: All the bulk samples were synthesized by the standard solid-state reaction method following the route shown in the flowchart (Figure 3.1). For good quality of samples, high purity chemicals were taken in stochiometric quantities and ground thoroughly using an agate and mortar, to obtain a homogeneous mixture. As described in section 2.1, a homogeneous mixture increases the rate of peritectic reaction, thus giving a single-phase end product. The reaction temperature is chosen after considering the solid-solubility limits of all the constituent compounds. The first two heating schedules are called the ‘calcination’ cycles. It is done to ensure that all the ‘carbon’ is liberated from the mixture in the form of ‘carbon dioxide’. It is necessary since alkaline carbonates are used. Followed by calcination, the mixtures are ground thoroughly to obtain a uniform composition. The resultant mixture is then pelletized at 2-3 ton pressure. This ensures densification of the samples and uniform heating of the mixture during sintering.

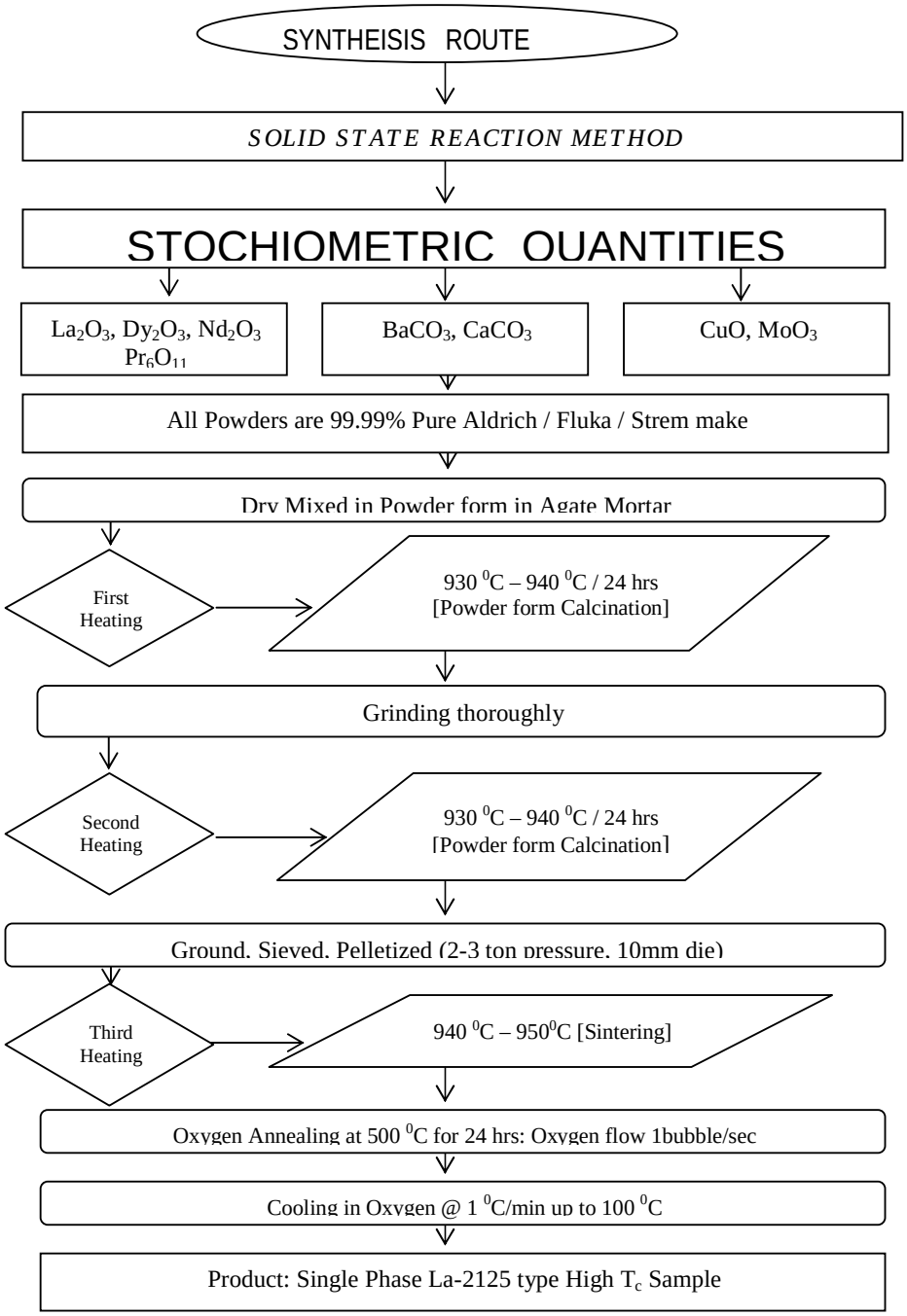

Figure 3.1 Flow chart for solid-state reaction method used for synthesis of bulk samples

Pelletization also helps in giving shape to the compound, which makes it easier to handle them. The sintering of the thus formed pellets confirms the shape

while it densify the compound, ensuring maximum reaction between the particles, since the distance between them gets reduced after pelletizing. The intermittent grindings and sintering of the samples are essential to form single-phase high T_c compounds.

3.1.2 ***Synthesis of thin films***: The thin films of the La-2125 type superconductors were synthesized, during the course of this work, by using the Pulsed Laser Deposition (PLD) technique at PLD Lab, Tata Institute of Fundamental Research, Mumbai and also at Department of Physics, University of Pune, Pune.

Conceptually and experimentally, PLD is extremely simple, probably the simplest among all thin film deposition techniques. The schematic experimental arrangement of a PLD setup is shown in Figure 3.2.

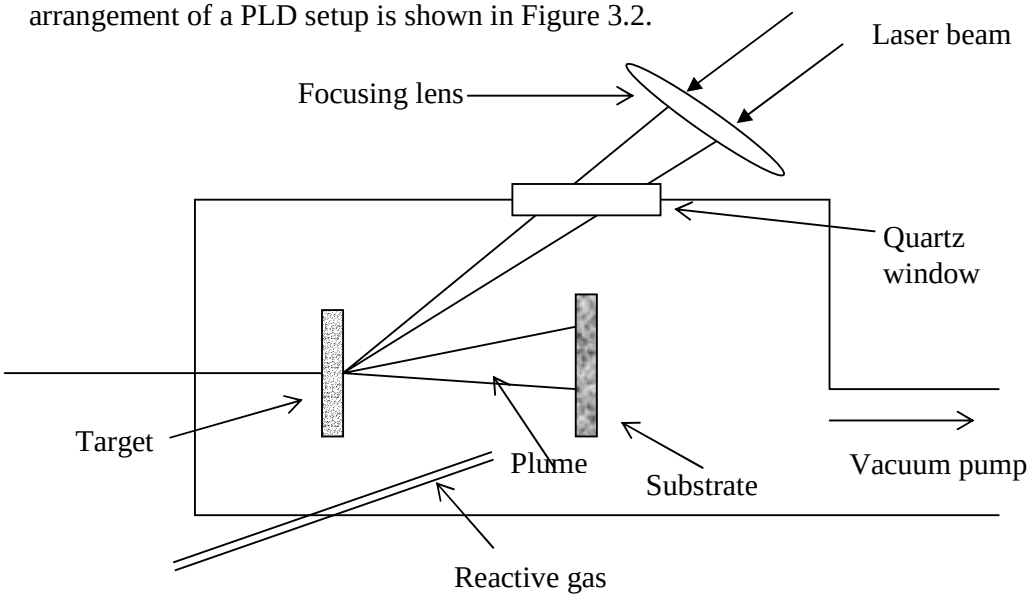

Figure 3.2 Schematic diagram of a pulsed laser deposition apparatus

As shown in the above figure, it consists of a target holder and a substrate holder housed in a vacuum chamber. A high-power laser is used as an external energy source to vaporize materials and to deposit thin films. A set of optical components is used to focus and raster the laser beam over the target surface. The decoupling of the

vacuum hardware and the evaporation power source makes this technique so flexible that it is easily adaptable to different operational modes without constraints imposed by the use of internally powered evaporation sources [1, 2].

The mechanism that leads to material ablation depends on laser characteristics, as well as the object, topological and thermodynamical properties of the target. When the laser radiation is absorbed by a solid surface, electromagnetic energy is converted first into electronic excitation and then into thermal, chemical and even mechanical energy to cause evaporation, ablation, excitation, plasma formation and exfoliation. Evaporants form a "plume" consisting of a mixture of energetic species including atoms, molecules, electrons, ions, clusters, micron-sized solid particulates and molten globules. The collisional mean free path inside the dense plume is very short. As a result, immediately after the laser irradiation, the plume rapidly expands into the vacuum from the target surface to form a nozzle jet (as shown in Figure 3.2), with hydrodynamic flow characteristics. This process attributes to many advantages as well as disadvantages. The advantages are flexibility, fast response, energetic evaporants and congruent evaporation. The disadvantages are the presence of micron-sized particulates and the narrow forward angular distribution that makes large-area scale-up a very difficult task [3, 4].

PLD is so versatile that with the choice of an appropriate laser, it can be used to grow thin films of any kind of material. According to the basic relationship in electromagnetism

$$E = (2\phi/c\varepsilon_0 n)^{1/2}$$

where E = electric field of electromagnetic wave in V/cm

ϕ = power density in W/cm^2

ε_0 = dielectric constant in vacuum = 8.854 * 10^{-12} F/m

c = velocity of light

Consider a material with n = 1.5 and a peak radiation power coupled into the material to be 5 X 10^8 W/cm^2. The corresponding electric field inside the materials will be 5 X 10^5 V/cm, sufficiently high to cause dielectric breakdown. Thus, any material, that absorbs laser radiation of this power level, will be transformed to form plasma. In other words, PLD can be used to vaporize and to deposit thin films of any material if the absorbed laser power density is high enough [5, 6].

The use of short laser pulses offers other advantages, such as congruent evaporation. The criterion for this condition requires the heated volume, characterized by the thermal diffusion length during the laser-target interaction

$$L = 2\,(D.\tau)^{½},$$

where D is the thermal diffusivity and τ is the laser-target interaction time (i.e., pulse duration), to be smaller or equal to the thickness of the ablated layer per pulse. Therefore, the use of short laser pulses for ablation is more likely to achieve congruent ablation that allows PLD to preserve stoichiometry during mass transfer from the target to the thin film. Because of the lack of active electrical elements, such as filaments and discharge electrodes, any kind of reactive gas could be used. Another advantage of undertaking PLD in a reactive environment is the enhanced gas phase reactivity due to the hyperthermal kinetic energy (1 – 20 eV) and the electronic excitation energy of the laser-ablated species.

LASER used in the present work: Generally, for the purpose of thin film deposition, the useful laser wavelength used for PLD lies in the range of 200 nm – 400 nm. Most materials used for deposition work exhibits strong absorption in this spectral region. Absorption coefficients tend to increase as one move to the short wavelength end of this range and the penetration depths into the target materials are correspondingly reduced. This is a favorable situation because thinner layers of the target surface are ablated as one move closer to the 200 nm mark. Most of the thin film work has been centered on the use of excimer lasers and Nd^{3+}: YAG lasers as the deposition sources. The Nd^{3+}: YAG lasers are solid-state systems in which the Neodymium (Nd) ions serve as the active medium and are present as impurities in the YAG (Yttrium Aluminium Garnet) host. It has a fundamental laser wavelength at 1064 nm. Using a nonlinear crystal, the 1064 nm output can be frequency doubled with about 50% power conversion efficiency yielding an output at 532 nm. In order to produce light in the UV, the 532 nm output is mixed with the residual 1064 nm light or frequency doubled again. The resulting outputs at 355 nm or 266 nm are produced with the respective efficiencies of ~ 20 % and ~ 15 % relative to the fundamental.

The excimer is a gas laser system. Unlike Nd^{3+}: YAG lasers, excimer lasers emit their radiation directly in the UV. High outputs delivering in excess of 1 J/pulse are commercially available. These systems can also achieve pulse repetition rates up to several hundred hertz with energies near 500 mJ/pulse. Consequently, the excimer is generally the widely used laser system for PLD work. The Table 3.1 gives a list of excimer wavelengths that are available in the commercial laser systems.

Of all the excimer lasers shown above, KrF and XeCl have been extensively used for PLD, with KrF being the highest gain system for electrically charged pumped

exicmer lasers and is the popular choice among the PLD community. With these benefits on hand, the present work has been carried out using the KrF excimer laser system at both Tata Institute of Fundamental Research and University of Pune.

Table 3.1 Excimer Laser operating wavelengths

Excimer laser system	Wavelength (nm)
F_2	157
ArF	193
KrCl	222
KrF	248
XeCl	308
XeF	351

Basics of Excimer laser: The light output from an excimer laser is derived from a molecular gain medium in which the lasing action takes place between a bound upper electronic state and a repulsive or weakly bound ground electronic state. Because the ground state is repulsive, the excimer molecule can be dissociated rapidly (on the order of a vibrational period ~ 10^{-13} s) as it emits a photon during transition from upper state to ground state. The high ratio of upper state lifetime to lower state lifetime makes the excimer the perfect laser medium because population inversion and therefore high gain are so easily achieved [7].

Some of the factors, which affect the quality of the thin films and their superconducting properties, are

(a) The quality of the bulk target,

(b) Deposition conditions, viz. target to substrate distance, lens distance, laser density, oxygen partial pressure, substrate temperature etc., and

(c) The type of substrate being used

It is observed that high density and highly homogeneous targets yield the best films. However, even the best targets must be resurfaced (sanded flat) at regular intervals in order to perform optimally. In order to maintain uniform target erosion and consumption, the target is rotated during deposition.

As with most thin film deposition techniques, the manner in which the substrate is held and its location and orientation relative to the target are important parameters in a PLD system. Frequently, the substrate must be heated to produce good adhesion and/or epitaxy. For many of the materials commonly deposited by PLD, substrate temperatures in excess of 800 ^{0}C must be maintained with uniformities better than ± 0.5%. The formation of epitaxial complex metal oxide films of high temperature superconductor like Y-123 or La-2125 requires oxygen ambients and high temperatures.

Since the evaporants are ejected as a highly forward-directed plume of material along the target normal, the substrate must be held directly opposite the target. The optimal target – to – substrate distance, D_{ts}, depends on several factors, most significant of which is the energy delivered to the target. Higher beam energies permit larger D_{ts} s to be used. Also, the deposition rate can be controlled by treating D_{ts} as a variable.

During the deposition of thin films of $La_{1.5}Dy_{0.5}Ca_1Ba_2Cu_5O_z$ (La-Dy-2125) bulk target, several of the above parameters were varied in order to achieve optimum deposition parameters. The optimum parameters give thin films with repetition of the

properties. The most critical parameters for the thin film deposition for La-Dy-2125 films have been the oxygen partial pressure, which was kept between 150 mTorr – 500 mTorr. The target to substrate distance, D_{ts}, was also varied from 40 mm to 51 mm. Another important parameter for the deposition is the substrate temperature. The substrate temperature was also raised from 700^0C to 825^0C in order to attain uniform epitaxial thin films. The ablation was done at different laser energies. The range was between 1.316 J/cm^2 – 2 J/cm^2.

3.2 STRUCTURAL PROPERTIES

3.2.1 ***X-ray Diffraction***: Until 1912, mineralogists and crystallographers accumulated most of the knowledge about the crystals over the years, by the measurement of interfacial angles, chemical analysis, and determination of physical properties. There was little knowledge of interior structure, it was indicated that the X-rays might be electromagnetic waves about 1-2 Å in wavelength. In addition, the phenomenon of diffraction was well understood, and it was known that diffraction occurred whenever wave motion encountered a set of regularly spaced scattering objects, provided that the wavelength of the wave motion was of the same order of magnitude as the repeat distance between the scattering centers. The German physicist von Laue was the first person to carryout diffraction experiment using X-rays in 1912. The two English physicists W. H. Bragg and W. L. Bragg analyzed the Laue experiment and were able to express the necessary conditions for diffraction in a mathematical form. They also solved the crystal structures of NaCl, KCl, KBr and KI, all of which have the NaCl structure, and were the first complete crystal-structure determined using the X-ray diffraction as a characterization tool [8].

Diffraction takes place whenever the Bragg law,

$$\lambda = 2d\,Sin\theta$$

is satisfied. This equation puts very stringent conditions on 'λ' and 'θ' for any given crystal. In order to satisfy the Bragg law either λ or θ can be varied, and this is done in different diffraction methods as

	λ	θ
Laue method	Variable	Fixed
Rotating-crystal method	Fixed	Variable (in part)
Powder method	Fixed	Variable

The positions of the atoms in the unit cell affect the intensities but not the directions of the diffracted beams. The intensity of a diffracted beam is changed by any change in atomic positions, conversely the atomic positions can be determined by the observations of diffracted intensities. It is interesting to understand the complex problem of relation between the atomic position and diffracted intensity.

The XRD patterns of all the samples studied during the course of present work were recorded at TIFR (Mumbai) using JEOL and SIETRONICS X-ray diffractometers using Cu-K_α radiation of wavelength 1.5418 Å, in the 2θ range of $20^0 – 80^0$. All the samples were in polycrystalline powder form.

3.2.2 ***Neutron Diffraction***: The main source of obtaining the neutron beam is the nuclear reactor. The neutron diffraction work in the present work has been carried out at the Powder diffractometer (TT-1015) of 'Dhruva Reactor' at BARC, India using neutron beam of wavelength 1.094 Å.

In principle the diffraction from X-rays and neutrons are same, except for some differences such as wavelength, the penetration powers, the scattering factors of atoms for neutrons and X-rays. The information obtained from X-ray diffraction and neutron diffraction varies a little due to these differences. The analysis of neutron diffraction data can be taken as complimentary to the one obtained from X-ray diffraction.

The neutrons in a beam has kinetic energies extending over a considerable range, but a 'monochromatic' beam, i.e., a beam composed of neutrons with a single energy, can be obtained by diffraction from a single crystal and this diffracted beam can be used in diffraction experiments [9]. If E is the kinetic energy of the neutrons, then

$$E = \tfrac{1}{2} mv^2$$

which can be written as;

$$E = P^2/2m$$

where, m = mass of the neutrons (1.68×10^{-27} kg), v = velocity of the neutron, P = momentum of the neutrons. The wavelength of these neutrons can be calculated as;

$$\lambda = h/P$$

or

$$\lambda = h / \sqrt{(2mE)}$$

The neutrons issuing from a reactor have their kinetic energies distributed in much the same way as those of gas molecules in thermal equilibrium; i.e., they follow the Maxwell distribution law. The largest fraction of these so-called "thermal

neutrons" therefore has the kinetic energy equal to kT, where k is Boltzmann's constant and T the absolute temperature. If this fraction is selected by the monochromatic crystal, then $E = kT$ can be taken, and thus,

$$\lambda = h / \sqrt{(2mkT)}$$

T is of the order of 300 ^{0} to 400 ^{0}K, which means that λ is about 1 or 2 Å. Thus, the monochromatic neutrons are taken out of the reactor, and used for diffraction on samples (polycrystalline samples, in the present case). The samples were taken in the form of powders, filled in Vanadium can with aluminium cap. Vanadium being transparent to neutrons, will not contribute to the diffracted patterns. The arrangement of the sample is made in such a way that only the Vanadium can is exposed to the impinging neutron beam and the diffracted neutron beam is recorded by the position sensitive detector (PSD). The schematic representation of the typical neutron diffraction experiment setup is shown in the Figures 3.3 (a) and (b). The planes in the 'polycrystalline sample' act as grating to the neutron beams, and diffract them. The diffracted neutrons are collected by the PSD, which is filled with helium gas. For every neutron falling on the PSD, the following reaction takes place, and eventually, the intensity is observed.

$$^1n_0 + {}^3He_2 \rightarrow {}^3T_1 + {}^1p_1$$

One incoming neutron interacts with the molecule of Helium gas, and breaks it into one tritium and one proton. Protons are charged particles, which ionizes the helium gas thus producing ions. These ions are recorded, as pulses by the "cathode – anode setup" kept under high potential. The whole cathode length is distributed or sliced into 1024 channels in the Dhruva reactor setup. The counts (pulses i.e., the

number of ions falling on the cathode) at each channel are recorded. The multi-channel analyzer (MCA) records the data from each channel and using a discriminator separates out the neutron pulses from the background pulses (which occur due to gamma ray etc,). The data from MCA is fed into the computer from where the intensity vs. channel spectrum can be analyzed and recorded. Using appropriate calibration constants, the channels are converted into corresponding angles.

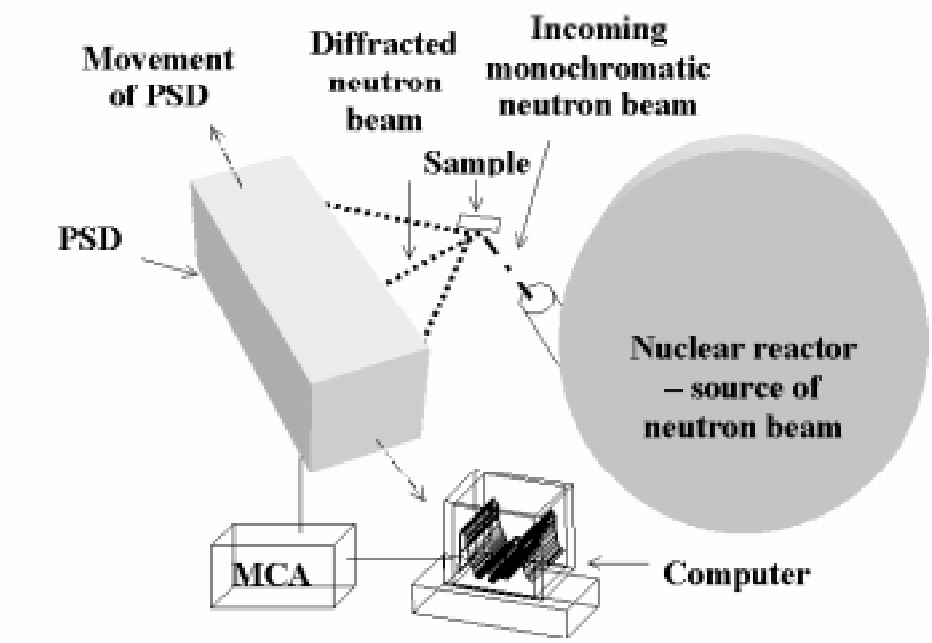

Figure 3.3 (a) Experimental Neutron diffraction experiment setup

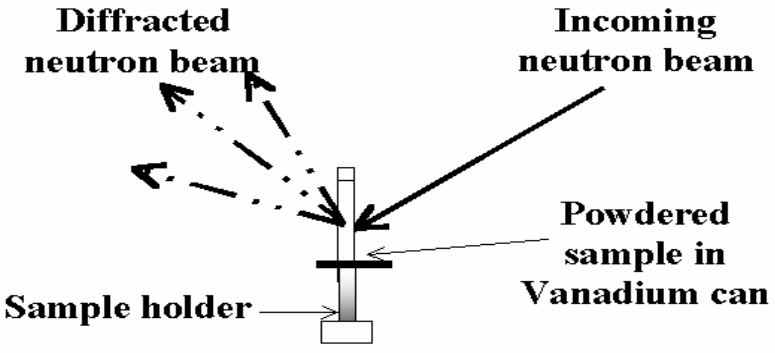

Figure 3.3 (b) Arrangement of sample at the detector angle in front of the PSD

Figure 3.4 shows the difference in the scattering amplitudes of X-rays and neutrons for different atoms [10].

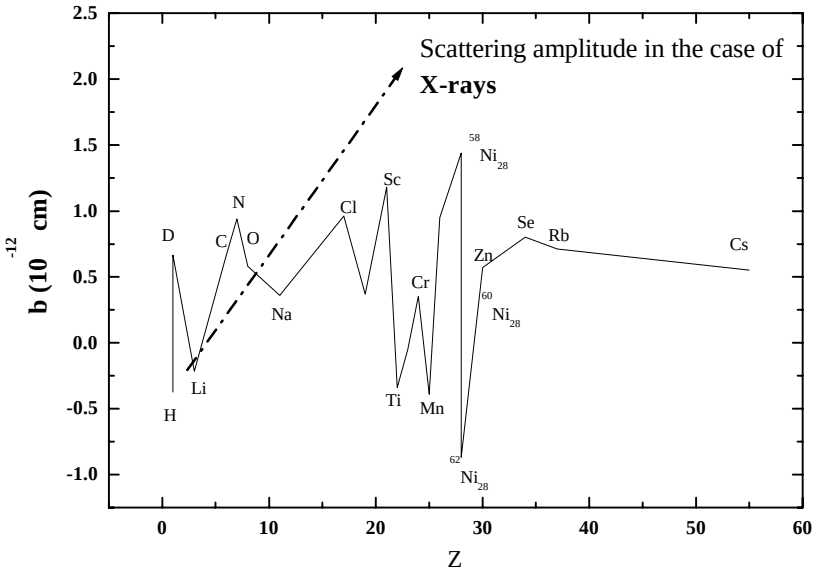

Figure 3.4 ***The irregular variation of neutron scattering amplitude (b) with atomic number Z for some selected elements. For comparison the regular increase for X-ray is shown***

The main differences between the X-rays and neutrons, in terms of their usage for the purpose of diffraction for structural studies, can be summarized as:

(a) A neutron beam is highly penetrating. An iron plate, 1 cm thick, is opaque to electrons, virtually opaque to 1.5 Å X-rays, but transmits 35% of 1.5 Å neutrons.

(b) The intensity of neutron scattering varies quite irregularly with the atomic number Z of the scattering atom. Elements with almost the same values of Z may have quite different neutron-scattering powers, and elements with widely separated values of Z may scatter neutrons equally well. Furthermore, some

light elements, such as carbon, scatter neutron more intensely than some heavy elements, such as tungsten. Hence, it can be stated that structure analyses can be carried out with neutron diffraction that are impossible, or possible only with great difficulty, with X-ray or electron diffraction. Neutrons can also distinguish in many cases between elements differing by only one atomic number, elements which scatter X-rays with almost equal intensity.

(c) Neutrons have a small magnetic moment. If the scattering atom also has a net magnetic moment, the two interact and modify the total scattering. In substances that have an ordered arrangement of atomic moments (antiferromagnetic, ferromagnetic, and ferromagnetic) neutron diffraction can disclose both the magnitude and direction of the moments. Only neutron diffraction can furnish such information, and it has had a major impact on studies of magnetic structure.

(d) Diffuse scattering (in transmission), also occurs with neutrons. Neutron small-angle scattering has certain advantages over X-rays as a means of studying inhomogeneities in materials, particularly because thick specimens, rather than thin foils can be examined.

Structural analysis of the X-ray and Neutron diffraction data: The investigation into the structure of an unknown compound involves many stages. First one is the data acquisition and secondly the analysis of this data to retrieve the relevant information, and finally the proper interpretation of the analyzed data. The powder diffraction of the high temperature La-2125 type mixed oxide superconductors has been carried out by X-rays and neutrons, in order to ascertain the structure of these types of oxides.

Figure 3.5 shows the general approach to the structural analysis using XRD data, which has been employed in the present work.

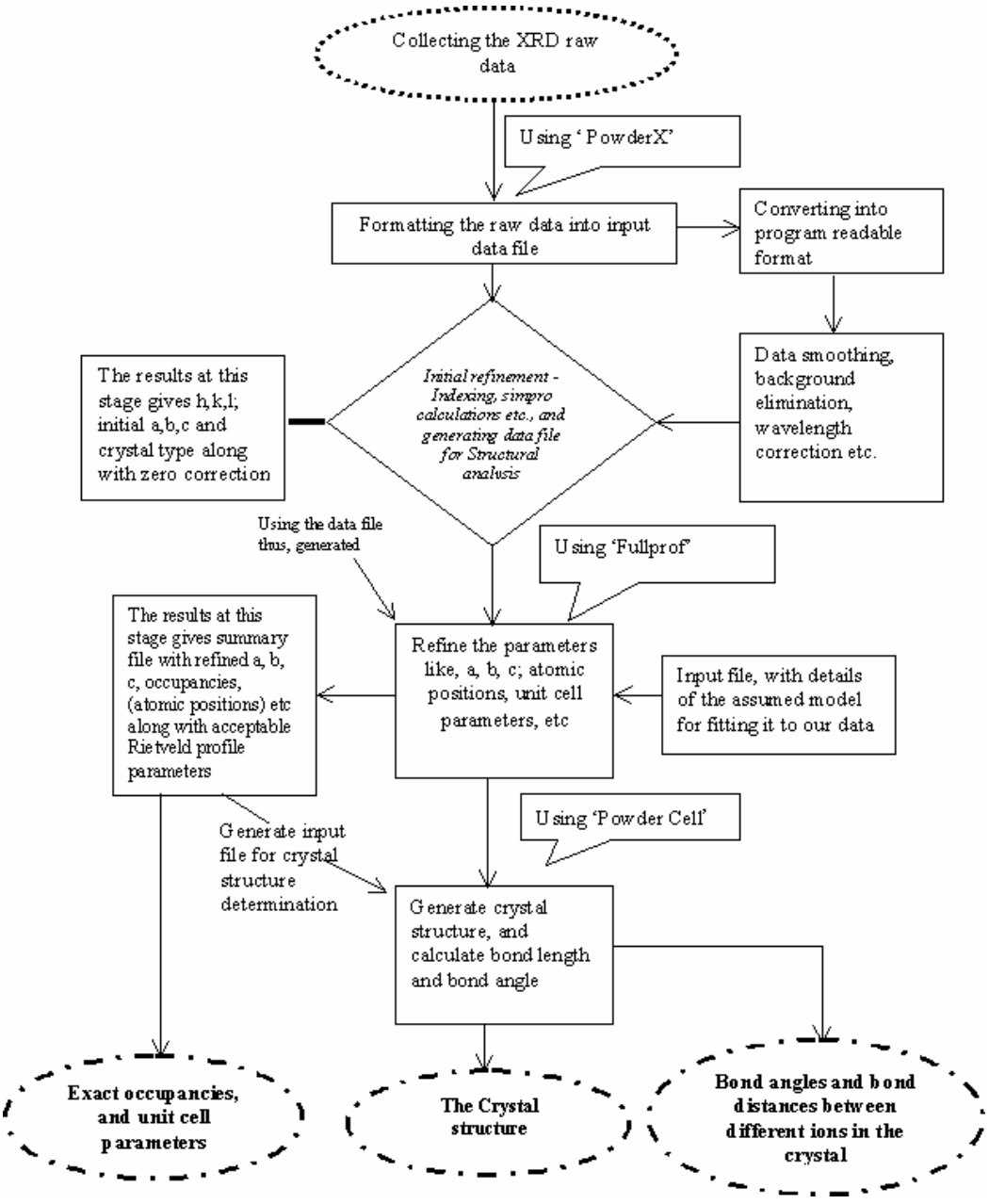

Figure 3.5 Block-diagram for the analysis of XRD data

The X-ray data has been recorded on the Sietronics and JEOL (Left Goniometer) X-ray diffractometers at TIFR, Mumbai using a Cu-K_α radiation of

1.5418 Å. The analysis of the X-ray data has been done using various computer softwares. The softwares used prominently in the present work are PowderX [11], FULLPROF [12], and Powder Cell [13]. In the course of present work, these softwares have been used very efficiently to obtain exact unit cell parameters and site occupancies of all the polycrystalline samples studied.

'**PowderX**' – the features of Powder X can be summarized as:

1. PowderX can read 13 data formats, either from angular-dispersive or energy-dispersive X-ray diffraction, used by various diffractometers made by Mac Science, Philips, Siemens, Rigaku, etc. It can also write many data formats used for ab initio structural solution and Rietveld refinements (EXPO, DBWS, GSAS, FULLPROF, RIETAN, etc.)
2. Display both the previous data and the data after processing so that it is very easy to see the effects of the processes during smoothing, background subtraction and α2 elimination.
3. Simple method for parameters input and easy to use interfaces.
4. Various methods for data smoothing, α2 elimination and peak search are available, so that the user can find the optimum methods for their data set. The high-angle side fluctuations is less than 0.5% of the peak intensity using our methods for Cu-$K_{\alpha 2}$ elimination, which is much better than conventional Rachinger and Ladell methods.
5. Derivatives and Fourier transforms of the X-ray data can be calculated, plotted and saved as data files.
6. Zero shift and other geometrical aberrations can be easily calculated and corrected.

7. Any part of the plot can be zoomed with mouse to see the details.
8. Print the ready-to-publish plots of X-ray diffraction data.
9. Edit the control file using graphical interfaces for pattern fitting program Simpro.
10. Several other programs, D_{hkl} (Calculate the diffraction angles and crystal plane spaces from the lattice parameters), Lazy (generating the simulated powder x-ray diffraction patterns), Treor90 (Index) and Eracel have been included in this system with user-friendly interfaces.

'**FULLPROF**' – is the Rietveld refinement program, which can be used for the Rietveld refinement of both X-ray and neutron diffraction data. Mainly used for Rietveld analysis (structure profile refinement) of neutron (CW, TOF, nuclear and magnetic scattering) or X-ray powder diffraction data collected as a function of the scattering variable T (2theta or TOF). The program can be also used as a Profile Matching tool, without the knowledge of the structure. Single crystal refinements can also be performed alone or in combination with powder data. The program FullProf is based on the code of the Young & Wiles (DBW) program on the code DBW3.2S (Versions 8711 and 8804). The features of FullProf can be highlighted as

1. Choice of line shape (Gaussian, Lorentzian, modified Lorentzians, pseudo-Voigt, Pearson-VII or Thompson-Cox-Hastings) for each phase.
2. Neutron (constant wavelength and TOF) and X-ray (laboratory and synchrotron sources)
3. One or two wavelengths ($K_{\alpha 1} + K_{\alpha 2}$)
4. Background refinement
5. Multi-phase (up to 8 phases)

6. Preferred orientation: two functions available
7. Absorption correction for a cylinder, microabsoprtion for flat samples.
8. Choice between three wheighting schemes: standard least squares, maximum likelihood and unit wheights.
9. Choice between automatic generation of hkl and/or symmetry operators and file given by user.
10. Magnetic structure refinement (crystallographic and spherical representation of the magnetic moments). Two methods: describing the magnetic structure in the magnetic unit cell of making use of the propagation vectors using the crystallographic cell. This second method is necessary for incommensurate magnetic structures.
11. Automatic generation of reflections for an incommensurate structure with up to 24 propagation vectors. Refinement of propagation vectors in reciprocal lattice units.
12. h, k, l dependence FWHM for strain and size effects
13. h, k, l dependence of shift and asymmetry for special kind of defects
14. Profile Matching. The full profile can be fitted without prior knowledge of the structure (needs only good starting cell and profile parameters)
15. Quantitative analysis without need of structure factor calculations.
16. Chemical (distances) and magnetic (magnetic moments) slack constraints
17. Resolution function (for pseudo-Voigt peak shape) may be supplied in a file
18. Structural or magnetic model could be supplied by an external subroutine for special purposes (rigid body, TLS, polymers, form factor refinements, small

angle scattering of amphifilic crystals, description of incommensurate structures in real direct space, etc.)

19. Single crystal data or integrated intensities can be used as observations (alone or in combination with a powder profile)
20. Neutron (or X-rays) powder patterns can be mixed with integrated intensities of X-rays (or neutron) from single crystal or powder data.

The requirement for using the FULLPROF program is an input file, with the description (in proper format) of assumed structure such as space group, atomic positions, occupancy, unit cell parameters etc. The program generates a profile of the assumed structure (or say model) using the description we have provided. This pattern is refined to fit with the observed data. By varying the profile generating parameters in the assumed model, a perfect fit with reliable Rietveld profile parameters, is obtained. The program has ability to carryout multi-phase refinement and also to carryout magnetic structure refinement, in the case of neutron diffraction data of magnetic samples.

"**Powder Cell**" - The basic idea of the program is the specific use of crystallographic know-how for an intuitive generation of structure models. Very often the success of the so-called Rietveld programs — e.g. DBWS, LHPM8, EDINP/ALLHKL, GSAS, PREP/PROF (RIETVELD), FULLPROF, or RIETAN — depends on the initial structure model. Exactly this characterizes the aim of the program. The user shall be able to manipulate in an easy way known crystal structures (translation and rotation of atoms or molecules; change, delete and insert atoms or molecules, symmetry reduction etc.) or to create a new in a relative short time only by the use of

crystallographic and crystal chemical knowledge. On this way Powder Cell tries to support the structure determination.

The criterion for the quality of the created or modified model is the calculated powder pattern. That means that one of the most important requirements is an excellent X-ray or neutron measurement on a powder of the interesting substance. On one hand, the deviation in the experimental and theoretical diffractograms may be due to unacceptable adaptation of the model on the real structure. On the other hand it is very possible that the measurements include texture components. However, the comparison with a theoretical diffractogram requires its exact calculation. Therefore the simulation must allow the variation of essential experimental parameters, e.g. used radiation, consideration of anomalous dispersion, diffraction geometry, fixed or variable slits, different intensity corrections, consideration of doublet, background etc. However, not only in research it is useful, but also for the solution of problems connecting with phase identification, phase mixtures, unknown preferred orientations, the simulation of a powder pattern of a phase described exclusively by single crystal data, one can apply the different features of Powder Cell.

☞ ***The Rietveld Refinement method***: The principal goal of this method is to refine crystal structures and not profiles, hence it is called Rietveld method instead of 'profile refinement' or 'whole pattern fitting structure refinement'. The things actually being refined are parameters in models for the structure and for other specimen and instrument effects on the diffraction pattern. It is called "Rietveld method", named after Dr. H. M. Rietveld [14, 15], because of his work and open-handed sharing of all aspects. He was the first person

- who first worked out computer-based analytical procedures to make use of the full information content of the powder pattern
- who put them in public domain by publication of two seminal papers
- who shared freely and widely his computer program.

In the Rietveld method, the least-squares refinements are carried out until the best fit is obtained between the entire observed powder diffraction pattern taken as a whole and the entire calculated pattern based on the simultaneously refined models for the crystal structure, diffraction optic effects, instrumental factors, and other specimen characteristics (e.g., lattice parameters) as may be desired and can be modeled [16].

For a Rietveld refinement, it is essential that the powder diffraction data be collected properly. The data is recorded in digitized form i.e., as a numerical intensity value, y_2, at each of several thousand equal increments (steps), i, in the pattern. Depending on the method, the increments can be scattering angle, 2θ or wavelength (X-ray data collected with an energy dispersive detector and an incident beam of 'white' radiation X-radiation). For constant wavelength data, the increments are usually steps in scattering angle and the intensity y_i at each step i, in the pattern is measured directly with a quantum detector on a diffractometer. Factors affecting the data collection and which have to be considered before the collection are the geometry of the diffractometer, the quality of the instrument alignment and calibration, the most suitable radiation (e.g. conventional X-ray, synchrotron X-ray or neutron), the wavelength, appropriate sample preparation and thickness, slit sizes and necessary counting time.

Typical step sizes range from 0.01 to 0.05 in 2θ for a fixed wavelength X-ray data and a bit larger for fixed wavelength neutron data. To ensure good counting statistics throughout an X-ray powder diffraction pattern, more time should be spent on data collection at high angles where the intensities are lower. An appropriate data-collection strategy depends on the nature of the sample (e.g., how well it scatters, how quickly the pattern degrades, peak-broadening effects and the degree of peak overlap). Ideally the step size = FWHM/5, FWHM = full width at half-maximum, as there are at least five steps across the top of each peak. The time per step should approximately compensate for the gradual decline in intensity with 2θ.

Rietveld refinement with neutron diffraction data has been notably successful both with fixed-wavelength data, with which Rietveld developed and used this method. The Rietveld method is the same no matter what powder diffraction data are used. The differences among data sources affect the data preparation that is required, whether the steps are in angle or energy, and the instrumental parameters that are refined but not in the method itself.

In all cases, the best fit sought is the best least squares fit to all of the thousands of y_i'*s* simultaneously [17]. The quantity minimized in the least-squares refinement is the residual, S_y:

$$S_y = \sum_i w_i \left(y_i - y_{ci} \right)^2$$

where,

$w_i = 1 / y_i$

y_i = observed (gross) intensity at the *i*th step.

y_{ci} = calculated intensity at the *i*th step,

and the sum is overall data points.

A powder diffraction pattern of a crystalline material may be thought of as a collection of individual reflection profiles, each of which has a peak height, a peak position, a breadth, tails which decay gradually with distance from peak positions, and an integrated area which is proportional to the Bragg intensity, I_k, where K stands for the Miller indices, *h, k, l,* I_k is proportional to the square of the absolute value of the structure factor $|F|^2$. It is a crucial feature of the Rietveld method that no effort is made in advance to allocate observed intensity to particular Bragg reflections nor to resolve overlapped reflections. Consequently, a reasonably good starting model is needed. The 'method is a structure refinement method'. Typically, many Bragg reflections contribute to the intensity, y_i, observed at any arbitrarily chosen point, i, in the pattern. The calculated intensities y_{ci}, are determined from the $|F_K|^2$ values calculated from the structural model by summing of the calculated contributions from neighboring (i.e., within a specified range) Bragg reflections plus the background:

$$y_{ci} = s\sum_k L_k \left|F_k\right|^2 \phi(2\theta_i - 2\theta_k) P_k A + y_{bi}$$

where, ***s*** is scale factor, ***K*** is the miller indices, *h, k, l* for Bragg reflection, $\boldsymbol{L_k}$ is the Lorentz, polarization, and multiplicity factors, $\boldsymbol{\Phi}$ is the reflection profile function, $\boldsymbol{P_k}$ is the preferred orientation function, ***A*** is an absorption factor, $\boldsymbol{F_k}$ is the structure factor for the $\boldsymbol{k^{th}}$ Bragg reflection and $\boldsymbol{y_{bi}}$ is the background intensity at the $\boldsymbol{i^{th}}$ step. The structure factor F_k, is given by

$$F_k = \sum_j N_i f_i \ exp\ [2\pi i(hx_j + ky_j + lz_j)]\ exp\ [-M_j]$$

with $M_j = 8\pi^2 u_s^{-2} \sin^2\theta / \lambda^2$, where u_s^{-2} is the root-mean-square thermal (and random static) displacement of the j^{th} atom.

The effective absorption factor, $\boldsymbol{A}$, differs with instrument geometry. It is usually taken to be a constant for the instrument geometry used for X-ray diffractometers. The least squares minimization procedures lead to a set of *normal equations* involving derivatives of all of the calculated intensities, $\boldsymbol{y_{ci}}$, with respect to each adjustable parameters and are soluble by inversion of the *normal matrix* with elements $\boldsymbol{M_{jk}}$ formally given by

$$\boldsymbol{M_{jk}} = \sum_i 2w_i \left((y_i - y_{ci}) \frac{\partial^2 y_{ci}}{\partial x_j \partial x_k} - \left(\frac{\partial y_{ci}}{\partial x_j} \right) \left(\frac{\partial y_{ci}}{\partial x_k} \right) \right)$$

where the parameters x_j, x_k are the (same set of) adjustable parameters. In the use of this algorithm, it is common practice to approximate these matrix elements by deletion of the first term, that in $(y_i - y_{ci})$. Thus, we are dealing with the creation and inversion of an m *X* m matrix, where m is the number of parameters being refined. Because the residual function is non-linear, the solution must be found with an iterative procedure in which the shifts, Δx_k are

$$\Delta x_k = \sum M^{-1}_{jk} \frac{\partial s_y}{\partial x_k}$$

The calculated shifts are applied to the initial parameters to produce, a supposedly, improved model and the whole procedure is then repeated. Because the relationships between the adjustable parameters and the intensities are non-linear, the starting model must be close to the correct model or the non-linear least squares procedure will not lead to the global minimum.

The model parameters that may be refined include not only atom positional, thermal, and site-occupancy parameters but also parameters for the background, lattice, instrumental geometrical optical features, specimen aberrations (e.g., specimen displacement and transparency), an amorphous component and specimen reflection-profile-broadening agents such as crystallite size and microstrain. Multiple phases may be refined simultaneously and comparative analysis of the separate overall scale factors for the phases offers what is probably the most reliable current method for doing quantitative phase analysis. The usual refinable parameters are listed in table 3.2.

Table 3.2 Parameters refinable simultaneously during Rietveld refinement

Parameters to be refined for each phase present	**Global Parameters**
x_j yj z_j B_j N_j; x_j y_j z_j are position coordinates, B_j is an isotropic thermal parameters, and N_j is the site-occupancy multiplier, all for the j^{th} atom in the unit cell	2θ – Zero shift
Scale factor	Instrumental profile
Specimen-profile breadth parameters	Profile asymmetry
Lattice parameters	Background
Overall temperature factor (thermal parameters)	Wavelength
Individual anisotropic thermal parameters	Specimen displacement

Preferred orientation	Specimen transparency
Crystallite size and microstrain	Absorption
Extinction	

There are usually two approaches to dealing with the background in a powder diffraction pattern. It can both be estimated by linear interpolation between selected points between peaks and then subtracted, or it can be modeled by an empirical or semi-empirical function containing several refinable parameters. For refining the background, y_{bi}, must be obtained from a refinable background function, which may be phenomenological or, better, based on physical reality and include refinable models. One such phenomenological fifth-order polynomial provided with an operator-specific origin is

$$y_{bi} = \sum_{m=0}^{5} B_m \, (2\theta_i / BKPOS) - 1]^m$$

where *BKPOS* is the origin that is to be specified in the input control file.

With a complete structural model and good starting values for the background contribution, the unit-cell parameters and the profile parameters, the Rietveld refinement of structural parameters can begin. Because the global minimum of the least-squares residual function is much shallower with powder data than it is with single-crystal data, and false minima are more prevalent, the refinement needs constant monitoring. A refinement of a structure of medium complexity can require a hundred cycles, while a structure of high complexity may easily require several hundred. The profile fit is best seen in a plot but can also be followed numerically with a reliability factor or R factor. The difference plots indicate whether a high R-value is due to a profile-parameter problem (i.e., total intensity is approximately

correct but there are differences in the peak form) or to a deficiency in the structural model (i.e., integrated intensities does not match). An approximate strategy for refinement can be described as,

Changes in positional parameters cause changes in structure-factor magnitudes and therefore in relative peak intensities, whereas atomic displacement (thermal) parameters have the effect of emphasizing the high-angle region (smaller thermal parameters) or de-emphasizing it (larger thermal parameters).

The scale, the occupancy parameters and the thermal parameters are highly correlated with one another, and are more sensitive to the background correction than are the positional parameters.

The structure should be refined to convergence. That is, the maximum shift / estimated standard deviation (e.s.d) in the final cycle of refinement should be no more than 0.10. All parameters (profile and structural) should be refined simultaneously to obtain correct e.s.d.

R-values: Although a difference profile plot is probably the best way of following and guiding a Rietveld refinement, the fit of the calculated pattern to the observed data can also be given numerically. This is usually done in terms of agreement indices or R-values.

The weighted-profile R-value, R_{wp}, is defined as:

$$R_{wp} = \left\{ \sum_{i}^{N} w_i [y_i(obs) - y_i(calc)]^2 / \sum_{i}^{N} w_i [y_i(obs)]^2 \right\}^{½}$$

where $y_i\ (obs)$ is the observed intensity at step, i, $y_i\ (calc)$ the calculated intensity, and w_i the weight. From a purely mathematical point of view, R_{wp}, is the most meaningful of these R s because the numerator is the residual being minimized. For the same

reason, it is also the one that best reflects the progress of the refinement. Ideally, the final R_{wp} should approach the statistically expected R-value, R_{exp},

$$R_{exp} = \left((N\text{-}P) / \sum_{i}^{N} w_i y_i(obs)^2 \right)^{½}$$

where N is the number of observations and P the number of parameters. R_{exp} reflects the quality of the data (i.e., the counting statistics). Thus, the ratio between the two is another useful numerical criterion, called the 'goodness of fit'. It is generally given as, χ^2 and expressed as:

$$\chi^2 = R_{wp} / R_{exp}$$

If the data have been 'over-collected' R_{exp} will be very small and χ^2 for a fully refined structure much larger than 1. Conversely, if the data have been 'under-collected', R_{exp} will be large and χ^2 could be less than 1.

An R-value similar to that reported for single-crystal refinements, based on the agreement between the observed and calculated structure factors, F_{hkl}, can also be calculated by distributing the intensities of the overlapping reflections according to the structural model,

$$R_F = \sum_{hkl} |F_{hkl}(obs) - F_{hkl}(calc)| / \sum_{hkl} |F_{hkl}(obs)|$$

Similarly, the Bragg-intensity R-value,

$$R_B = \sum_{hkl} |I_{hkl}(obs) - I_{hkl}(calc)| / \sum_{hkl} |I_{hkl}(obs)|$$

Where $I_{hkl} = mF^2_{hkl}$ (m = multiplicity), or its weighted equivalent can be used to monitor the improvement in the structural model. Because 'R-Bragg (R_B)' and 'R-structure factor (R_F)' are based not on actually observed Bragg intensities but on those deduced with the help of the model, they are, therefore, biased in favor of the

model being used. None the less, they are the R's that are most nearly comparable to the conventional R-values quoted in the literature on single crystal structure refinements. They also serve a useful function because they are insensitive to misfits in the pattern that do not involve the Bragg intensities of the phase(s) being modelled.

R-values are useful indicators for the evaluation of a refinement, especially in the case of small improvements to the model, but they should not be over interpreted. The most important criteria for judging the quality of a Rietveld refinement are

The fit of the calculated pattern to the observed data and the chemical sense of the structure model.

The former can be evaluated on the basis of the final profile plot (using the complete range of data collected) and the latter on a careful examination of the final atomic positions.

One of the great triumphs of Rietveld analysis has been in its crucial contributions to the development of the field of high temperature superconductors. Diffractionists at the best neutron diffraction facilities, in 1987 - soon after the discovery of first really high temperature superconductor, T_c = 90 K, and Brookhaven National Laboratory, in the US; pulsed neutron (TOF) sources at the Rutherford-Appleton Laboratory in the UK and many other groups around the world, studied larger samples of the polycrystalline matrix, performed Rietveld analysis with several different starting models, and all came to the same conclusion in detail. The structure was, thus correctly determined from powder diffraction data whereas the X-ray single crystal results had been in error.

In the present work, the starting model of tetragonal Y-123 with space group P 4/M M M was assumed. Since it was expected that the La-2125 is a stochiometric

derivative of the La-123 compound. Hence, the fitting was carried out on the lines of tetragonal La-123 compound. The patterns matched very well, giving reliable R-values. Using the results of Rietveld analysis of all the samples, bond lengths and bond angles were calculated. And based on them, a structure for La-2125 unit cell has been simulated.

3.2.3 ***Atomic Force Microscopy (AFM)***: The atomic force microscope (AFM) probes the surface of a sample with a sharp tip, a couple of microns long and often less than 100 Å in diameter [18]. The tip is located at the free end of a cantilever that is 100 to 200 μm long. Forces between the tip and the sample surface cause the cantilever to bend, or deflect. A detector measures the cantilever deflection as the tip is scanned over the sample, or the sample is scanned under the tip. The measured cantilever deflections allow a computer to generate a map or surface topography [19].

Several forces typically contribute to the deflection of an AFM cantilever. AFM operates by measuring the attractive or repulsive forces between a tip and the sample. The forces most commonly associated with atomic force microscopy are interatomic force called the van der Waals force. The dependence of the van der Waals force upon the distance between the tip and the sample is shown in the Figure 3.6. The two distance regimes are labeled in the figure are (a) the contact regime; and (b) the non-contact regime.

In the contact regime, the cantilever is held less than a few angstroms from the sample surface, and the interatomic force between the cantilever and the sample is repulsive. In the non-contact regime, the cantilever is held on the order of tens to hundreds of angstroms from the sample surface, and the interatomic force between the

cantilever and sample is attractive (largely a result of the long-range van der Waals interactions).

In principle, AFM resembles the record player as well as the stylus profilometer. However, AFM incorporates a number of refinements that enable it to achieve atomic-scale resolution:

- Sensitive detection
- Flexible cantilevers
- Sharp tips
- High-resolution tip-sample positioning, and
- Force feedback

In the present work, the work was carried out by using the contact mode of AFM. In contact AFM mode, also known as repulsive mode, an AFM tip makes soft 'physical contact' with the sample. The tip is attached to the end of a cantilever with a low spring constant, lower than the effective spring constant holding the atoms of the sample together. As the scanner gently traces the tip across the sample (or the sample under the tip), the contact force causes the cantilever to bend to accommodate changes in topography. Considering the Figure 3.6, we can see that at the right side of the curve a large distance separates the atoms. As the atoms are gradually brought together, they first weakly attract each other. This attraction increases until the atoms are so close together that their electron clouds begin to repel each other electrostatically. This electrostatic repulsion progressively weakens the attractive forces as the interatomic separation continues to decrease. The force goes to zero when the distance between the atoms reaches a couple of angstroms, about the length

of a chemical bond. When the total van der Waals force becomes positive (repulsive), the atoms are in contact.

The slope of the van der Waals curve is very steep in the repulsive or contact regime. As a result, the repulsive van der Waals force balances almost any force that attempts to push the atoms closer together. In AFM, this means that, when the cantilever pushes the tip against the sample, the cantilever bends rather than forcing the tip atoms closer to the sample atoms.

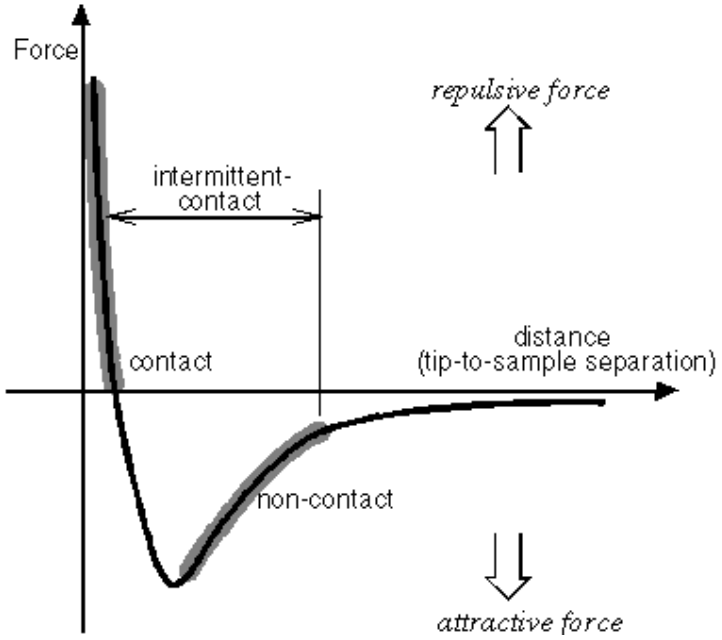

Figure 3.6 Interatomic force versus the distance curve for the operation of AFM

In addition to the repulsive van der Waals force, two other forces are generally present during contact AFM operation: a capillary force exerted by the thin water layer often present in an ambient environment, and the force exerted by the cantilever itself [20]. Most AFMs detect the position of the cantilever with optical techniques [21, 22].

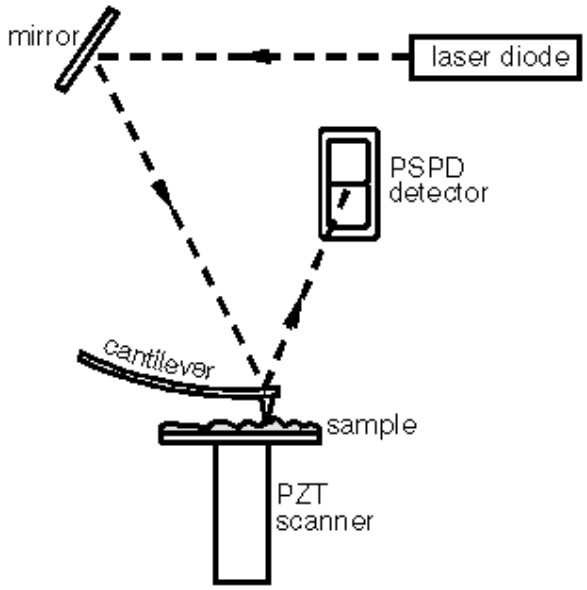

Figure 3.7 The working of a Contact mode AFM

As shown in Figure 3.7, a laser beam bounces off the back of the cantilever onto a position-sensitive photo detector (PSPD). As the cantilever bends, the position of the laser beam on the detector shifts. The PSPD itself can measure displacements of light as small as 10Å. The ratio of the path length between the cantilever and the detector to the length of the cantilever itself produces a mechanical amplification. As a result, the system can detect sub-angstrom vertical movement of the cantilever tip.

Once the AFM has detected the cantilever deflection, it can generate the topographic data set by operating in one of two modes, constant-height or constant-force mode. In constant-height mode, the spatial variation of the cantilever deflection can be used directly to generate the topographic data set because the height of the scanner is fixed as it scans. In constant – force mode, the deflection of the cantilever can be used as input to a feedback circuit that moves the scanner up and down in z – direction, responding to the topography by keeping the cantilever deflection constant. In this case, the image is generated from the scanner's motion. With the cantilever

deflection held constant, the total force applied to the sample is constant. In this method, the speed of scanning is limited by the response time of the feedback circuit, but the total force exerted on the sample by the tip is well controlled.

The present work has been carried out on a Nanoscope III (Digital equipments) AFM at TIFR (Mumbai) working in the contact mode.

3.2.4 ***Scanning Electron Microscopy (SEM)***: The Scanning Electron Microscope (SEM) is a microscope that uses electrons rather than light to form an image. The SEM has a large depth of field, which allows a large amount of the sample to be in focus at one time. The SEM also produces images of high resolution, which means that closely spaced features can be examined at a high magnification [23]. Preparation of the samples is relatively easy since most SEMs only require the sample to be conductive. The combination of higher magnification, larger depth of focus, greater resolution, and ease of sample observation makes the SEM one of the most widely used instruments in materials research.

In the SEM, a beam of electrons is directed from a filament to the sample in a vacuum environment ranging from 10^{-4} to 10^{-10} Torr. The electrons are guided on to the sample by a series of electromagnetic lenses. The resolution and depth of field of the image are determined by the beam current and the final spot size, which are adjusted with one ore more condenser lenses and the final, probe-forming objective lenses. The electrons interact with the sample with a few nanometers to several microns of the surface, depending on beam parameters and sample type. Electrons are emitted from the sample primarily as either backscattered electrons or secondary electrons. Once these electrons escape from the sample surface, an Everhart-Thornley scintillator-photomultiplier detector typically detects them.

Secondary electrons are the most common signal used for investigations of surface morphology. They are produced as a result of interactions between beam electrons and weakly bound electrons in the conduction band of the sample which then escape from the sample surface as secondary electrons. Secondary electrons are low energy electrons (< 50 eV), so only those formed within the first few nanometers of the sample surface have enough energy to escape and be detected. High-energy beam electrons, which are scattered, back out of the sample (backscattered electrons) can also form secondary electrons when they leave the surface. Since these electrons travel faster farther into the sample than the secondary electrons, they can emerge from the sample at a much larger distance away from the impact of the incident beam, which makes their spatial distribution larger. The SEM image formed is the result of the intensity of the secondary electron emission from the sample at each x, y data point during the rastering of electron beam across the surface.

Although SEM and AFM appear very different, they actually share a number of similarities. Both techniques raster a probe across the surface to detect some interaction with the surface to form an image. Both have a lateral resolution, which is similar in scale. By using these two techniques, which are complementary, one technique will often compensate for the imagining artifact of the other technique.

In the present work, the SEM measurements were carried out at TIFR (Mumbai) using a Jeol instrument at magnification range of 5000 - 10000.

3.3 TRANSPORT PROPERTIES

3.3.1 ***Resistivity measurements***: Resistivity studies on the high temperature superconducting samples were carried out using the standard d. c. four probe

technique [24, 25]. These studies help to determine the exact value of the superconducting onset and zero electrical resistance temperature (T_c) of a particular HTSC sample.

Four contacts were made on the well-sintered pellet using conductive silver epoxy paint. Fine enameled copper wires were used to pass the constant current through the outer two leads using a constant current source (KEITHLY current source – Model 220). Current of the order of few hundred microamps to few milliamps is passed, while the voltage developed across the two inner leads is measured using the nanovoltmeter (KEITHLEY model 181) as a function of temperature. DC resistance of the samples is then found by Ohm's law. In this configuration, the lead resistance of the potential leads does not come into the picture because no current flows through these leads under null-balanced condition, thus ensuring that the measured potential is the potential of the sample only. The block diagram of the four-probe setup used for measuring the d.c. resistance is shown in Figure 3.8.

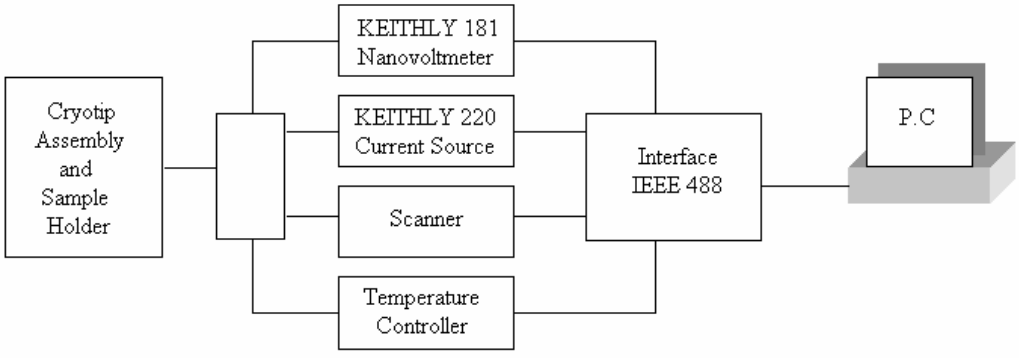

Figure 3.8 Block diagram of d.c. four probe resistivity setup

The characteristic parameters of superconducting transition generally used are defined as:

T_c^{on}	The superconducting onset temperature is the temperature at which the resistance starts decreasing abruptly
$T_c^{R=0}$	The temperature at which resistance goes to zero within the measuring capability of the measuring instrument. Generally, to characterize the zero resistance state a criterion of potential drop of $< 10^{-1}$ μv was used.
T_c^{mid}	The temperature corresponding to the mid point of the superconducting transition, i.e., the average of the temperature corresponding to 90% and 10% of the resistance at T_c^{on}
ΔT_c	Width of the superconducting transition, which measures the temperature interval for the fall of resistance from 90% to 10% of its value of T_c^{on}

3.4 MAGNETIC PROPERTIES

3.4.1 ***a.c.susceptibility***: The a.c. susceptibility measurements were performed using mutual inductance method consisting of primary and secondary coils. The primary coil (wound in same direction) are coaxially wound on secondary coils (two sections connected in series but wound in opposite direction). The primary coil was connected to a lock-in-amplifier (EG & G Model 5210). A low frequency (100 Hz) sine wave signal was generated using a signal generator and was fed to the primary coil as well as the lock-in-amplifier as a reference signal. The alternating current produced an alternating magnetic field inside the primary coil, which induced voltage in secondary

coils. With no sample in the coil, the mutual inductance of the combined coil is zero. The signal from the secondary coil was fed back to the lock-in-amplifier for phase sensitive detection. When a superconducting sample is placed in one of the sections of second coils, any change in the magnetization of the sample (and hence the susceptibility) corresponds to a change in the emf induced in the secondary coil, which is measured by the lock-in-amplifier. Hence, for a properly calibrated and scaled system, the change in magnetization (ΔM) due to primary field amplitude (ΔH_{ac}) gives the diamagnetic susceptibility ($\chi_{ac} = \Delta M / \Delta H_{ac}$).

3.4.2 ***d.c.susceptibility***: The d.c.susceptibility measurements were performed on the commercially available "Oxford" cryogenic Vibrating Sample Magnetometer (VSM) at TIFR, Mumbai. All materials acquire a magnetic moment when placed in a magnetic field. The magnetic moment per unit volume is known as the 'Magnetization'. The VSM uses an induction technique for the measurement of magnetic moment by detecting the a.c. field produced by an oscillating sample moment. The technique is very simple.

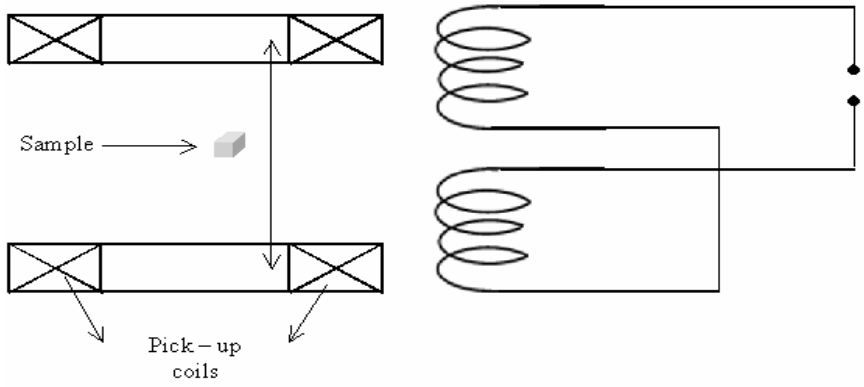

Figure 3.9 Signal generation in VSM

The sample is attached to the lower end of a rigid rod and made to oscillate vertically, typically over 1 – 1.5 mm and frequencies 40 – 80 MHz. If the sample is magnetized (either permanently or in response to an external applied field) the oscillation will induce an a.c. signal in a set of suitably pick-up or sense coils. The amplitude of this signal is proportional to the magnetic moment of the sample. This type of design, named after its inventor Simon Foner (1956) [26], is appropriate for the systems where the direction of vibration and field is parallel. Mallison designed an effective set of sense coils for system where the field direction is horizontal, that is, proportional to the vibration direction [27].

The block diagram in Figure 3.10 shows how the individual components of the system may be integrated to form a VSM.

The pick up coils are usually connected as a gradient pair such that the induced emf ’s in each coil add. This also has the advantage, if the coils are matched, of rejecting the total emf induced in the coil system by any external applied field change. The lock-in amplifier (LIA) is tuned to the vibration frequency using a reference signal from the vibrator controller and detects the in-phase voltage from sense coils.

The applied field and sample temperature may be varied under computer control. The computer may then record the LIA voltage data as a function of field, temperature or time.

In the present work, the d.c. susceptibility measurements were taken using the above setup. Magnetization as a function of temperature was measured for all the samples in order to see the paramagnetic – diamagnetic transition, thus cross-checking the superconducting T_c obtained from electrical method (resistivity measurements).

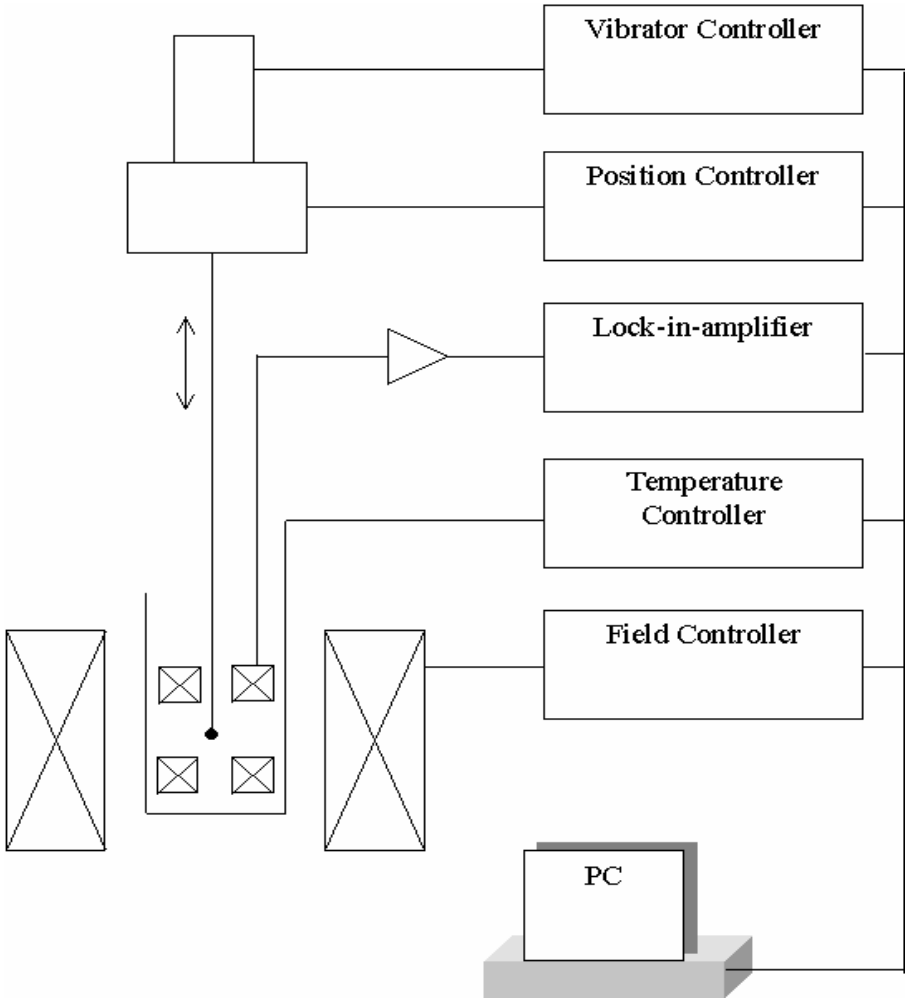

Figure 3.10 Block diagram of VSM measurement

3.4.3 ***d.c.magnetization***: The magnetization measured as a function of varying applied field at a given temperature gives the hysteresis loops. Magnetization measurements were also performed on the VSM at TIFR, using the setup described above. All the samples were studied up to 1 Tesla applied field and different temperatures (below and above T_c), in order to see the broadening of the loops to calculate current density (J_c). From the width of these loops, and using the Bean's critical state model, J_c can be calculated.

3.5 OXYGEN CONTENT DETERMINATION

3.5.1 ***Iodometric double titration***: The oxidation state of copper in the high T_c superconductor is significantly related to its superconducting property [28]. The method of double iodometric titration is generally adopted to determine the oxidation state of copper (or the average valence of copper, $2 + p$) and oxygen content z [29-32].

For the first experiment of iodometric titration, the valence number of copper in a sample equals $2 + p$. The superconducting cuprate sample is weighed [about 30 – 40 mg (w_1)] and is placed in a three-neck flask. Powdered KI, (~ 1 gm) is added so as to cover the sample. The solution is blanketed with nitrogen gas. The whole mixture is then dissolved in an acidic solution of 6N HCl (hydrochloric acid, ~10 ml) to ensure that the sample is always in contact with an excess of iodine. This yellow coloured solution is then well stirred and 6N NH_4OH (ammonium hydroxide ~ ammonia solution) is added drop wise until the solution turns in to a persistent green coloured solution. Then, 2 ml of 85% H_3PO_4 (ortho phosphoric acid) is added and the titration is carried out with 0.01 N $Na_2S_2O_3$ (sodium thiosulphate). Starch solution is used as an indicator to the titration. The volume of $Na_2S_2O_3$ required is V_1 ml, which, in turn gives the volume of iodine liberated from the sample, weighing w_1. The reactions, which take place, are as follows:

$$Cu^{1+} + I^- \rightarrow CuI$$

$$Cu^{2+} + 2I^- \rightarrow CuI + \tfrac{1}{2} I_2$$

$$Cu^{3+} + 3I^- \rightarrow CuI + I_2$$

In general the whole reaction can be written as:

$$Cu^{2+p} + (2+p)\, I^- \rightarrow CuI + 0.5\,(p+1)\, I_2$$

Where p is the hole concentration. The liberated I_2 will participate in the reaction with the solution of $Na_2S_2O_3$ as

$$I_2 + 2\, Na_2S_2O_3 \rightarrow 2NaI + Na_2S_2O_3$$

From the above reactions, it is observed that any Cu^{1+} ion present in the sample will precipitate out as CuI and without producing neutral iodine. All other species of copper having their higher oxidation level greater than Cu^{1+} will react and yield a quality of neutral iodine, which is proportional to the degree of oxidation ($p+1$). Thus the amount of neutral iodine produced has to be accurately determined using standard titration average charge or degree of oxidation of copper i.e., $(Cu\text{-}O)^{+p}$.

In the second step of iodometric titration, the sample containing copper with valence $2+p$ is first dissolved in an acidic solution to determine the total copper. The sample (weighing w_2) is dissolved in 10 ml of 6N HCl; it is then diluted to 40 ml with distilled water and heated up to nearly 50 ^{0}C. Approximately 10 ml of 6N NH_4OH is added drop by drop. The solution is simultaneously stirred till a persistent blue colour is formed. This is followed by adding 2 ml of 85% H_3PO_4 solution. This resultant solution is cooled to room temperature and blanketed with nitrogen gas. 1 g of powder KI is added and the solution is titrated with 0.01 N solution of $Na_2S_2O_3$ to a starch end point.

The second titration thus gives the volume V_2 of the solution of $Na_2S_2O_3$ required to titrate the iodine generated from sample weighing w_2. The reactions involved in the second titration are:

$$Cu^+ + H^+ \rightarrow Cu^{2+} + H_2O$$

$$[Cu\text{-}O]^{-p} \rightarrow [Cu\text{-}O] + O_2$$

By using the known values of V_1, V_2 and w_1, w_2 in the following formula to calculate the excess number of divalent copper,

$$p = \left[\frac{V1/w1}{V2/w2} \right] - 1$$

Thus, by determining the effective oxidation level or effective copper valence, i.e., *2+p*, the oxygen content is calculated assuming that the stochiometric is known. In order to obtain the exact value of oxygen content, the titration is usually repeated 2-3 times and average readings are used. For example, for calculating the oxygen content (z) of $La_2Ca_1Ba_2Cu_5O_z$ sample, the following relation has been

$$2z = 7(2+p) + 11$$

or

$$z = 3.5(2+p)+5.5$$

where, z is the oxygen content per La-2125 unit cell. Actually, these relations are derived from the relations for RE-123 system. Since RE-123 and La-2125 are isostructural, hence, the modification of the relation is justified. The values of the oxygen content thus obtained can be verified by the values of oxygen content obtained from neutron diffraction data analysis, done using Rietveld refinement.

3.5.2 ***Neutron diffraction***: Scattering powers of the neutrons are dependent on the nuclear energy levels, and not on the atomic numbers. Hence, it gives a great advantage in identifying individual species present in the structure. Since the oxygen is a light atom, the oxygen is largely suppressed in the X-ray diffraction pattern. Neutron powder diffraction has been the major player in crystal structure studies of

various high T_c materials since discovered and has gone far in elucidating the structural origins, or requirements, of superconductivity. One important parameter is the distribution of oxygen atoms between two incompletely filled sites. The ability of neutrons to be scattered prominently by even light atoms gives an advantage in determining the oxygen content. In the Rietveld refinement of the neutron diffraction data, the oxygen occupancy can be varied and exact values can be determined. Since, oxygen plays a major role in the structural and superconducting properties of high temperature superconductors; it is highly appreciable to ascertain the exact oxygen content values, which in turns gives exact bond lengths and bond angles.

REFERENCES

[1] J. T. Cheung and J. Madden

J. Vac. Sci, Tech **B 5 (3)**, 705 (1987)

[2] J. T. Cheung and T. Magee

J. Vac. Sci. Tech, **A1 (3)**, 1604 (1983)

[3] J. T. Cheung and H. Sankur

CRC Crit. Rev. Solid State Mater. Sci, **15**, 65 (1988)

[4] J. T. Cheung

Appl. Phys. Lett. **43(3)**, 255 (1983)

[5] S. P. Gapanov, B. M. Luskin and N. N. Salaschenko

Sov. Tech. Phys. Lett. **5**, 210 (1979)

[6] S. V. Gapanov, A. Gudkov and A. A. Fraerman

Sov. Phys. Tech. Lett **27(9)**, 1130 (1982)

[7] D. Basting, K. Mohla, E. Albers and M. V. Bergmann

Lasers & Optoeleckronik, **2**, 128 (1984)

[8] B.D. Culity

"X-Ray Diffraction ", Pub: Addison-Wesly Pub. Co. Inc. (1978)

[9] G.E. Beacon

"Neutron Diffraction" , Pub: Oxford Press (1972)

[10] Roland Tellgren

Proc. Of ISPD-1998, Ed. S.P. Sengupta, Pg. 45 (1998}

[11] C. Dong

J. Appl. Cryst. **32**, 838 (1999)

[12] Juan Rodriguez-Carvajal (`Version 3.5d Oct98-LLB-JRC`)

Laboratoire Leon Brillouin (CEA-CNRS)

[13] W. Kraus and G. Nozle (Version 2.3 – 1999)

Federal Institute for Materials Research and Testing

Rudower Cahussee **5**, 12489, Berlin (Germany)

[14] H. M. Rietveld

Acta. Cryst. **22**, 151 (1967)

[15] H. M. Rietveld

J. Appl. Cryst. **2**, 65 (1969)

[16] L.B. McCusker, R. B. Von Dreele, D. E. Cox, D. Louer and P. Scardi

J. Appl. Cryst. **32**, 36 (1999)

[17] R. A. Young

"The Rietveld Method", IUCr & Oxford Science Publications (1996)

[18] W. Richard Bowen, Teodora Doneva, Nidal Hilal and Chris J. Wright

Microscopy and Analysis, **13**, January 2001

[19] T. R. Albrecht, P. Grutter, D. Horne and D. Rugar

J. Appl. Phys **69(2)**, 668 (1991)

[20] A. L. Weisenhorn, P. K. Hansma, T. R. Albrecht and C. F. Quate

Appl. Phys. Lett. **54(26)** 2651 (1989)

[21] G. Meyer and N. M. Amer

Appl. Phys. Lett **57(20)**, 2089 (1990)

[22] C.A. J. Putman, B.G. De Grooth, N. F. Van Hulst and J. Greve

J. Appl. Phys. **72(1)**, 6 (1992)

[23] Phil Russell, Dale Batchelor and John Thornton

Microscopy and Analysis, 13, July 2001

[24] E. M. Engler

Chem. Technol. **17**, 542 (1981)

[25] H. C. Montgomery

Philips Research Reports, **13**, 1 (1958)

[26] S. Foner

Rev. Sci. Instr. **30**, 548 (1959)

[27] Mallinson

J. Appl. Phys. **37**, 2514 (1966)

[28] W. M. Chen, C.C. Lan, J. F. Geng, L.Y. Li, K. C. Hung and X. Jin

Physica C, **270**, 155 (1996)

[29] A. L. Nazzal, Y. Lee, E. M. Engler, R. D. Jacowitz, Y. Tokura and

J. B. Torrance

Physica C, **153**, 1367 (1988)

[30] Y. Matsuma, H. Teraoka, K. Sugiyamma, F. Nakamura and T. Fujita

Physica C, **185**, 587 (1991)

[31] S. Degoy, J. Jinenez, P. Martin, O. Martinez, A. C. Prieto, D. Chambonnet,

C. Audry, C. Belouet and J. Perriere

Physica C, **256**, 291 (1996)

[32] K. Kishio, J. I. Shimoyama, T. Asegawa, K. Kitazawa and K. Fueki

Jpn. J. Appl. Phys, **26**, L1228 (1987)

CHAPTER - IV

Studies on $La_{2-x}Dy_xCa_yBa_2Cu_{4+y}O_z$ system

INTRODUCTION

It is reported that, the synthesis and repetitiveness in the superconducting properties of $LaBa_2Cu_3O_z$ (La-123) system, has remained a problem to be solved till date [1-3]. Extensive studies have been carried out on the La-based superconductors in order to stablise the superconducting phase in them by the addition of Ca [4-5]. The Ca-doped 123 superconductors' exhibit tetragonal structure and superconductivity $T_c \sim 5$ - 10 K, lower than most of the orthorhombic 1-2-3 materials [6]. Substitution is a simple way to introduce the holes in the conducting CuO_2 layers of high T_c cuprate superconductors. For example, substituting part of La-atoms with Ca, Sr or Ba atoms in the La_2CuO_4 would increase the amount of $[Cu\text{-}O]^+$ and a transformation from semi-conductor to superconductor [7]. In the course of present work, an attempt is made to obtain a superconducting phase from non-superconducting $La_2Ba_2Cu_4O_z$ (La-224) by the addition of equal amounts of CaO and CuO along with the substitution of rare earth metal ion like Dy at La site.

In this chapter, studied on synthesis of the $La_{2-x}Dy_xCa_yBa_2Cu_{4+y}O_z$ (LaDyCaBCO); x = 0.1 – 0.5, y = 2x, samples obtained by adding equal amounts of CaO and CuO to La-224 along with substitution of Dy^{3+} for La^{3+} have been reported. Detailed structural studies have been carried out by using neutron diffraction and X-ray diffraction measurements and analyzing the data by Rietveld analysis technique. The neutron diffraction studies provide an accurate determination of the oxygen atom positions, the bond lengths and site occupancies of La, Ca and Ba ions in LaDyCaBCO system. The interrelationship between the superconducting transition

temperature, dopant valency and the variation in the oxygen content is discussed in the context of the hole concentration.

In addition to the bulk studies, the thin films of the LaDyCaBCO compounds were synthesized for the first time using Pulsed Laser Deposition (PLD) technique. Structural and superconducting properties of thin films were studied using variety of experimental techniques. The tetragonal thin films possess stable properties and longer life [8, 9]. The La-2125 mixed oxide superconductors exhibit tetragonal structure throughout the CaO and CuO doping range, up to (x = 0.5, y = 1.0). It is thus interesting to synthesis and study the properties of thin films of these compounds for possible device applications.

4.1 STRUCTURAL STUDIES

4.1.1 In Bulk form

(a) ***X-ray Diffraction***: The Figure 4.1 shows the indexed XRD patterns for the $La_{2-x}Dy_xCa_yBa_2Cu_{4+y}O_z$ (x = 0.1 – 0.5; y = 2x) [LaDyCaBCO] system. The XRD patterns were recorded at room temperature at TIFR, Mumbai using Cu-K_α radiation with wavelength, λ = 1.5408 Å.

The XRD patterns clearly show the single-phase nature of all the samples with tetragonal symmetry. The values of unit cell parameters, calculated by least square method are tabulated in Table 4.1.

The X-ray data was analyzed by ***Rietveld analysis method*** for detailed structural studies using the FULLPROF Rietveld refinement program. The details about the various X-ray data fitting softwares used to obtain the values of unit cell parameters and other structural parameters are given in Chapter III (Section 3.2) in the

form of a flow chart (Figure 3.5). After preliminary XRD data analysis, Rietveld FULLPROF program was used for detailed structural refinement.

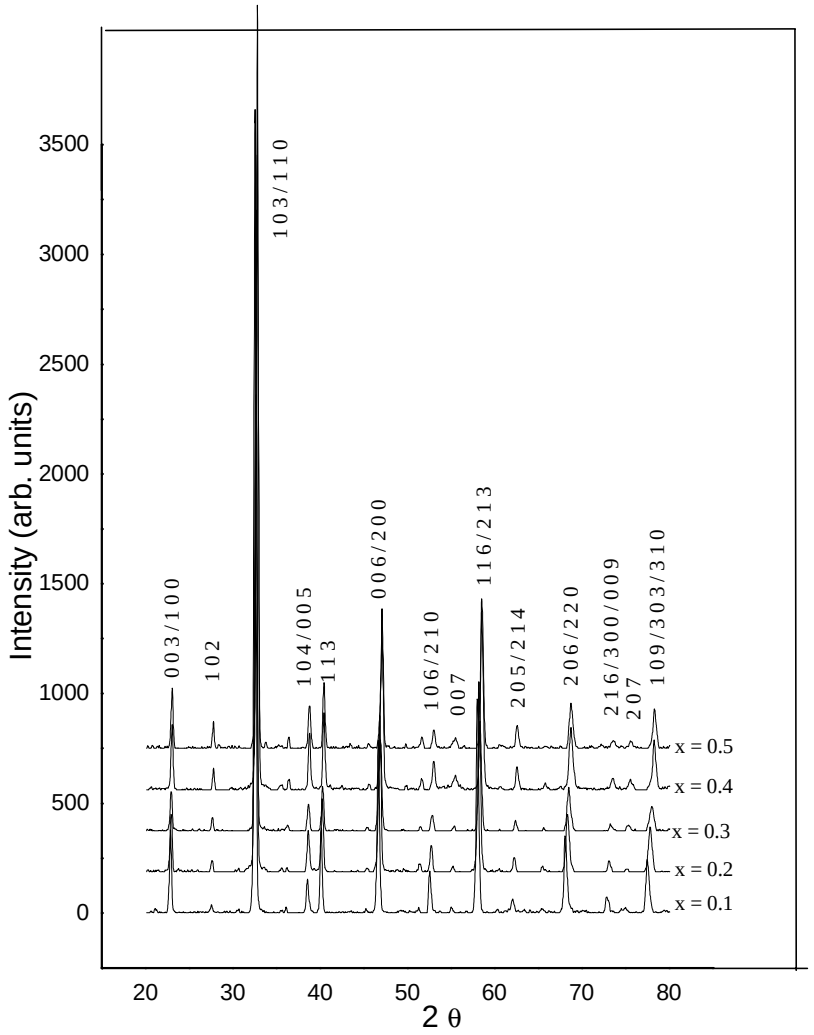

Figure 4.1 ***Indexed XRD patterns of $La_{2-x}Dy_xCa_yBa_2Cu_{4+y}O_z$ (x = 0.1 – 0.5; y = 2x) system***

Table 4.1 ***Values of unit cell parameters, unit cell volume and X-ray density of LaDyCaBCO samples***

Sample (x, y)	**Unit cell Parameters**		**Volume (Å)^3**	**X-ray density (gm / cm^3)**
	(a= b) Å	(c) Å		
(0.1, 0.2)	3.8954 (3)	11.6890 (8)	177.3748	9.1740
(0.2, 0.4)	3.8828 (3)	11.6461 (8)	175.5842	9.5462
(0.3, 0.6)	3.8710 (3)	11.6210 (8)	174.1429	9.9063
(0.4, 0.8)	3.8643 (3)	11.6750 (8)	174.3420	10.1758
(0.5, 1.0)	3.8670 (3)	11.6760 (8)	174.5992	10.4648

The La-224, the starting compound (x = 0.0, y = 0.0) can be normalized to La-123 form as follows:

$La_2Ba_2Cu_4O_z$ (La-224) = La-224 (La: Ba: Cu = 1:1: 2)

= $(La_2Ba_2Cu_4O_z) * ¾$

= $(La_{1.5}Ba_{1.5}Cu_3O_{z'})$ = (La: Ba: Cu = 1:1:2)

= $La_1(Ba_{1.5}La_{0.5})Cu_3O_{z'}$ → La-123 … (1)

Hence starting model of Y-123 tetragonal system with P4/MMM space group (No. 123) was assumed in starting the analysis [10]. During refinement, variable parameters like atomic positions, occupancies of different ions (except oxygen), unit cell parameters etc were varied for obtaining a matching fit between the observed and calculated patterns. Figures 4.2 (a-e i.e., x = 0.1 – 0.5) show the Rietveld fitted patterns of the LaDyCaBCO system.

The patterns fit very well into the assumed model, thus confirming the atomic positions and the space group. It also confirms the phase purity of all the samples

studied. Rietveld analysis of the XRD data gives the accurate values of unit cell parameters, site occupancies and oxygen content in the samples.

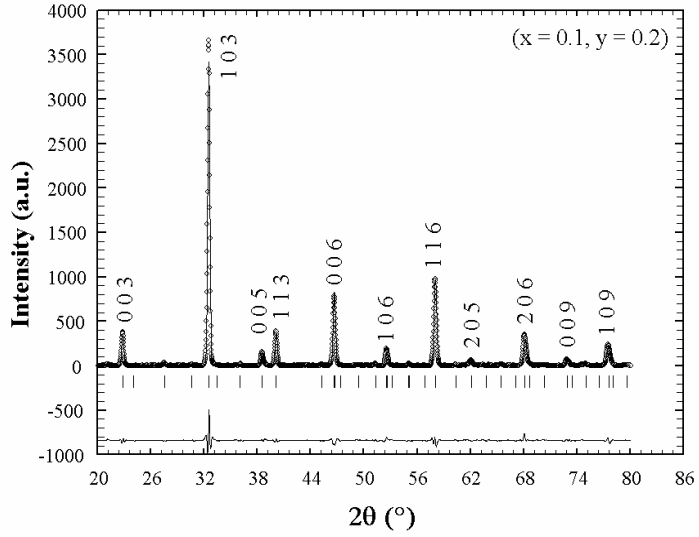

Figure 4.2 (a) XRD Rietveld fitted pattern of $La_{1.9}Dy_{0.1}Ca_{0.2}Ba_2Cu_{4.2}O_z$

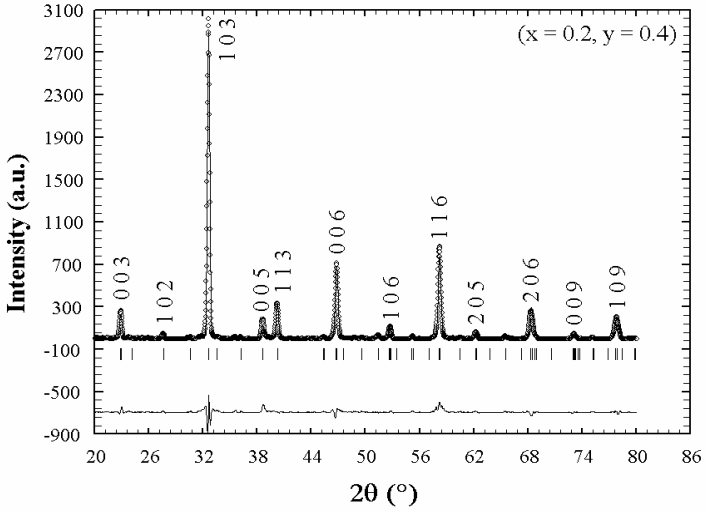

Figure 4.2 (b) XRD Rietveld fitted pattern of $La_{1.8}Dy_{0.2}Ca_{0.4}Ba_2Cu_{4.4}O_z$

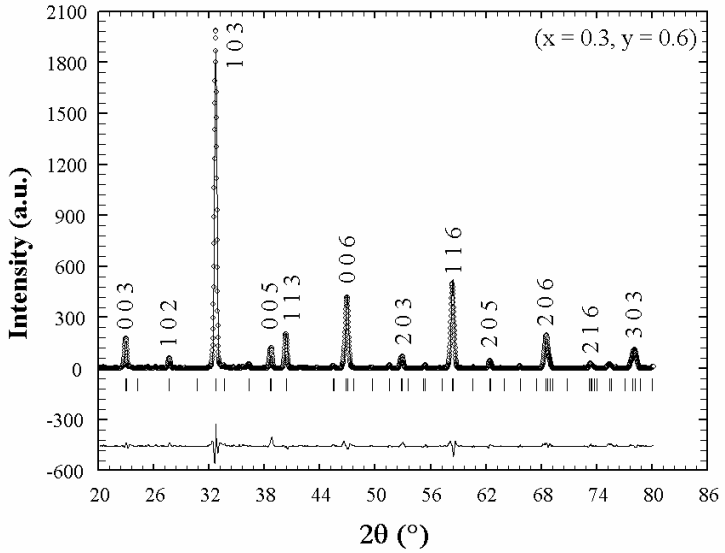

Figure 4.2 (c) XRD Rietveld fitted pattern of $La_{1.7}Dy_{0.3}Ca_{0.6}Ba_2Cu_{4.6}O_z$

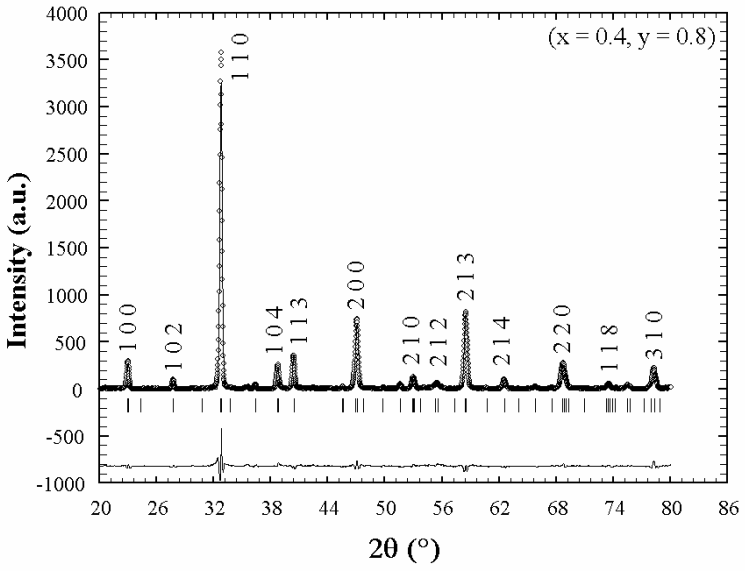

Figure 4.2 (d) XRD Rietveld fitted pattern of $La_{1.6}Dy_{0.4}Ca_{0.8}Ba_2Cu_{4.8}O_z$

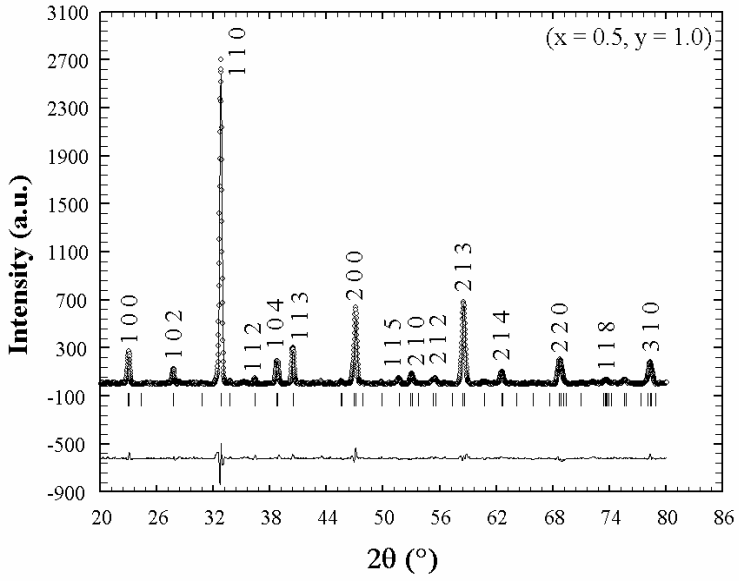

Figure 4.2 (e) XRD Rietveld fitted pattern of $La_{1.5}Dy_{0.5}Ca_1Ba_2Cu_5O_z$

The results of the detailed Rietveld analysis on the XRD data are tabulated in Table 4.2. The results clearly show that, with increasing Ca^{2+} and Dy^{3+} concentration (smaller ionic radii elements as compared to La^{3+} and Ba^{2+}), the unit cell parameters decreases along with the unit cell volume. Since the X-rays are not sensitive to the oxygen content, oxygen values were kept fixed during the refinement. The atomic positions, thermal parameters and unit cell parameters were varied during the refinement cycles, and the best-fit values have been tabulated in the table.

Table 4.2 Values obtained from XRD Rietveld analysis

	Sample (x, y)				
Parameters	(0.1, 0.2)	(0.2, 0.4)	(0.3, 0.6)	(0.4, 0.8)	(0.5, 1.0)
Space group	P4/MMM	P4/MMM	P4/MMM	P4/MMM	P4/MMM
a = b (Å)	3.8920 (3)	3.8773 (3)	3.8666 (3)	3.8585 (3)	3.8564 (3)
c (Å)	11.6720 (8)	11.6805 (8)	11.6434 (8)	11.6272 (8)	11.6201 (8)
La/Nd/Ca (½, ½, ½)					
N_{La}	0.8289	0.6223	0.4615	0.4747	0.3039
N_{Dy}	0.0432	0.1360	0.1956	0.2247	0.3039
N_{Ca}	0.0432	0.0863	0.2890	0.2247	0.4039
Ba (½,½, z)					
z	0.1790	0.1776	0.1801	0.1846	0.1854
N	1.4187	1.3454	1.3043	1.3036	1.2443
La @ Ba (N)	0.4901	0.5254	0.6555	0.5539	0.6443
Ca @ Ba (N)	0.0616	0.1064	0.2044	0.3039	0.2443
Cu (1) (0,0,0)					
N	1.0000	1.0000	1.0000	1.0000	1.0000
Cu (2) (0,0,z)					
z	0.3507	0.3539	0.3476	0.3544	0.3562
N	2.0000	2.0000	2.0000	2.0000	2.0000
O (1) (0,½,0)					
N	0.8000 (3)	0.7000 (3)	0.6700 (3)	0.6300 (3)	0.6000 (3)
O (2) (0,0,z)					
z	0.1643	0.1524	0.1673	0.1763	0.1667
N	2.0000	2.0000	2.0000	2.0000	2.0000
O (4) (0,½,z)					
z	0.3745	0.3319	0.3662	0.3690	0.3702
N	4.0000	4.0000	4.0000	4.0000	4.0000
Total Oxygen					
(z' – in 123)	6.8000 (3)	6.7000 (3)	6.6700 (3)	6.6300 (3)	6.6000 (3)
(z – in 2125)	9.5200 (5)	9.8266 (5)	10.2273 (5)	10.6080 (5)	11.0000 (5)
R-factors					
χ^2	2.55	3.20	2.05	3.78	2.60
R_{wp}	23.3	27.7	27.7	27.9	26.3
R_p	14.6	15.5	19.3	14.3	16.3

(b) ***Neutron Diffraction***: Neutron diffraction (ND) is a very powerful tool in obtaining the exact structural information of any unknown compound from the powder diffraction data. The neutron diffraction technique is best suited for estimating the actual site occupancies and atomic positions [11]. It also gives the accurate oxygen content in the sample, which is very essential for the superconducting properties of mixed oxide superconductors [12].

The neutron diffraction experiments were performed on the polycrystalline samples of LaDyCaBCO system on a powder diffractometer (TT1015) at Dhurva Reactor, BARC Mumbai. The samples were taken up for neutron diffraction at room temperature using neutrons of wavelength $\lambda = 1.094$ (except for $x = 0.4$ sample). The Figures 4.3 (a-e) shows the Rietveld fitted neutron diffraction plots for all the samples of LaDyCaBCO system.

The detailed analysis of the ND data carried out using FULLPROF Rietveld refinement method [13] resulted in to the values of crystallographic site occupancies of constituent ions at different atomic positions, oxygen content, unit cell parameters etc; which are tabulated in Table 4.3. The details of FULLPROF refinement program and the features have been discussed in Chapter-III (Section 3.2).

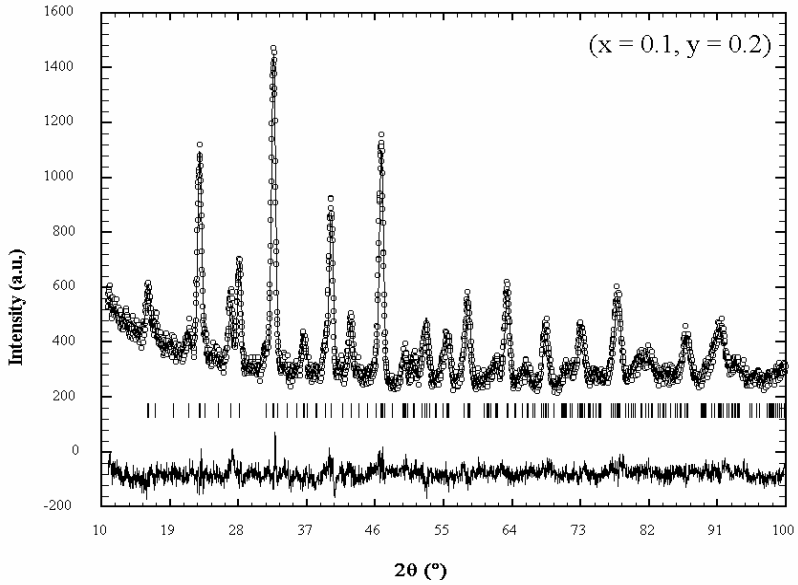

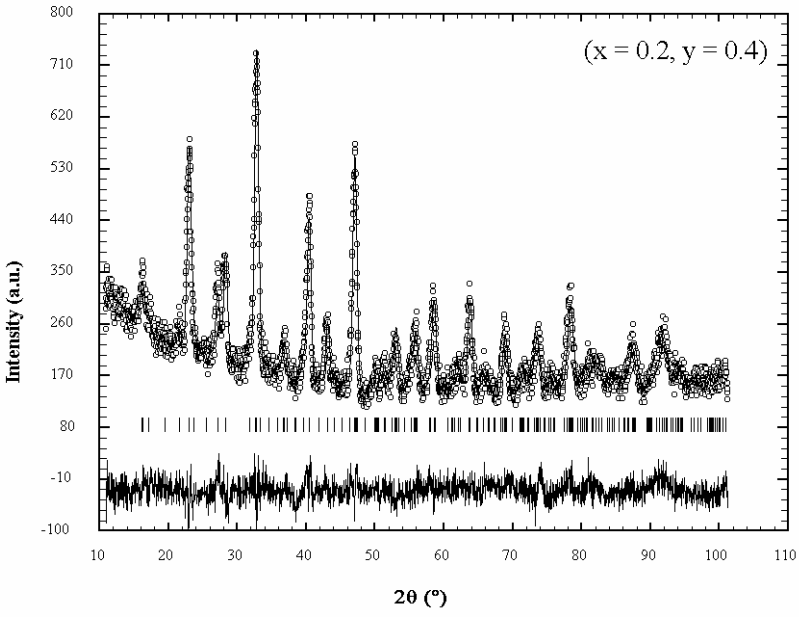

Figure 4.3 (a & b) ***Rietveld fitted neutron diffraction plots of x = 0.1 & 0.2 samples***

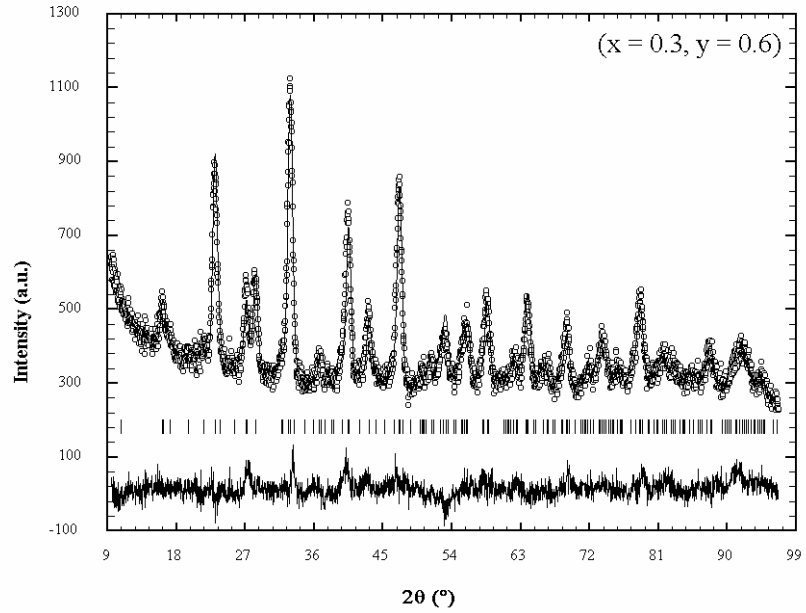

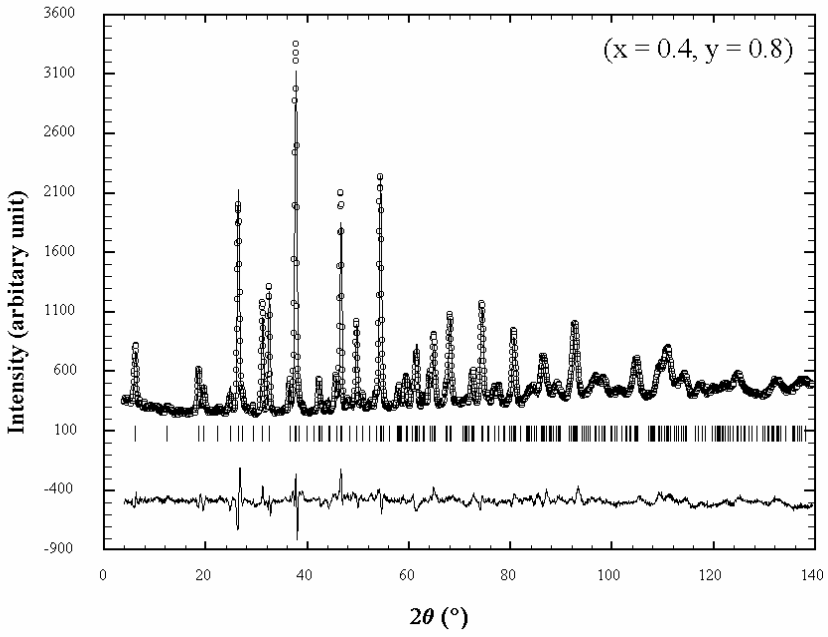

Figure 4.3 (c & d) Rietveld fitted neutron diffraction plots of x = 0.3 & 0.4 samples

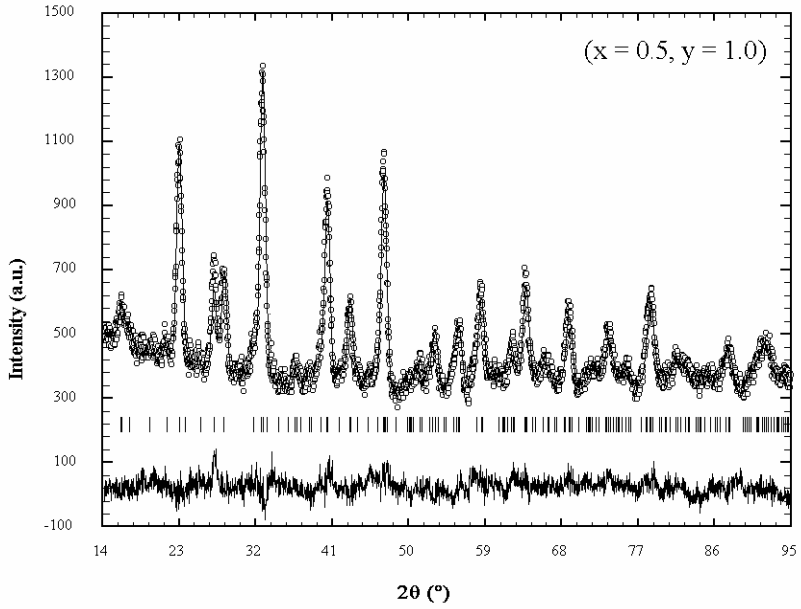

Figure 4.3 (e) Rietveld fitted neutron diffraction plot of x = 0.5 samples

The neutron diffraction pattern for x = 0.4 (y = 0.8) sample has been recorded on a modified neutron powder diffractometer with wavelength 1.248 Å. The 2θ range has been $5 – 139^0$ for this particular sample. The analysis of the neutron diffraction data on x = 0.4 sample has been done on the similar lines of rest of the samples. The results of the analysis have been tabulated in Table 4.3, along with the results of other samples (x = 0.1 – 0.5).

Table 4.3 ***Values of unit cell parameters, site occupancies and R- factors obtained from Rietveld analysis of Neutron Diffraction data***

	Sample (x, y)				
Parameters	(0.1, 0.2)	(0.2, 0.4)	(0.3, 0.6)	(0.4, 0.8)	(0.5, 1.0)
Space group	P4/MMM	P4/MMM	P4/MMM	P4/MMM	P4/MMM
a = b (Å)	3.8935 (3)	3.8705 (3)	3.8606 (3)	3.8611 (3)	3.8670 (3)
c (Å)	11.7293 (8)	11.6593 (8)	11.6825 (8)	11.6402 (8)	11.6763 (8)
La/Nd/Ca (½, ½, ½)					
N_{La}	0.804	0.614	0.554	0.405	0.300
N_{Dy}	0.071	0.136	0.196	0.250	0.300
N_{Ca}	0.125	0.250	0.250	0.316	0.400
Ba (½,½, z)					
z	0.1804	0.1830	0.1819	0.1864	0.1868
N	1.251	1.364	1.304	1.250	1.200
La @ Ba (N)	0.507	0.614	0.554	0.606	0.600
Ca @ Ba (N)	0.319	0.023	0.141	0.195	0.200
Cu (1) (0,0,0)					
N	1.000	1.000	1.000	1.000	1.000
Cu (2) (0,0,z)					
z	0.3494	0.3490	0.3526	0.3529	0.3526
N	2.0000	2.0000	2.0000	2.0000	2.0000
O (1) (0,½,0)					
N	0.929	0.995	0.989	0.861	0.937
O (2) (0,0,z)					
z	0.1619	0.1614	0.1601	0.1591	0.1653
N	2.254	2.0000	2.245	2.407	1.9666
O (4) (0,½,z)					
z	0.3634	0.3656	0.3669	0.3684	0.3706
N	3.844	4.0000	3.8010	3.9710	3.9130
Total Oxygen					
(z' – in 123)	7.027	6.9950	7.035	7.2390	6.8166
(z – in 2125)	9.8378	10.2593	10.787	11.582	11.361
R-factors					
χ^2	1.47	1.35	1.50	2.33	1.51
R_{wp}	6.40	8.12	6.28	7.10	5.86
R_p	5.04	6.40	4.93	5.48	4.63

During the refinement procedure, single phase fit with tetragonal space group P4/MMM was attempted with ***Gaussian peak shape***. All possible positional (x, y, z), thermal parameters (B) and occupational (N) parameters were varied in addition to cell parameters, half width parameters, background parameters, zero angle and scale factor. These parameters were varied in separate cycles due to a strong correlation between the thermal and occupancy parameters. The occupancy fractions of Ba and La ions at Ba-sties were refined assuming that no vacancies are present at these sites. The occupancy fractions of La were refined assuming all substituted Dy and Ca ions occupy La-site only (for non-zero values of x and y). As a result of refinement, very good fits were obtained for all the five samples refined on the basis of standard tetragonal 1-2-3 structural model with the final values of profile R-factors (R_p) converging [Figures 4.3 (a-e)]

Using the results obtained from the neutron diffraction analysis, bond lengths were calculated for different ions using **Powder Cell**. The results are given in Table 4.5. Based on these structural observations a model of structure for La-2125 unit cell has been proposed for the first time.

The refinement of the neutron data on LaDyCaBCO samples has been done according to the RE-123 tetragonal structure model and, hence it is imperative to establish the relation between RE-123 and La-2125 structures. Figure 4.4 shows the unit cell of La-2125 structure when normalized to La-123 (tetragonal) form, while Figure 4.5 depicts the crystallographic unit cell of La-2125 sample consisting of four CuO_2 sheets contributing four Cu-atoms and two Cu-O chains contributing one Cu-atom each.

It is well known that the $REBa_2Cu_3O_z$ (R = Y, Er, Gd etc) phase posses a layered structure with a sequence along c-axis of the

$Cu(1)O_x$ – BaO – $Cu(2)O_2$ – RE – $Cu(2)O_2$ – BaO – $Cu(1)O_x$ [12] with one Cu(1) chain site and two Cu(2) plane sites. In a similar fashion, the sequence along the c-axis for the layered structure $La_2Ca_1Ba_2Cu_5O_z$ can be written as

$Cu(1)O_x$ – BaO – $Cu(2)O_2$ – La – $Cu(2)O_2$ – CaO - $Cu(2)O_2$ – La - $Cu(2)O_2$ – BaO - $Cu(1)O_x$, hence it is assumed that the La-2125 structure possess four Cu(2) plane sites and one Cu(1) site as clearly depicted in Figure 4.5.

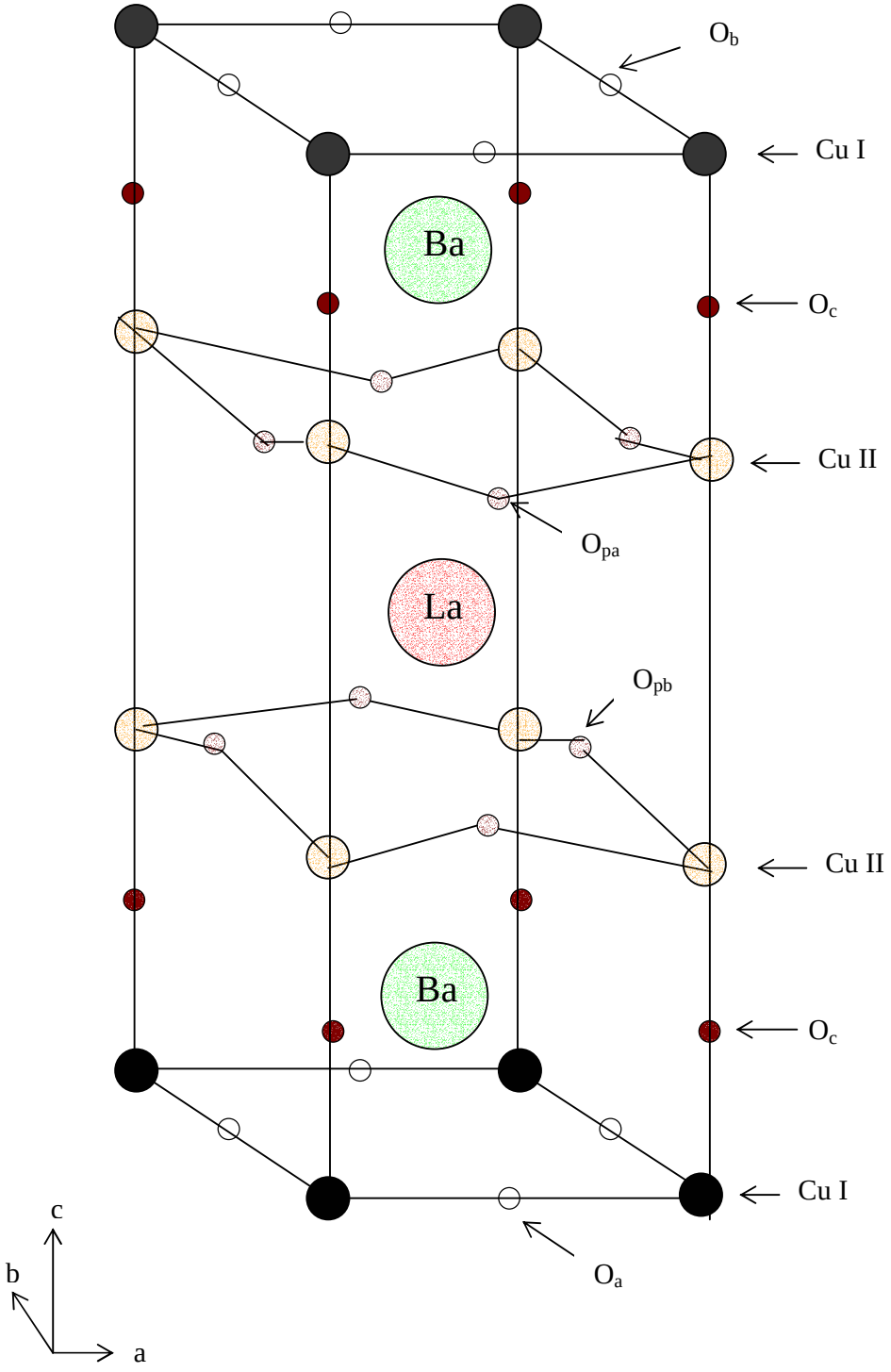

Figure 4.4 Unit cell of La-2125 structure - normalized RE-123 (Tetragonal) type

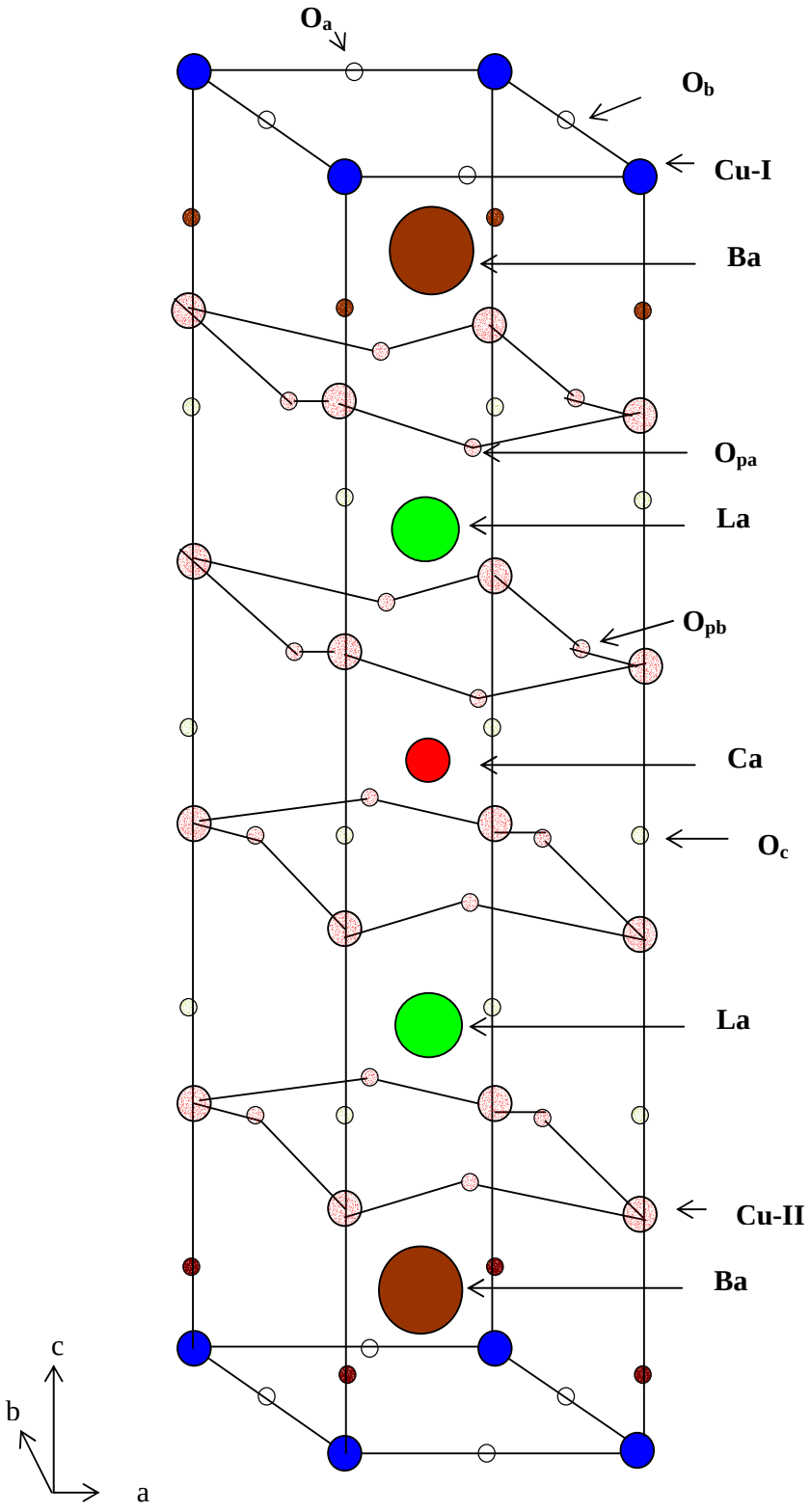

Figure 4.5 Unit cell of proposed La-2125 structure

The La-2125 structure can be normalized to La-123 form by the following relation:

La-2125	⇔	La-123	
$La_2Ca_1Ba_2Cu_5O_z$	=	$(La_2Ca_1Ba_2Cu_5O_z)$ X (3/5)	
	=	$La_{1.2}Ca_{0.6}Ba_{1.2}Cu_3O_z$,	
	=	$La_1(Ba_{1.2}Ca_{0.6}La_{0.2})Cu_3O_z$,	… (2)
	=	La-123 (1: 2: 3)	

Similarly, the $La_{1.9}Dy_{0.1}Ca_{0.2}Ba_2Cu_{4.2}O_z$ can be normalized to La-123 form as:

$La_{1.9}Dy_{0.1}Ca_{0.2}Ba_2Cu_{4.2}O_z$	=	$(La_{1.9}Dy_{0.1}Ca_{0.2}Ba_2Cu_{4.2}O_z)$ X (3/4.2)	
	=	$La_{1.36}Dy_{0.08}Ca_{0.14}Ba_{1.42}Cu_3O_z$,	
	=	$(La_{0.92}Dy_{0.08})(Ba_{1.42}Ca_{0.14}La_{0.44})Cu_3O_z$,	… (3)
	=	La-123 (1: 2: 3)	

And also, the $La_{1.5}Dy_{0.5}Ca_1Ba_2Cu_5O_z$ can be normalized to La-123 form as:

$La_{1.5}Dy_{0.5}Ca_1Ba_2Cu_5O_z$	=	$(La_{1.5}Dy_{0.5}Ca_1Ba_2Cu_5O_z)$ X (3/5)	
	=	$La_{0.9}Dy_{0.3}Ca_{0.6}Ba_{1.2}Cu_3O_z$,	
	=	$(La_{0.3}Dy_{0.3}Ca_{0.4})(Ba_{1.2}Ca_{0.2}La_{0.6})Cu_3O_z$,	… (4)
	=	La-123 (1: 2: 3)	

The stochiometries obtained from neutron diffraction, for LaDyCaBCO compounds have been tabulated in Table 4.4, which gives the values of the stoichiometries as calculated and obtained from Rietveld analysis. Table 4.5 lists the values of various bond distances between Cu-O, Ba-O and La-O atoms, for different Dy-Ca doped LaDyCaBCO samples. It can be seen that, the Cu-O bond lengths do not show an appreciable change while La-O_{pab} bond length decreases with increasing Ca-concentration due to increase occupancy of smaller Ca^{2+} ions at La^{3+} site.

Table 4.4 ***Occupancies of different atoms obtained from the refinement (in 1-2-3 & 2-1-2-5) stoichiometries***

Sample	**$La_{1.9}Dy_{0.1}Ca_{0.2}Ba_2Cu_{4.2}O_z$**			
Atoms	***Initial value** (as taken in stochiometric formula) **in 2125 form***	***Reduced to 1-2-3 type** (3 / total no. of copper present per stochiometric formula)*	***Obtained from refinement** (in 123 form)*	***Final stoichiometry** (in 2125 form = no. of copper present per stochiometric formula / 3)*
La	1.9000	1.3570	1.3110	1.8354
Dy	0.1000	0.0714	0.0710	0.0994
Ca	0.2000	0.1430	0.4440	0.6216
Ba	2.0000	1.4280	1.2510	1.7514
Cu	4.2000	3.0000	3.0000	4.2000
O	z	z’	7.0270	9.8378
Sample	**$La_{1.8}Dy_{0.2}Ca_{0.4}Ba_2Cu_{4.4}O_z$**			
Atoms	Initial value (as taken in stochiometric formula) in 2125 form	Reduced to 1-2-3 type (3 / total no. of copper present per stochiometric formula)	Obtained from refinement (in 123 form)	Final stochiometry (in 2125 form = no. of copper present per stochiometric formula / 3)
La	1.8000	1.2270	1.2280	1.8010
Dy	0.2000	0.1360	0.1360	0.1994
Ca	0.4000	0.2727	0.2730	0.4004
Ba	2.0000	1.3636	1.3640	2.0005
Cu	4.4000	3.0000	3.0000	4.4
O	z	z’	6.9950	10.2593
Sample	**$La_{1.7}Dy_{0.3}Ca_{0.6}Ba_2Cu_{4.6}O_z$**			
Atoms	Initial value (as taken in stochiometric formula) in 2125 form	Reduced to 1-2-3 type (3 / total no. of copper present per stochiometric formula)	Obtained from refinement (in 123 form)	Final stoichiometry (in 2125 form = no. of copper present per stochiometric formula / 3)
La	1.7000	1.1080	1.1080	1.7000
Dy	0.3000	0.1950	0.1960	0.3005
Ca	0.6000	0.3910	0.3910	0.5995
Ba	2.0000	1.3040	1.3040	1.9994
Cu	4.6000	3.0000	3.0000	4.6000
O	z	z’	7.035	10.7870

Table 4.4 Continued…

Sample	$La_{1.6}Dy_{0.4}Ca_{0.8}Ba_2Cu_{4.8}O_z$			
Atoms	Initial value (as taken in stochiometric formula) in 2125 form	Reduced to 1-2-3 type (3 / total no. of copper present per stochiometric formula)	Obtained from refinement (in 123 form)	Final stoichiometry (in 2125 form = no. of copper present per stochiometric formula / 3)
La	1.6000	1.0000	1.011	1.6176
Dy	0.4000	0.2500	0.250	0.5000
Ca	0.8000	0.5000	0.511	0.8176
Ba	2.0000	1.2500	1.2500	2.0000
Cu	4.8000	3.0000	3.0000	5
O	Z	z’	7.240	11.5820
Sample	$La_{1.5}Dy_{0.5}Ca_1Ba_2Cu_5O_z$			
Atoms	Initial value (as taken in stochiometric formula) in 2125 form	Reduced to 1-2-3 type (3 / total no. of copper present per stochiometric formula)	Obtained from refinement (in 123 form)	Final stoichiometry (in 2125 form = no. of copper present per stochiometric formula / 3)
La	1.5000	0.9000	0.9000	1.5000
Dy	0.5000	0.3000	0.3000	0.5000
Ca	1.0000	0.6000	0.6000	1.0000
Ba	2.0000	1.2000	1.2000	2.0000
Cu	5.0000	3.0000	3.0000	5
O	Z	z’	6.8166	11.3610

Table 4.5 Bond distances for LaDyCaBCO samples calculated from Neutron diffraction results

Bond length (Å)	**Dy & Ca-concentration (x, y)**				
	(0.1,0.2)	*(0.2, 0.4)*	*(0.3, 0.6)*	*(0.4, 0.8)*	*(0.5,1.0)*
Cu1 - O_{ab}	1.9467	1.9353	1.9303	1.9305	1.9335
Cu1 - O_c	1.8990	1.8818	1.8704	1.8520	1.9301
Cu 2 - O_{pab}	1.9537	1.9449	1.9375	1.9390	1.9449
Cu 2 - O_c	2.1992	2.1873	2.2489	2.5559	2.1870
La – O_{pab}	2.5213	2.4901	2.4787	2.4645	2.4538
Ba – O_{ab}	2.8753	2.8806	2.8709	2.9043	2.9148
Ba – O_c	2.7617	2.7484	2.7417	2.7487	2.7459
Ba – O_{pab}	2.8978	2.8711	2.8978	2.8662	2.8886

(c) ***Scanning Electron Microscopy (SEM)***: The SEM studies were carried out on the polycrystalline bulk samples of the LaDyCaBCO system in order to determine the average grain size and for studying the grain morphology. Figure 4.6 shows the SEM photographs for all the LaDyCaBCO samples, taken at X 5000 magnification (Figures 4.6 a – d) and at X 10,000 magnification (Figure 4.6 e - f). It can be observed from SEM pictures that, the superconducting grain structure is well developed and shows good packing of the grains. The average grain size of the LaDyCaBCO samples lies in the range 1800 Å – 2300 Å.

(a) x = 0.1, y = 0.2 @ 5k magnification

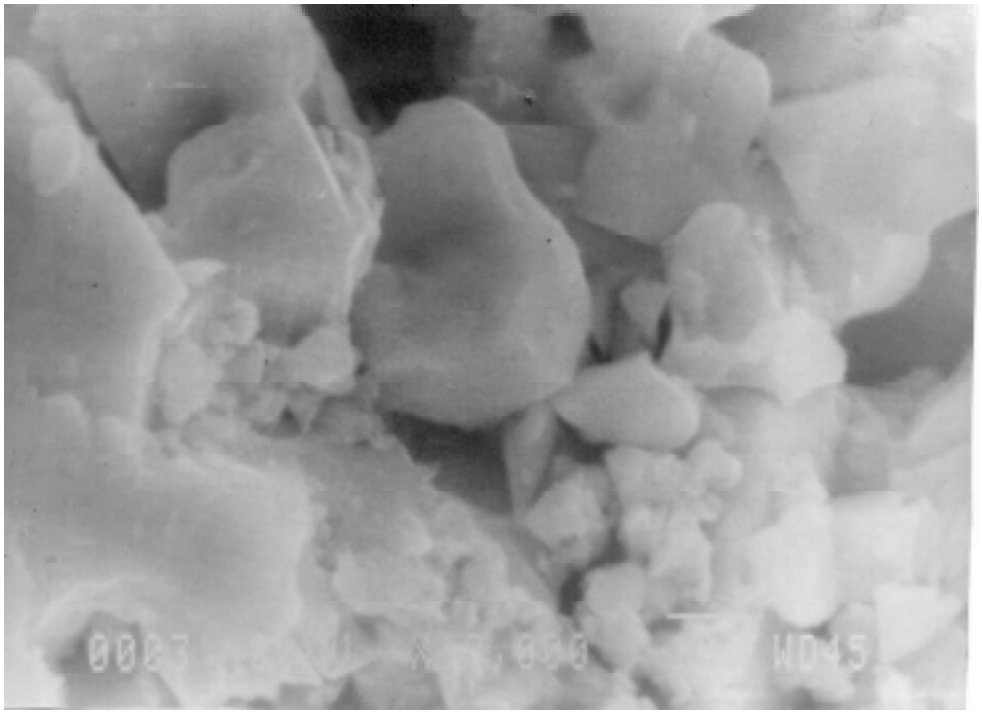

(b) x = 0.2, y = 0.4 @ 5k magnification

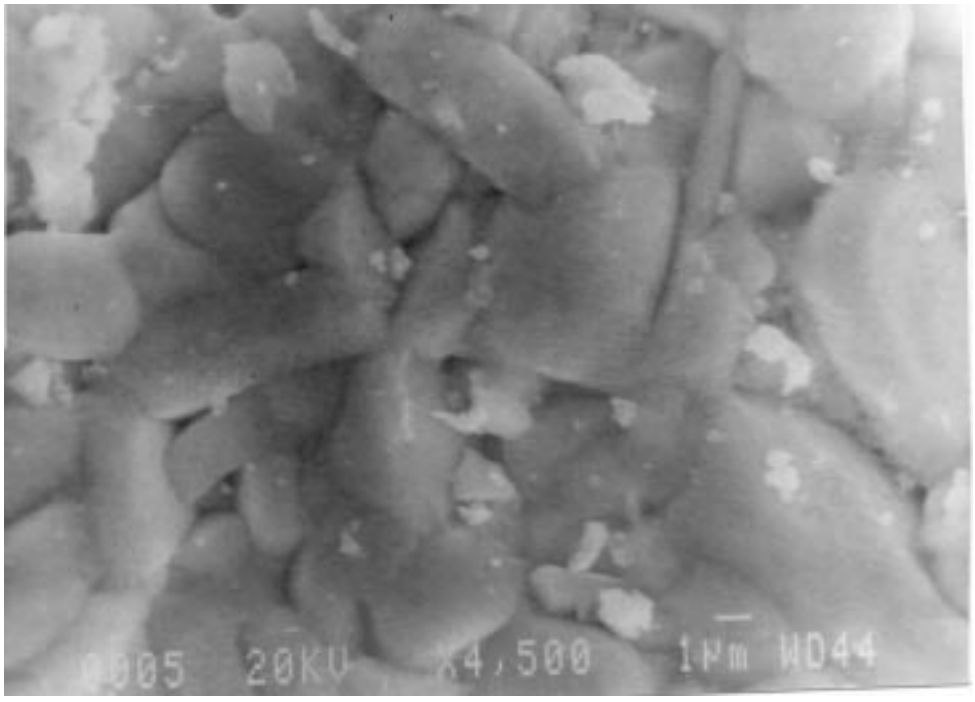

(c) x = 0.3, y = 0.6 @ 5K magnification

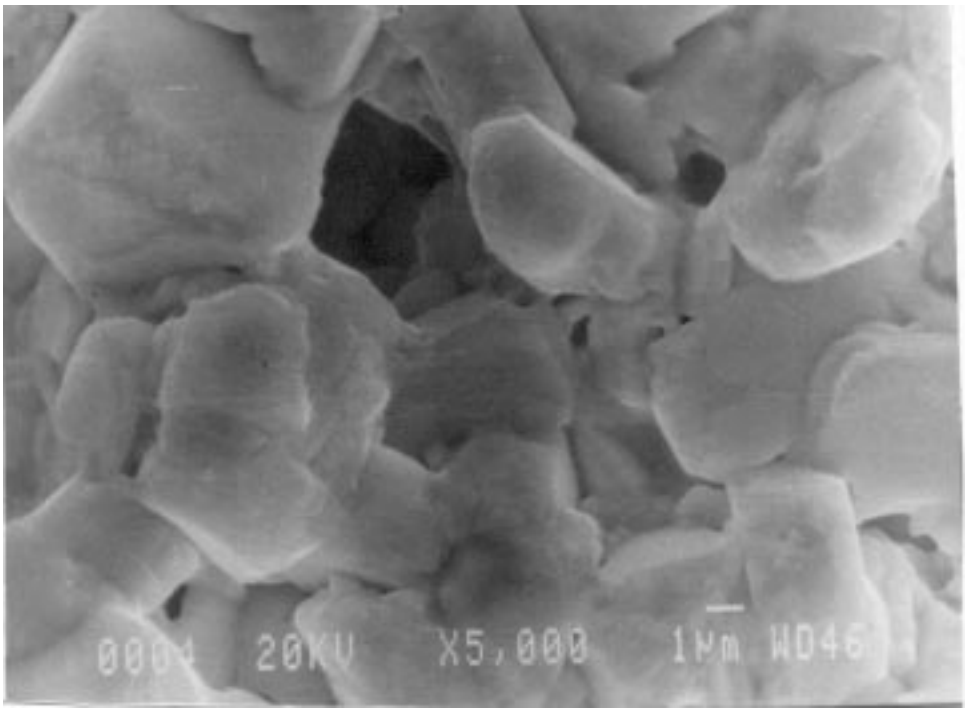

(d) x = 0.4, y = 0.8 @5k magnification

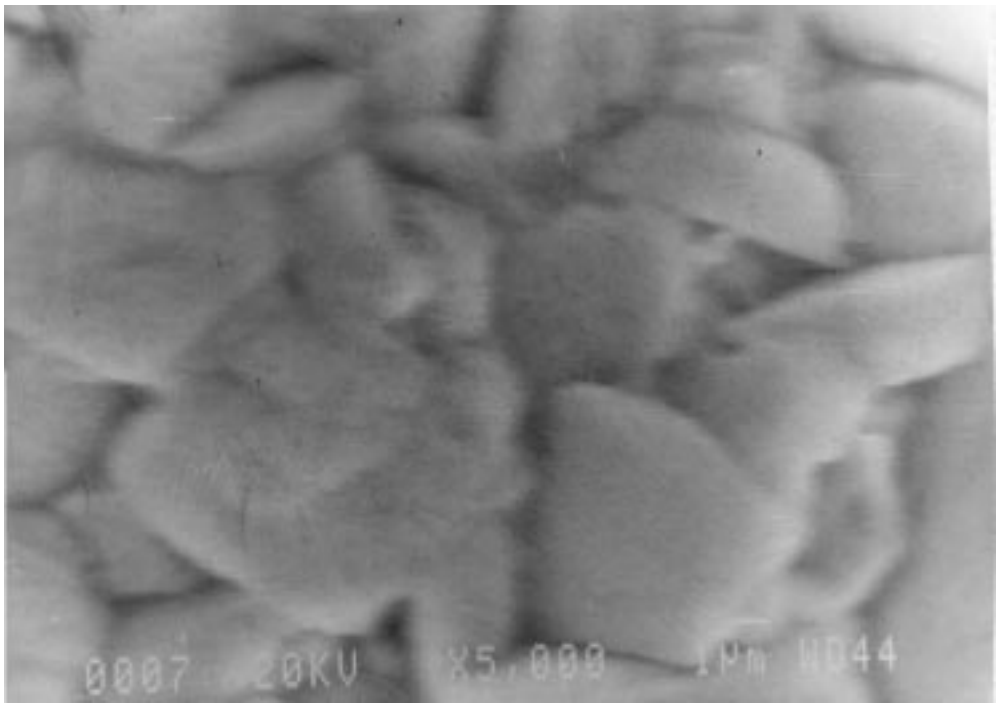

(e) x = 0.5, y = 1.0 @ 10 k magnification

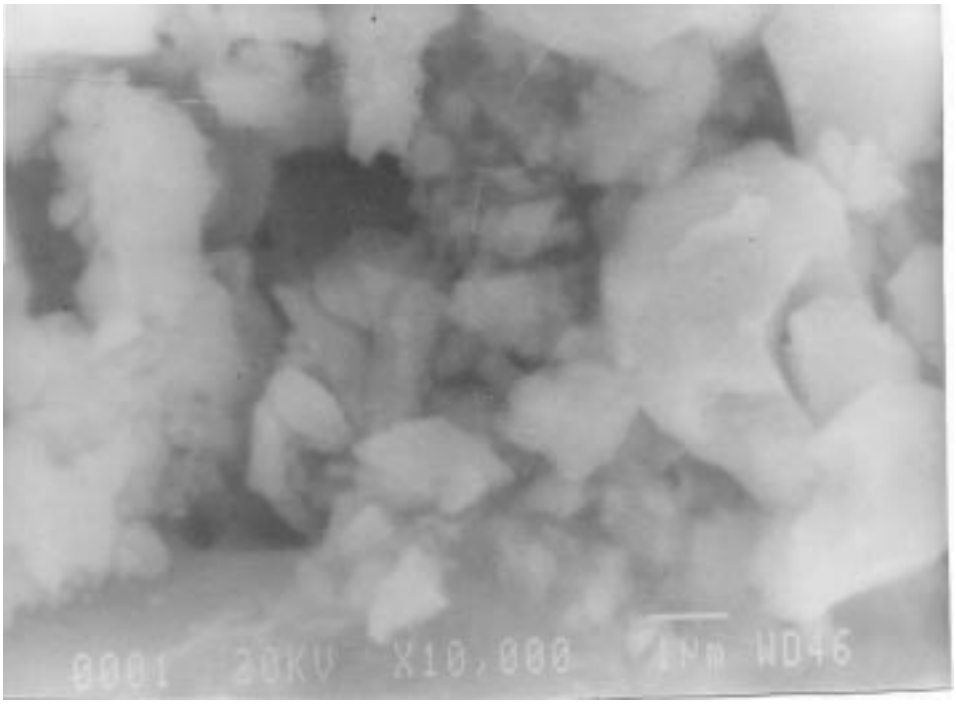

(f) x = 0.5, y = 1.0 @ 17 k magnification

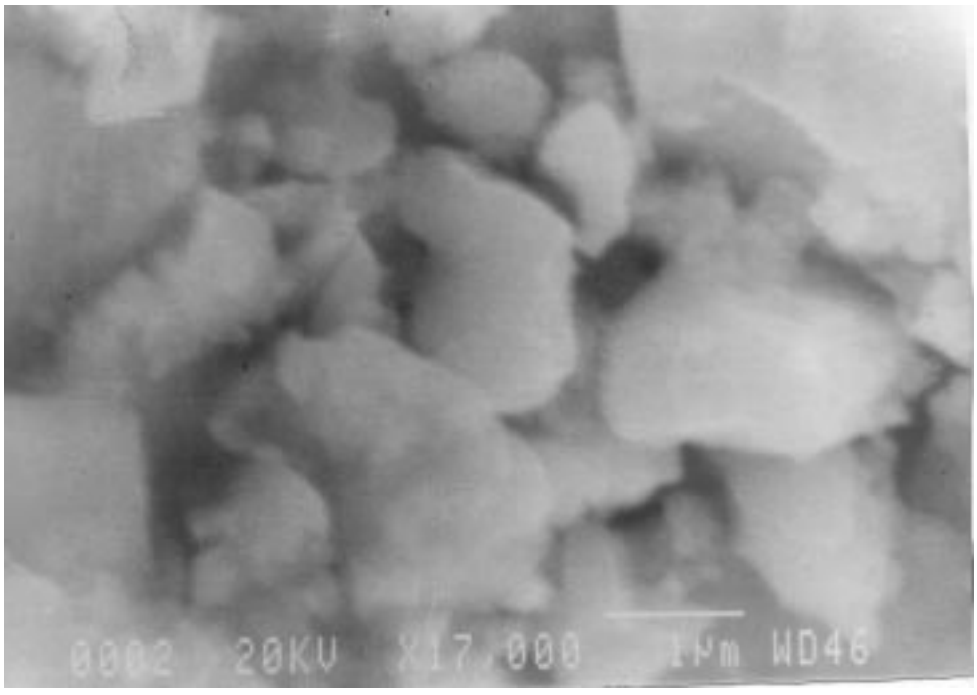

Figure 4.6 (a – f): SEM Images for $La_{2-x}Dy_xCa_yBa_2Cu_{4+y}O_z$ samples

4.1.2 In thin film form

The thin films of La-2125 ($La_{1.5}Dy_{0.5}Ca_1Ba_2Cu_5O_z$) samples were deposited using PLD technique by varying different deposition parameters. Table 4.6 lists the various parameters varied during the deposition and their results.

Table 4.6 Variation in deposition parameters used for La-2125 thin films

Parameters	*A*	*B*	*C*	*D*	*E*
Target	$La_{1.5}Dy_{0.5}Ca_1Ba_2Cu_5O_z$ single phase tetragonal superconductor				
Substrate	$LaAlO_3$ single crystal (1 0 0)				
T_s	800^0C				
D_{ts}	50 mm				
Laser used	248 nm KrF exicmer laser				
Frequency of Laser	10 Hz				
Laser Energy	~ 2 J/cm^2	~ 2 J/cm^2	~2 J/cm^2	~1.316 J/cm^2	~1.316 J/cm^2
O_p	100 mTorr	300 mTorr	250 - 300 mTorr	300 mTorr	500 mTorr
Annealing	Yes for 2hrs at 5000C before cooling to room temp. (RT) in oxygen atmosphere.	Yes for 2 hrs at 5000C before cooling to RT in oxygen atmosphere.	Cooled in oxygen at O_p	Cooled in oxygen at atmospheric pressure	Cooled in oxygen at atmospheric pressure
T_c	Non Superconductor	Metallic behavior	~ 54 K	~ 62 K	~ 62 K

All the films were deposited on the $LaAlO_3$ (LAO) single crystal (1 0 0) substrates. The choice of substrate also plays a vital role in the deposition of the thin films. Due to the lattice matching ('a' and 'b' parameters) of LAO substrates with the La-2125 unit cell, c-axis oriented thin films were produced. Also, various crucial deposition parameters, such as oxygen partial pressure, target -to- substrate distance (D_{ts}) were varied to see the effect of these parameters on the quality of thin films. The films A and B (Table 4.6) deposited at high energy but low oxygen partial pressure, keeping other parameters like D_{ts} etc constant, resulted in non-superconducting behavior. Film C was then annealed in oxygen after deposition, which exhibited superconductivity. But the maximum T_c ~ 62K, was observed in the thin films deposited at ~ 1.316 J/cm^2 and high oxygen partial pressure of 300mTorr to 500mTorr (Films D and E respectively). The structural studies and transport measurements were performed for the thin film exhibiting maximum T_c.

(a) ***X-ray Diffraction***: The thin films of $La_{1.5}Dy_{0.5}Ca_1Ba_2Cu_5O_z$ composition were deposited by using Pulsed laser deposition (PLD) technique at different conditions in order to optimize the deposition conditions for La-2125 type mixed oxide superconductors. The XRD measurements were taken on these thin films in order to verify the epitaxial growth. Figure 4.7 shows the typical XRD plot of $La_{1.5}Dy_{0.5}Ca_1Ba_2Cu_5O_z$ film deposited at the substrate temperature of 800 ^{0}C, D_{ts} (target to substrate distance) of 5.1 cm and oxygen partial pressure (inside the deposition chamber during ablation) of 500 mTorr.

Figure 4.7 also shows the LAO substrate peaks. With the improvement of the deposition conditions, the epitaxy of the film also improved. The thin film yielding

the maximum T_c achieved so far (~ 62K), showed epitaxial growth, which is shown in the figure below.

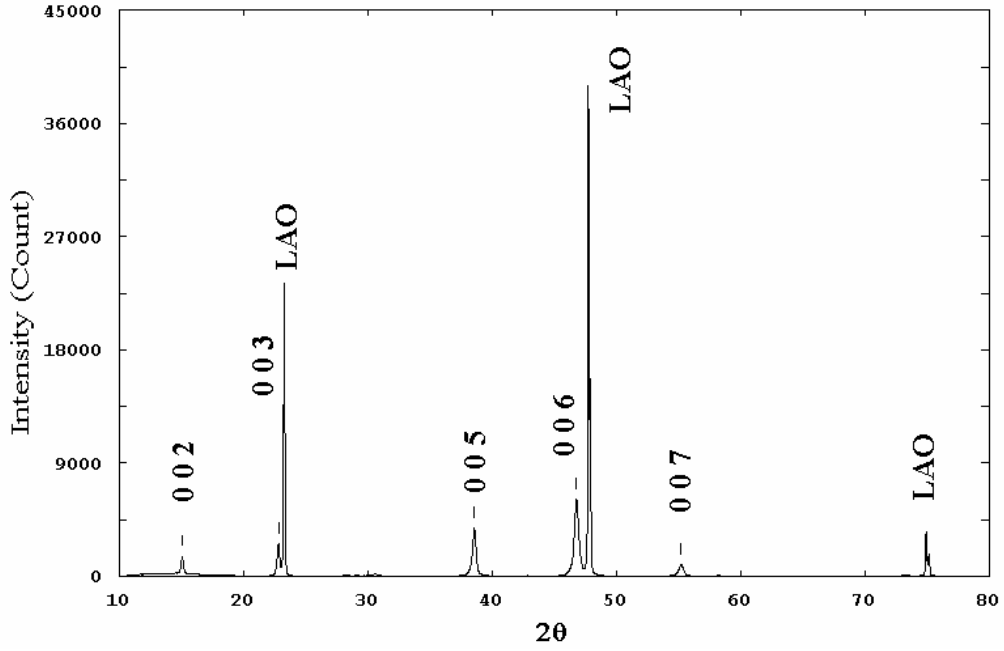

Figure 4.7 The typical XRD plot of $La_{1.5}Dy_{0.5}Ca_1Ba_2Cu_5O_z$ thin film on LAO substrate

(b) ***Atomic Force Microscopy***: In order to study the surface morphology of the thin films and estimation of grain size, Atomic Force Microscopic (AFM) studies were carried out on the thin films of $La_{1.5}Dy_{0.5}Ca_1Ba_2Cu_5O_z$ (La-2125) sample using JEOL contact mode AFM, at TIFR, Mumbai. Figures 4.8 (a & b) shows the AFM pictures of the LaDy-2125 superconductors, deposited at 800^0C (substrate temperature), D_{ts} = 5.1 cm and O_p = 500 mTorr. These films are deposited on LAO ($LaAlO_3$) substrate and has $T_c^{R=0}$ ~ 62K. The AFM pictures show that, the surface grains are having uniform shape and distribution with good packing pattern. The average grain size of the film is ~ 1800 Å.

(a)

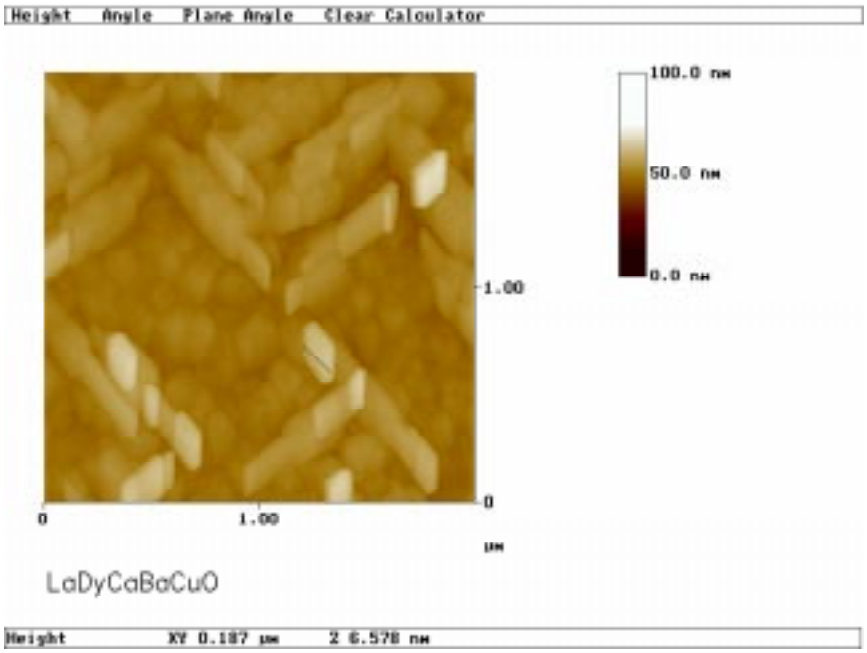

(b)

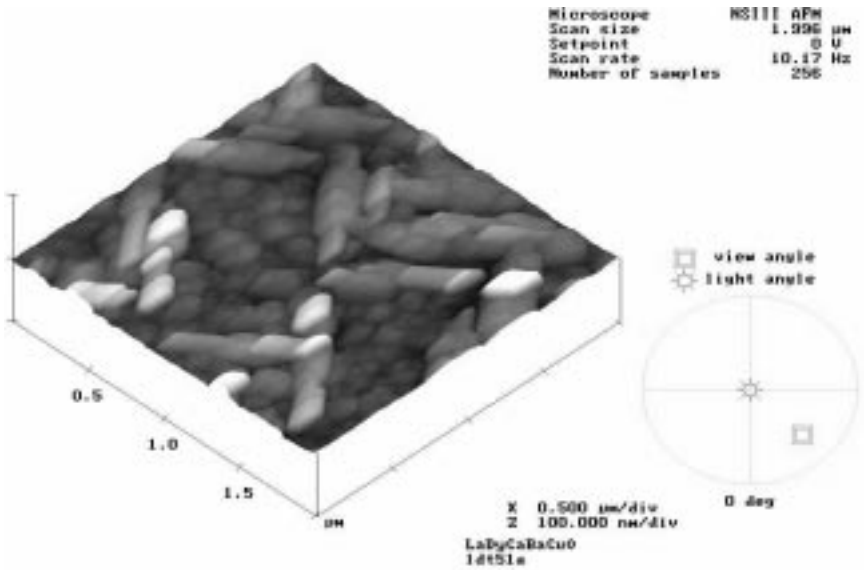

Figure 4.8 (a & b) ***AFM pictures (normal and surface) of LaDy-2125 thin film***

4.2 TRANSPORT MEASUREMENTS

(a) ***Resistivity measurements on bulk samples***: The resistivity measurements were performed on all the bulk samples using the standard four-probe method for determining the transition temperatures. Figure 4.9 shows the normalized resistance versus temperature plots for all the bulk samples in LaDyCaBCO series and the Table 4.7 lists the values of $T_c^{R=0}$.

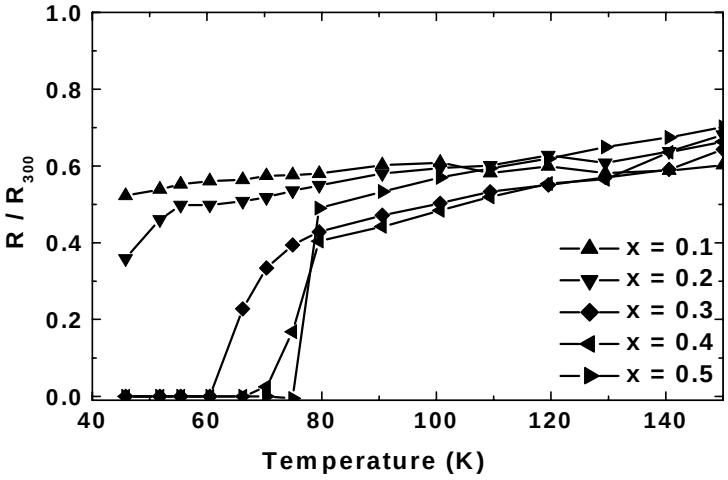

Figure 4.9 Normalized resistance versus temperature plot for LaDyCaBCO system

It is evident from the above figure that, with the increasing Ca concentration, the superconductivity is induced into the system from a non-superconducting sample (x = 0.1, y = 0.2) to a sample with maximum T_c (x = 0.5, y = 1.0). Also, the metallic nature of the sample improves with increasing dopant concentration.

Table 4.7 Values of T_c (R=0 and χ), oxygen content and hole concentration

Ca concentration	Transition temperature		Oxygen content (in 123 & 2125)		Hole concentration	
(x, y)	$T_c^{R=0}$ (K)	$T_c^{M(ON)}$	z'	z	p	p_{sh}
(0.1,0.2)	< 20	~ 25	6.90 (2)	9.66 (2)	0.266 (2)	0.200 (2)
(0.2,0.4)	< 30	-	6.95 (2)	10.19 (2)	0.300 (2)	0.225 (2)
(0.3,0.6)	66 (1)	63 (1)	6.96 (2)	10.68 (2)	0.306 (2)	0.230 (2)
(0.4,0.8)	71 (1)	-	6.96 (2)	11.14 (2)	0.309 (2)	0.232 (2)
(0.5,1.0)	75 (1)	73 (1)	6.97 (2)	11.61 (2)	0.313 (2)	0.235 (2)

(b) ***Resistivity measurements on thin films***: In order to optimise the deposition conditions for the La-2125 thin films, several parameters were varied. As a result of these changes, maximum T_c was observed in the film (Film E in Figure 4.10) deposited at 800^0C substrate temperature and 500 mTorr oxygen partial pressure. Initially the deposition conditions of RE-123 were used which were subsequently modified for the deposition of La-2125 thin films. Superconductivity is observed in films C & D synthesized in the same oxygen partial pressure with film D cooled in oxygen at atmospheric pressure. Film E deposited at higher oxygen pressure showed sharp resistive transition with less resistance. These findings clearly show that, oxygen partial pressure plays an important role in inducing superconducting property in this system. Table 4.6 gives the values of transition temperatures for all the films synthesized using varying deposition conditions.

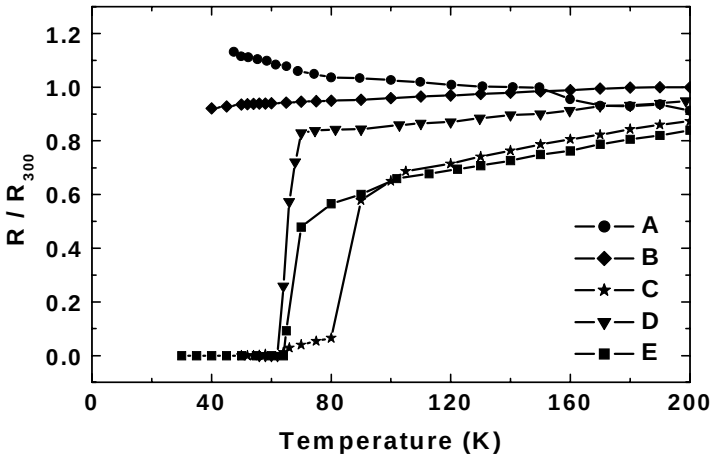

Figure 4.10 Normalized resistance versus temperature plot for LaDy-2125 thin film

4.3 MAGNETIC MEASUREMENTS

4.3.1 On bulk samples

(a) ***D.C. Susceptibility***: The d.c. susceptibility measurements were performed on few selected samples of LaDyCaBCO system to verify the transition temperatures obtained from resistive method.

It is clear from Figure 4.11, that with increase in Ca concentration along with Dy in the LaDyCaBCO system, T_c increases up to maximum value of ~ 75K. The values of T_c obtained from both electrical (R-T) and magnetic methods (M-T) are in good agreement (Fig s. 4.9 & 4.11). The susceptibility measurements were taken on the Oxford make VSM at TIFR (Mumbai) in the temperature range of 10 – 100 K at a field of 10 Oe. Table 4.7 lists the values of transition temperatures obtained from d.c. susceptibility measurements.

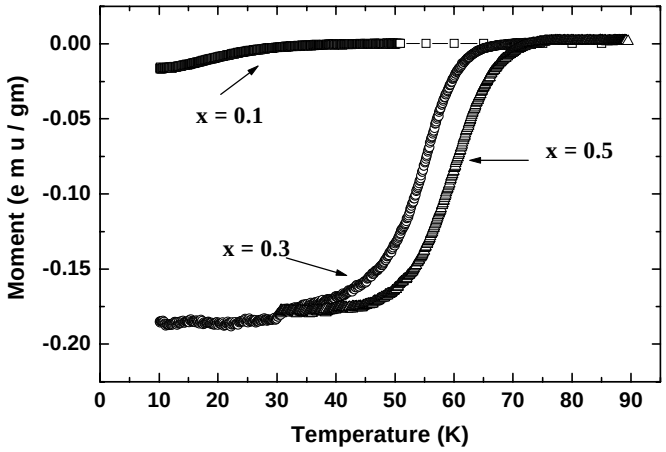

Figure 4.11 Magnetic Moment versus temperature plot for LaDyCaBCO system

(b) ***D.C. Magnetization***: The D. C. Magnetization measurements were performed on the bulk La-2125 ($La_{1.5}Dy_{0.5}Ca_1Ba_2Cu_5O_z$) for the determination of magnetic current density (J_c). Figure 4.12 shows the M-H (hysteresis) plots for the La-2125 sample obtained at 20 K, 50 K and 85 K in an applied field up to 10 k Oe.

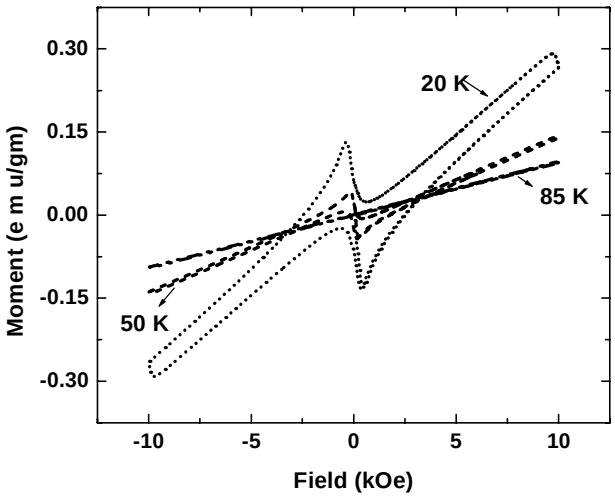

Figure 4.12 The hysteresis plot for La-2125 sample at different temperatures

The values of magnetic J_c of La-Dy-2125 sample at 20 K and 50 K have been determined using Bean's critical state model [14, 15] according to

$$J_c = \left(\frac{30\Delta M}{D} * \rho \right) (\text{A/cm}^2) \quad \ldots (5)$$

where, J_c = current density in A/cm^2

ΔM = width of loop

D = average grain size (Å)

ρ = X-ray density (in gm / cm^3)

The values of current density at various applied fields have been tabulated in Table 4.8.

Table 4.8 Values of current densities at various temperatures and fields

Sample	Temperature (K)	Field H (k Oe)	J_c (X 10^6 A/cm^2)
$La_{1.5}Dy_{0.5}Ca_1Ba_2Cu_5O_z$	20	0.5063	2.3218
		0.6330	2.0015
		1.7721	1.1208
		2.6582	0.9607
		5.1898	0.7218
		6.7721	0.6405
		9.0506	0.5605
	50	0.4430	0.4403
		0.9493	0.2802
		1.1392	0.2401
		1.4556	0.2001
		4.5569	0.1200
		8.2278	0.0800

4.3.2 On thin films

(a) ***D.C. Susceptibility***: The D.C. Susceptibility measurements were taken on the thin film (Film E – Table 4.5) with maximum $T_c^{R=0}$ in order to confirm the transition temperature for the film and also to study its diamagnetic behavior. The VSM (Oxford instruments) facility at TIFR Mumbai has been used to measure the M-T plot for the thin film.

The value of transition temperature obtained from d.c. susceptibility curve of La-Dy-2125 thin film (Figure 4.13) is in good agreement with the value obtained from similar measurements on bulk sample. This shows the good quality of the thin film.

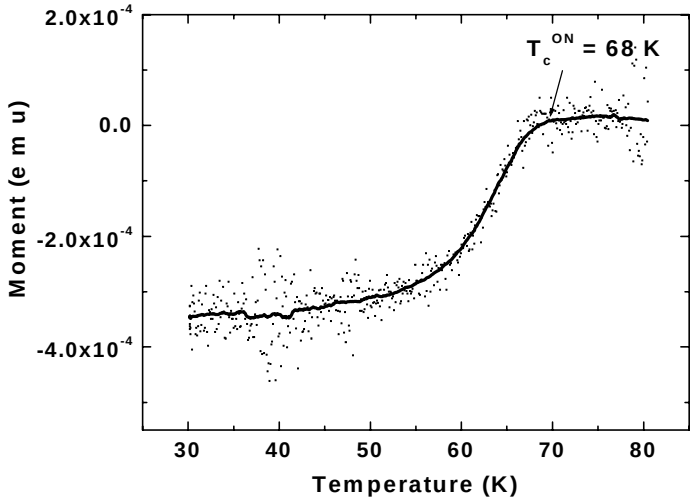

Figure 4.13 M-T plot for $La_{1.5}Dy_{0.5}Ca_1Ba_2Cu_5O_z$ thin film

(b) ***D.C. Magnetization***: Similar to the studies on bulk sample, the thin film of LaDyCaBCO system (Film E), has been studied for its magnetic behavior at different temperatures and applied fields. The magnetic hysteresis loop for the Film E has been

recorded using the VSM magnetometer at TIFR, Mumbai at 20 K and 85 K up to 10 k Oe applied field.

The magnetization measurements recorded at 20 K (below T_c) and at 85 K (above T_c) show totally different behaviors. Figure 4.14 depicts the M-H loop of La-Dy-2125 thin film recorded at 20 K showing a large hysteresis effect. M-H loop of the sample taken at 85 K has not been shown as it shows paramagnetic behavior with large fluctuations in the data.

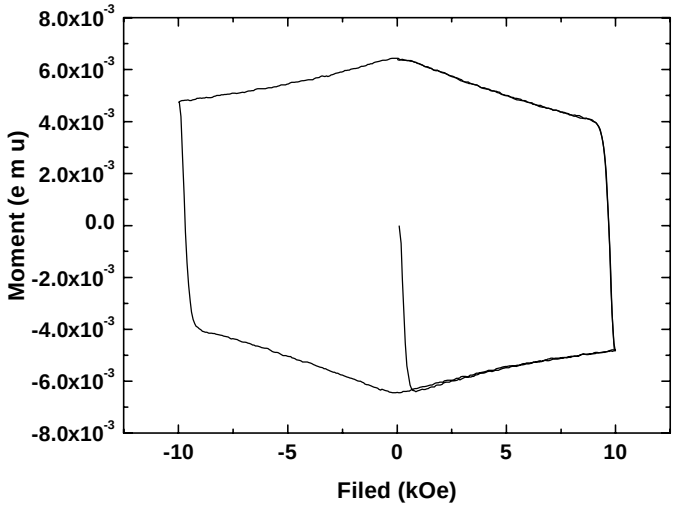

Figure 4.14 M-H loop for $La_{1.5}Dy_{0.5}Ca_1Ba_2Cu_5O_z$ thin film at 20 K

The current densities at different applied fields were calculated using the Bean's critical state model, using the relation for thin film samples [16]

$$J_c = \frac{30\Delta M}{b\left[1-\frac{b}{3a}\right]} \qquad \ldots (6)$$

where, ΔM = width of the hysterisis loop at same field,

a & b are the dimensions of the thin film (Å)

The values of the current densities calculated at 20 K, using the above formula for the $La_{1.5}Dy_{0.5}Ca_1Ba_2Cu_5O_z$ thin film has been tabulated in the Table 4.9.

Table 4.9 Current density values for LaDyCaBCO thin film

Sample	Temperature (K)	Field H (k Oe)	J_c (X 10^6 A/cm^2)
$La_{1.5}Dy_{0.5}Ca_1Ba_2Cu_5O_z$ (Thin film)	20	1.23377	2.6564
		2.72727	2.4467
		4.48052	2.2835
		5.12987	2.2136
		5.77922	2.1204
		7.01299	2.0272
		7.66234	1.9806

4.4 IODOMETRIC TITRATION

Oxygen content in the LaDyCaBCO samples was determined by the Iodometric double titration method. Small weights (~ 30 – 40 mg) of the finely powdered samples were taken for titration against the reducing agents. The detailed procedure explained in Chapter 2 (Section 2.5.1) and Chapter 3 (Section 3.5.1) has been followed in calculating the oxygen content and hole concentration. Table 4.7 lists the values of oxygen content and hole concentration calculated from Iodometric titration results.

The oxygen content has been calculated by using the relation:

$$z = 3.5(2+p) + 5.5 \quad \ldots (7)$$

The following relation has been used to calculate the value of oxygen content per unit formula in RE-123 form:

$$z' = [z^* 3 / (\text{Cu content per unit formula of La-2125 unit cell})]$$

The values of oxygen content have been used for calculating the hole concentration per unit formula using Tokura's model [17].

4.5 DISCUSSION

Results of the structural, electrical and magnetic property measurements on the bulk samples of $La_{2-x}Dy_xCa_yBa_2Cu_{4+y}O_z$ (LaDyCaBCO); x = 0.1-0.5, y = 2x system have been discussed here in the light of effect of simultaneous increase in Dy and Ca concentration in non-superconducting tetragonal $La_2Ba_2Cu_4O_z$ system.

Figure 4.15 shows the variation in unit cell parameters and unit cell volume with the increase in Dy concentration (x).

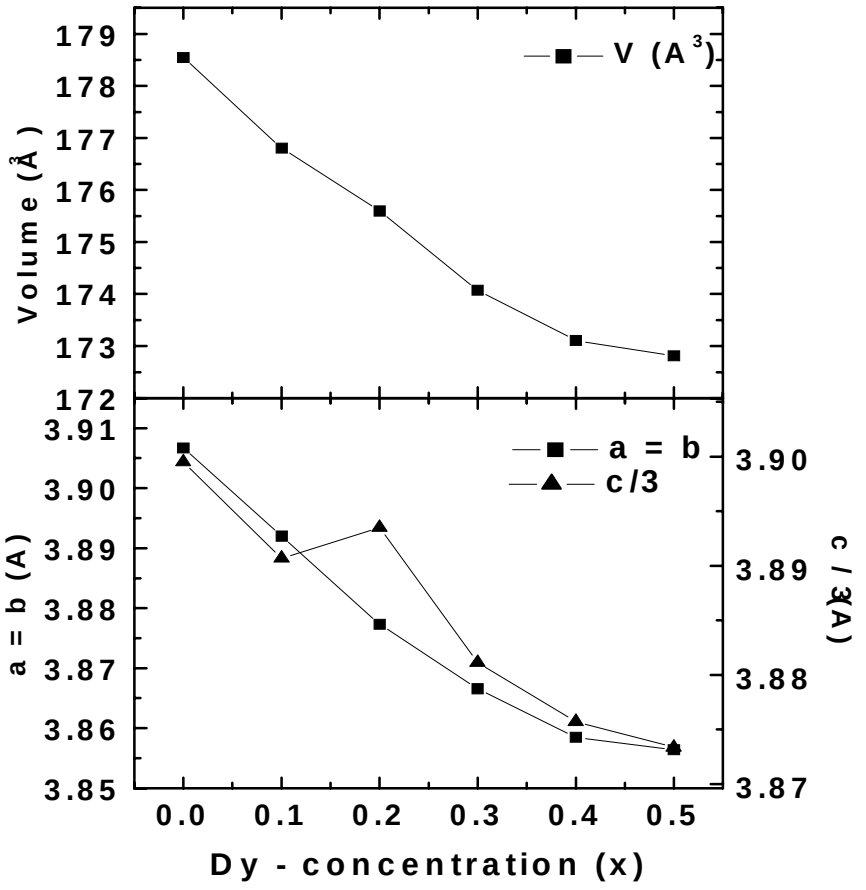

Figure 4.15 ***Variation in unit cell parameters and volume with increasing Dy concentration (x)***

The figure clearly shows that, the replacement of La^{3+} by smaller Dy^{3+} and Ca^{2+} ions is responsible for the decrease in unit cell parameters and unit cell volume. Also, the density of the samples increases with increasing Dy-Ca concentration (Table 4.1). Figure 4.16 shows the variation in T_c for LaDyCaBCO samples with increasing Dy (x) and Ca (y = 2x) concentration. It can be seen that, T_c increases with increasing dopant concentration with a maximum T_c ~ 75 K for x = 0.5 i.e. y = 1.0, concentration.

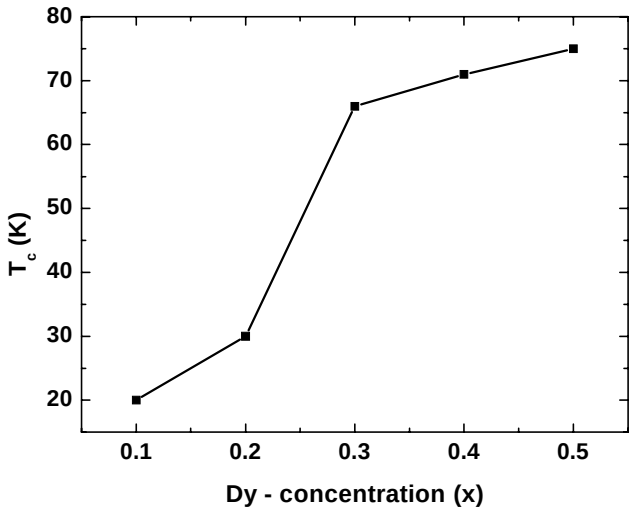

Figure 4.16 Increase in T_c with increase in Dy (x) and Ca (y = 2x) concentrations

This behavior in T_c increase due to Dy-Ca doping can be explained as follows: Rietveld analysis of the neutron diffraction (ND) data on bulk LaDyCaBCO samples reveal that, with increasing Dy-Ca concentration the occupancy of Ca-ions at La-site increases with concomitant displacement of La ions at Ba-site (Table 4.3). This behavior can be clearly seen in Figures 4.17 and 4.18.

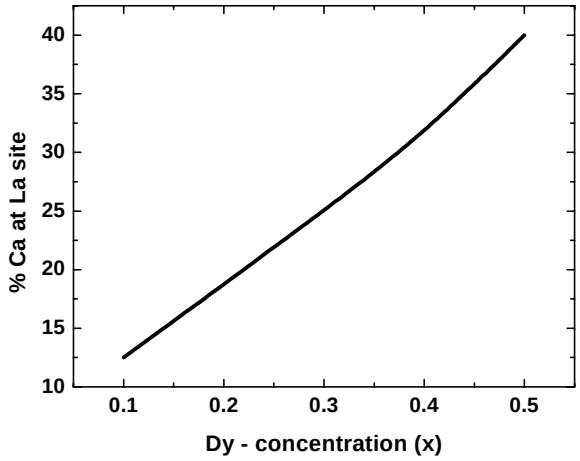

Figure 4.17 Occupancy of Ca at La site (in %) with increasing Dy (x) concentration

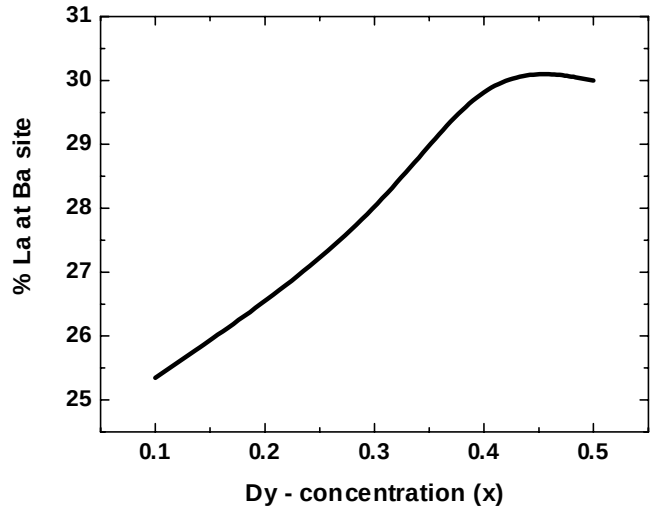

Figure 4.18 Occupancy of La at Ba site (in %) with increasing Dy (x) concentration

It has been observed that, increasing Ca concentration results in an increase in Ca-occupancy at La site (Figure 4.17) along with some fraction of Ca^{2+} occupying Ba^{2+} site (Figure 4.19).

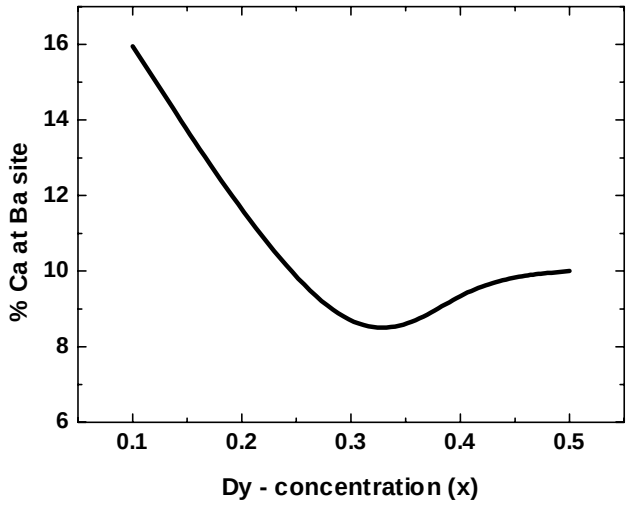

Figure 4.19 Occupancy of Ca at Ba site (in %) with increasing Dy (x) concentration

The results of the comprehensive Rietveld analysis of the ND data for knowing the % occupancy of Ca ions at La and Ba site in Dy-Ca doped LaDyCaBCO samples are displayed in Figure 4.20, which shows the overall variation in Ca occupancy at La and Ba sites with increasing dopant concentration.

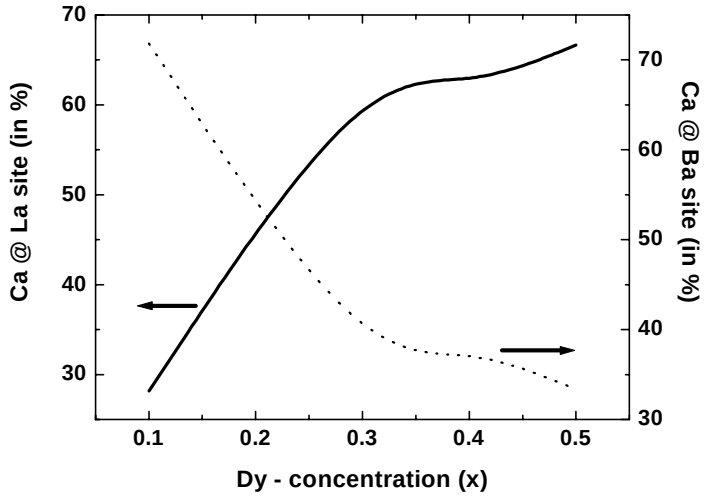

Figure 4.20 Overall occupancy of Ca (in %) at La and Ba sites

For Dy (x = 0.5), i.e. Ca (y = 1.0) sample, with the composition $La_{1.5}Dy_{0.5}Ca_1Ba_2Cu_{4+y}O_z$, which when normalized to RE-123 is $La_{0.9}Dy_{0.3}Ca_{0.6}Ba_{1.2}Cu_3O_z$ or $(La_{0.3}Dy_{0.3}Ca_{0.4})(Ba_{1.2}Ca_{0.2}La_{0.6})Cu_3O_z$ [La-123 stochiometry], it has been observed that out of overall Ca occupancy of 0.6, Ca occupies 0.4 (i.e., ~ 66 %) at La site which is responsible for providing the necessary holes for superconductivity in the sample.

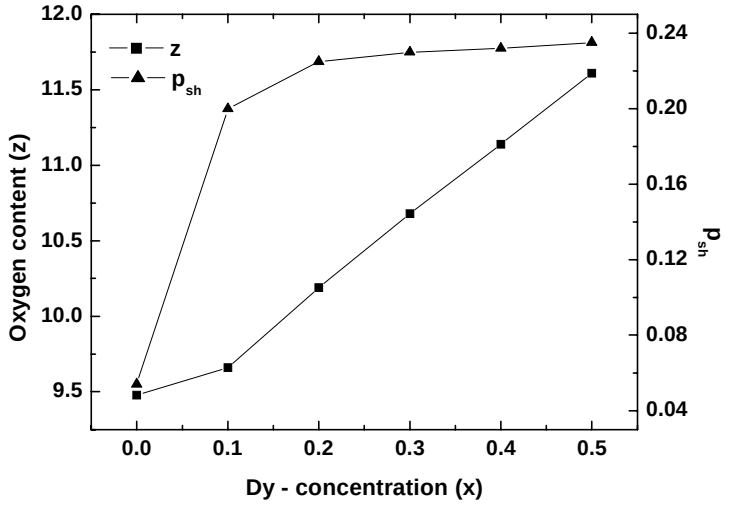

Figure 4.21 Plot of oxygen content (z) and hole concentration vs. Dy concentration

The results of the Rietveld analysis suggests that, Ca doping increases the hole concentration, thereby increasing T_c. This has been supported by the oxygen content determination studies using Iodometric titration. Figure 4.21 shows the dependence of oxygen content (z) and hole concentration in CuO_2 (p_{sh}) sheets, on the doping concentration (x). Increasing the dopant content increases the (z) and hence p_{sh} values, which clearly shows, that the concentration of holes in CuO_2 sheets is responsible for the occurrence of superconductivity in La-2125 system. This observation has been understood by normalizing the La-2125 stochiometry to, well understood La-123

system. Based on these studies, an attempt is made to propose a crystallographic unit cell model of La-2125 system, which is shown in Figure 4.5, developed on the basis of unit cell of La-123 structure [Figure 4.4].

The structural and transport studies on La-2125 system have revealed that, Ca ions plays an important role along with Cu ions in 'turning on' of superconductivity in this system. A large number of studies have been reported on the current density measurements and it's dependence on various dopants, applied field and temperature in RE-123 type of superconducting systems [18, 19]. These studies in bulk and thin film forms of the RE-123 samples help to explore the possibility of applications of RE-123 materials in various devices [20, 21].

Keeping in mind the importance of current density studies and similarity of structural and transport properties of La-2125 & RE-123 system, an effort is made to determine the current density (J_c) of La-Dy-2125 samples using magnetic measurement techniques. La-Dy-2125 sample has been selected as it exhibits maximum $T_c \sim 75$ K and stable tetragonal structure [22].

Figure 4.22 shows the variation of current density with increasing applied magnetic field at various temperatures for La-Dy-2125 sample. The values of J_c are in the range of $0.6 \times 10^6 - 2.4 \times 10^6$ A/cm^2 and $1 \times 10^5 - 4 \times 10^5$ A/cm^2 measured at 20 K and 50 K respectively. This clearly shows that within the temperature difference of 30 K, the current density decreases by a factor of six.

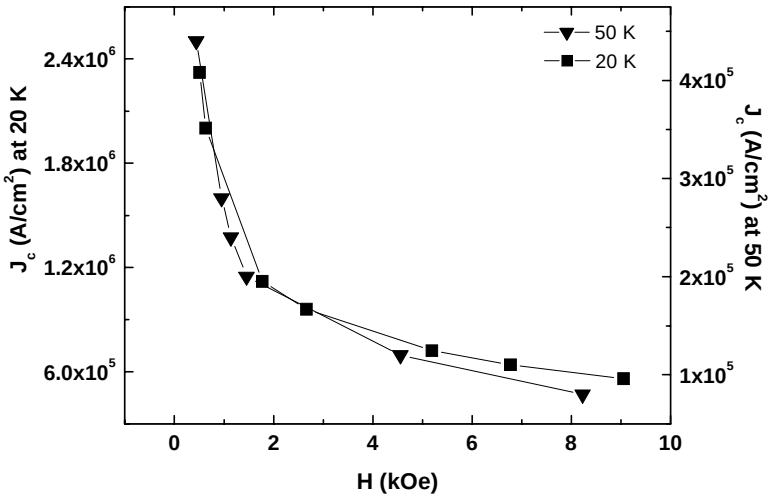

Figure 4.22 J_c vs. H plot for $La_{1.5}Dy_{0.5}Ca_1Ba_2Cu_5O_z$ bulk sample.

Figure 4.23 shows the logarithmic (natural) values of J_c and H for the above plot.

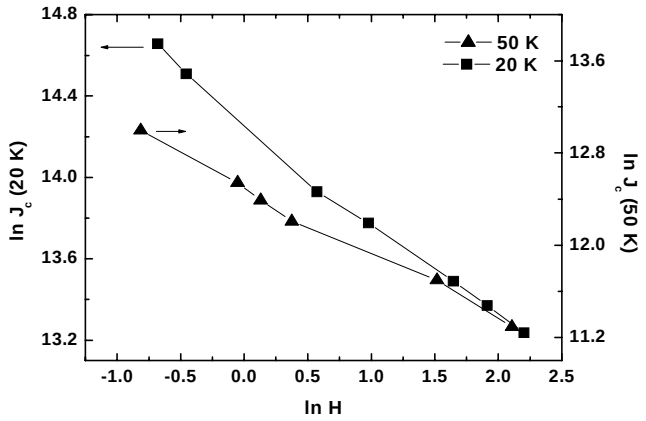

Figure 4.23 ln J_c vs. ln H for LaDy-2125 bulk sample

The slopes of the above plots (n), also called the gradient of plots (-n), which are 0.4860 and 0.5658 at 20 K and 50 K respectively. The values are in good agreement with the flux creep model [23], which relates the current density to the applied field according to the relation [24]

$$\mathbf{J_c \propto H^{-n}\ (n = 0.5)} \qquad \ldots (8)$$

In addition to the J_c measurement in bulk La-Dy-2125 sample, magnetic J_c has been also determined in the thin film of La-Dy-2125 sample synthesized using PLD technique. For the determination of magnetic J_c, the equation (5) has been modified to equation (6) by taking into consideration the dimensions of the thin films.

Figure 4.24 shows the decrease in current density (J_c) for the La-Dy-2125 thin film with increasing applied field (H).

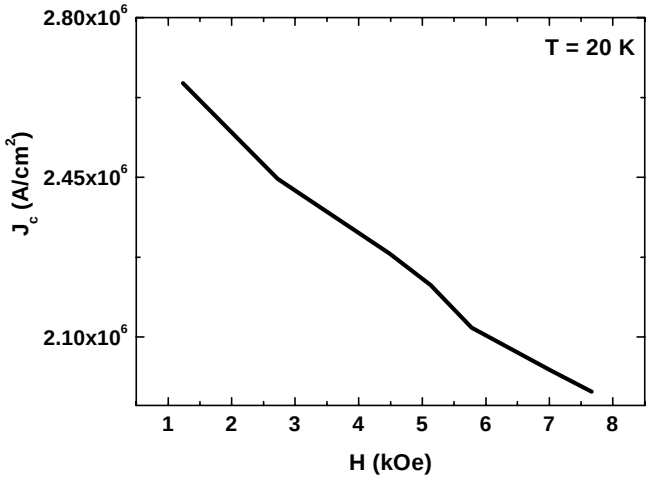

Figure 4.24 J_c versus H plot for $La_{1.5}Dy_{0.5}Ca_1Ba_2Cu_5O_z$ thin film

It can be seen that, the range of J_c of thin films of La-Dy-2125 is 2.1 X 10^6 – 2.6 X 10^6 (A/cm^2), which is higher than the range of J_c variation of 6 X 10^5 - 2.4 X10^6 (A/cm^2) for bulk La-Dy-2125 sample at 20 K.

The Figure 4.25 shows the logarithmic (natural) values of J_c and H for La-Dy-2125 thin film at 20K. The slope (n) of the plot is 0.1589, which is a clear deviation from the flux creep model observed in the bulk sample with the same composition.

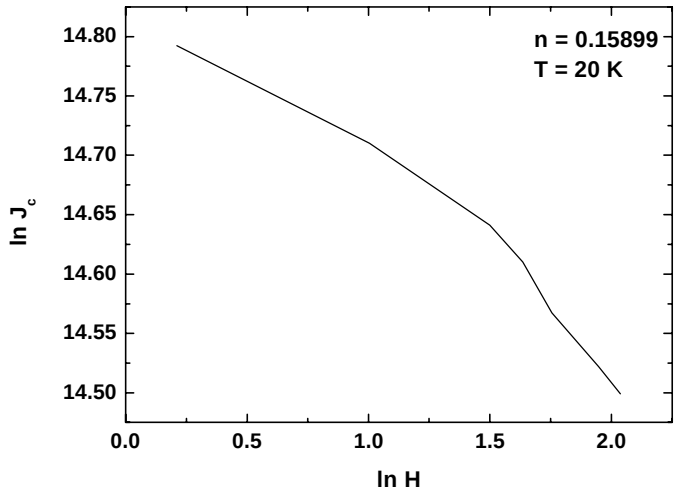

Figure 4.25 ln J_c vs. ln H plot for LaDy-2125 thin film at 20K

Since it is very difficult to estimate exact dimensions and thickness of thin films, the formula used to obtain J_c is an estimate. Further, thin films are supposed to be a replica of single crystal in which uniform grain size and homogeneity are maintained. Therefore, it is expected that film will not obey flux creep model. The present findings agree with the above assertion that thin films do not obey flux creep model that is why the slope found for thin films is about 0.16, where as for bulk it is around 0.5.

CONCLUSIONS

Our studies on the structural, transport and magnetic measurements on the bulk and thin film samples of $La_{2-x}Dy_xCa_yBa_2Cu_{4+y}O_z$; x = 0.1 – 0.5, y = 2x, samples shows the following salient features

- Addition of equal amounts of CaO and CuO, along with rare earth Dy, in the non-superconducting tetragonal $La_2Ba_2Cu_4O_z$ system, results into the formation of a superconducting tetragonal $La_{1.5}Dy_{0.5}Ca_1Ba_2Cu_5O_z$ (La-2125) phase with a maximum T_c of ~ 75 K with stable oxygen independent behavior.
- There exists a direct relationship between T_c and hole concentration in conducting CuO_2 planes with the Ca concentration.
- The thin films of La-Dy-2125 system exhibits single phase epitaxial behavior with an average grain size of ~ 1800 Å and a well defined surface morphology.
- The detailed structural investigations using neutron diffraction (ND) studies at room temperature shows that, with increasing Ca-concentration the occupancy of Ca ions at La site increases with concomitant displacement of La onto Ba site. The increased Ca occupancy provides the necessary holes for conduction in CuO_2 planes and Ca substitution helps in 'turning on' of superconductivity in the system.
- Results of the current density measurements on the bulk La-Dy-2125 samples with maximum T_c ~ 75K suggests that, the decrease in J_c (current density) with increasing field at different temperatures obeys the flux creep model. The

study of field dependence of J_c for La-Dy-2125 thin film shows that, there is a deviation from flux creep model which may be attributed to the uniform grain size and homogeneity in the films.

REFERENCES

[1] S. Englesberg, Physica C **176** 451 (1991)

[2] A. Maeda, T. Noda, H. Matsumoto, T. Wada, M. Izumi, T. Yabe, K. Uchinokura and S. Tanaka, J. Appl. Phys. **64 (8)** 4095 (1998)

[3] J. M. S. Skakle and A. R. West, Physica C **227** 336 (1994)

[4] D. S. Wu, Y. F. Wang, H. C. I Kao and C. M. Wang, Physica C **212** 32 (1993)

[5] B. Raveau, J. Solid State Chem. **3** 151 (1981)

[6] H. Rajagopal, A. Sequeira, R. Alfred Gunasekaran, I. K. Gopalkrishnan, J. V. Yakhmi and R. M. Iyer, Physica B **174** 372 (1994)

[7] N. Nguyen, J. Choisnet, M. Herview and B. Raveau J. Solid State Chem **39** 120 (1981)

[8] C. Chaubaud, Y. Direktovitch and I. Gertner, Physica C **261** 33 (1996)

[9] J. Santiso, A. Figueras, A. Moya and F. Baudenbacher Physica C **351** 155 (2001)

[10] D. Goldschmidt, G. M. Reisner, Y. Direktovitch, A. Knizhnik, E. Gartstein, G. Kimmel and Y. Eckstein, Phys. Rev. B **48** 532 (1993)

[11] R. J. Cava, B. Batlogg, R. B. Van Dover, D. W. Murphy, S. Sunshine, T. Siegrist, J. P. Remeika, E. A. Rietman, S. Zahurak and G. P. Espinosa Phys. Rev. Lett. **58** 1670 (1987)

[12] J. D. Jorgensen, B. W. Veal, A. P. Paulikar, L J. Nowicki, G. W. Crabtree, H. Clauss and W. K. Kwok, Phys. Rev B **41** 1863 (1990)

[13] Juan Rodriguez-Carjaval, Laboratoire Leon Brillouin (CEA-CRNS) (1997)

[14] C. P. Bean, Rev. Mod. Phys. **36** 31 (1964)

[15] J. O. Willis, J. R. Cost, R. D. Brown, J. D. Thompson and D. E. Peterson
IEEE Trans. Magn. Mag. **25** 21 (1989)

[16] F. Wang
Superconduct. Sci. Technol. **14** 826 (2001)

[17] Y. Tokura, J. B. Torrance, T. C. Huang and A. I. Nazzal
Phys. Rev. B **38** 7156 (1988)

[18] R. G. Kulkarni, G. J. Baldha, G. K. Bichile, D. G. Kuberkar and
Smita Deshmukh, Appl. Phys. Lett **59** 1386 (1991)

[19] G. K. Bichile, D. G. Kuberkar, K. M. Jadhav, S. S. Shah and R. G. Kulkarni
Cryogenics **31** 833 (1991)

[20] M. R. Koblischka, M. Muralidhar, T. Higuchi, K. Waki, N. Chikumoto and
M. Murakami, Supercond. Sci. Technol. **12** 288 (1999)

[21] G. Hammert, A. Schmehl, R. R. Schulz, B. Goetz, H. Bielefeldt,
C. W. Schneider, H. Hilgenkamp and J. Mannhart, Nature **407** 162 (2000)

[22] S. Rayaprol, Krushna Mavani, D. S. Rana, C. M. Thaker, R. S. Thampi,
D.G. Kuberkar, S.K. Malik and R. G. Kulkarni
J. of Supercon. **15(3)** 211 (2002)

[23] M. Tinkham, Helvetica Physica Acta 61 443 (1988)

[24] J. Mannhart, P. Chaudhari, D. Dimos, C. C. Tsuei and T. R. McGuire
Phys. Rev. Lett. **61** 2476 (1988)

CHAPTER - V

Studies on Pr and Mo substituted La-2125 system

INTRODUCTION

Pr-123 is a non-superconductor with non-metallic nature [1-2]. But there is a marked difference in the properties of Pr-123 and Pr doped 123 systems. In Pr doped 123 systems, the increase in Pr content gradually suppresses the superconductivity [3, 4]. In order to explain this behavior of Pr-doped 123 systems, two mechanisms have been proposed which are magnetic pair breaking and /or localization of holes available for conduction in CuO_2 planes [5].

The substitutional effects of Pr existing in either Pr^{3+}, Pr^{4+} or mixed valent $Pr^{3+,\ 4+}$ at RE (rare earth) site in $RE_{1-x}Pr_xBa_2Cu_3O_z$ (RE-123) with RE = Eu, Er, Gd and Y etc have been widely studied [6 – 8]. In RE-123 systems, the superconductivity gets suppressed at about $x \geq 0.5$ either due to tetravalent Pr induced hole filling or localization of mobile holes in the conducting CuO_2 planes or by magnetic pair breaking through hybridization of Pr^{3+} ($4f^2$) and O^{2-}(2p) states of CuO_2 planes [9, 10].

Our earlier studies on the role-played by RE substitution at La-site in newly synthesized $La_{2-x}RE_xCa_yBa_2Cu_{4+y}O_z$; x = 0.0 – 0.5, y = 2x system, have shown that RE ion at La-site provide the stability to the La-2125 structure [11, 12]. Keeping in mind the role played by Pr-substitution at RE-site in RE-123 systems [3, 4] it would be interesting to study the role played by Pr – substitution at La-site in modifying the structural and superconducting properties of $La_{2-x}Pr_xCa_yBa_2Cu_{4+y}O_z$ (LaPrCaBCO) system. For this purpose La-2125 system is normalized to RE-123 and then the effect of Pr-substitution at La-site on the T_c has been studied on the basis of mechanisms relevant to RE-123 system. For this purpose a series of samples with the stochiometric composition $La_{2-x}Pr_xCa_yBa_2Cu_{4+y}O_z$, x = 0.1 – 0.5, y = 2x; (LaPrCaBCO) have been

synthesized and detailed structural study has been done by analyzing the X-ray diffraction (XRD) data by Rietveld refinement method. The XRD data was obtained at room temperature (RT) using Cu-K_α radiation of wavelength, λ = 1.5405 Å. The superconducting properties have been studied using electrical (four probe resistivity) and magnetic (d.c. susceptibility and d.c. magnetization) methods.

The substitutional studies at different crystallographic sites in RE-123 superconductor have been done by many researchers to investigate the origin and mechanism of superconductivity [13, 14]. It is reported that, the Cu-site substitution by Fe, Co, Ni, Zn, Mo etc reduces T_c and induces structural phase transitions. Interestingly, partial substitution of rare earth at La-site in La-2125 systems shows no effect on T_c similar to rare earth substituted RE-123. To date no attempt has been made to substitute metal dopant like Mo for Cu-site in La-2125 superconductor in order to understand the effect of aliovalent substitutents on structure and superconductivity of the La-2125 compounds.

One of the important properties needed to be determined for application of high-T_c superconductors is their current-carrying capacity and temperature and field dependence. For most applications, a high critical current density $J_c \sim 10^4 - 10^6$ A/cm^2 is required, often in the presence of crystalline defects that can act as pinning centers, which are necessary to sustain resistanceless currents in magnetic fields [15]. It is well established that, the superconducting behavior of 123 materials depends markedly on the changes in the effective copper valence [16]. The effective valence can be monitored by the changes in the oxygen stoichiometry or the chemical substitutions at copper and non-copper sites [17, 18]. The valency of dopant plays an important role

in monitoring the effective copper valence (the mobile carrier concentration, *p*) or the oxygen content of oxide superconductors, as superconducting behavior depends on it. Especially, cation doping [19, 20] at the Cu-site may change *p* and affect many properties accordingly. The valence state of $Mo^{4+, 6+}$ is higher than that of Cu^{2+}; such a substitution of Mo for Cu in YBCO decreases *p* and is also equivalent to the introduction of defects at Cu-sites, which act as pinning centers. Some work has been reported on the effect of Mo substitution on the superconducting properties of YBCO and REBCO [21] which prompted us to extend this interesting work onto the La-2125 system and study the effect of Mo substitution at Cu site in $La_{1.5}Nd_{0.5}Ca_1Ba_2[Cu_{1-x}Mo_x]_5O_z$ system for x = 0.00 – 0.20. Literature survey reports that, the hole filling by Mo at Cu site can be compensated by hole doping in the non-copper cation sites in RE-123 systems [22]. In order to investigate, whether this hole doping phenomenon can be possible in the presently studied system, we studied the Mo substituted system with Ca doping in the form, $La_{1.5-y}Nd_{0.5}Ca_{1+y}Ba_2[Cu_{1-x}Mo_x]_5Oz$, for x = 0.20 and y = x, 2x, 3x.

5.1 STUDIES ON LaPrCaBCO SYSTEM

5.1.1 ***X-ray Diffraction***: The X-ray diffraction measurements were performed on all the samples of LaPrCaBCO system at room temperature in the 2θ range of 20^0 - 80^0 using a Cu-K_α radiation of wavelength λ = 1.5405 Å. Figure 5.1 shows the indexed XRD patterns for the LaPrCaBCO system.

The XRD patterns were indexed and unit cell parameters were refined by using the 'PowderX' software. The values of unit cell parameters, unit cell volume and X-ray density are shown in Table 5.1.

Table 5.1 Values of unit cell parameters, volume and X-ray density

Sample (x, y)	Unit cell Parameters		Volume (V)	X-ray density (ρ)
	(a= b) Å	(c) Å	$(Å)^3$	(gm / cm^3)
(0.1, 0.2)	3.9312 (3)	11.8340 (8)	182.8903	8.8690
(0.2, 0.4)	3.8839 (3)	11.6601 (8)	175.8969	9.5576
(0.3, 0.6)	3.8783 (3)	11.6287 (8)	174.9117	9.8452
(0.4, 0.8)	3.8675 (3)	11.6074 (8)	173.6247	10.1939
(0.5, 1.0)	3.8726 (3)	11.6342 (8)	174.4797	10.4142

Detailed structural studies on the LaPrCaBCO system have been done by analyzing the XRD data by Rietveld refinement technique using FULLPROF program. During the refinement of the data, an initial model of RE-123 tetragonal structure with P 4/M M M space group (No. 123) was assumed on the lines of analysis of LaDyCaBCO system (Chapter – IV). Figs. 5.2 (a – e) shows the Rietveld fitted indexed XRD patterns for all the samples of LaPrCaBCO system. It can be seen from the figures that, the calculated XRD patterns fit very well with the observed patterns, which shows the single-phase nature and good quality of the samples.

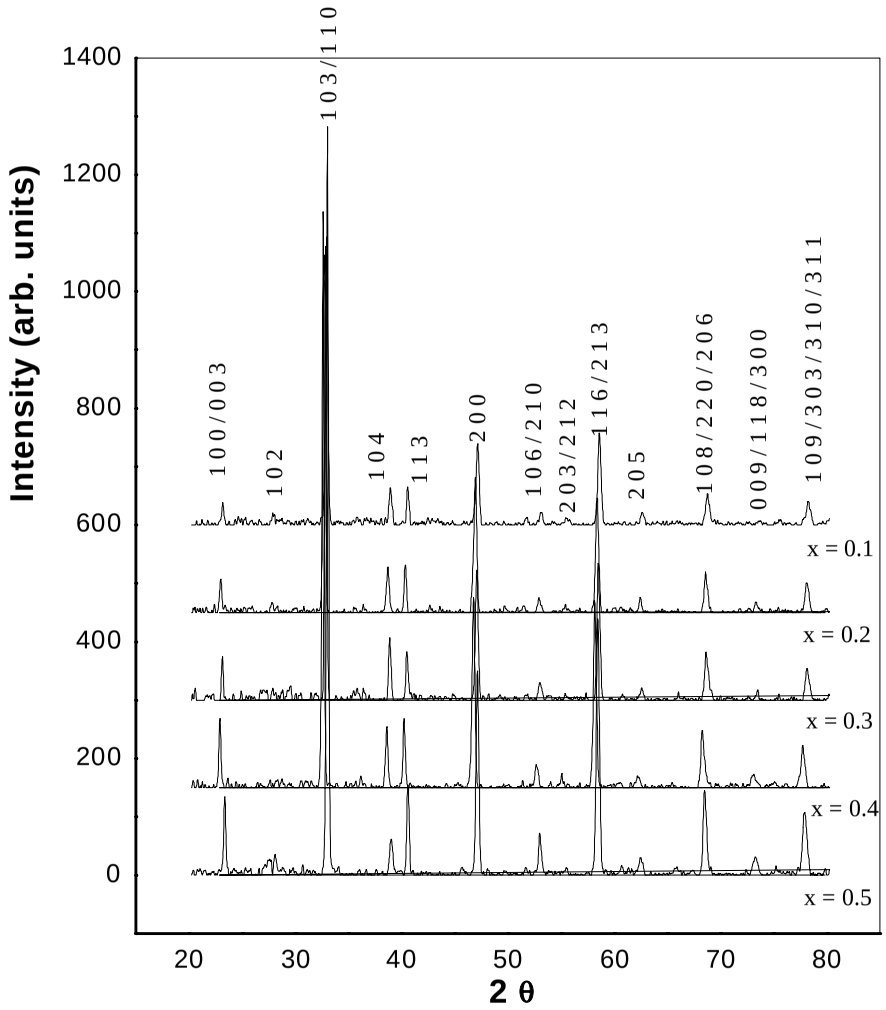

Figure 5.1 Indexed XRD patterns for LaPrCaBCO system

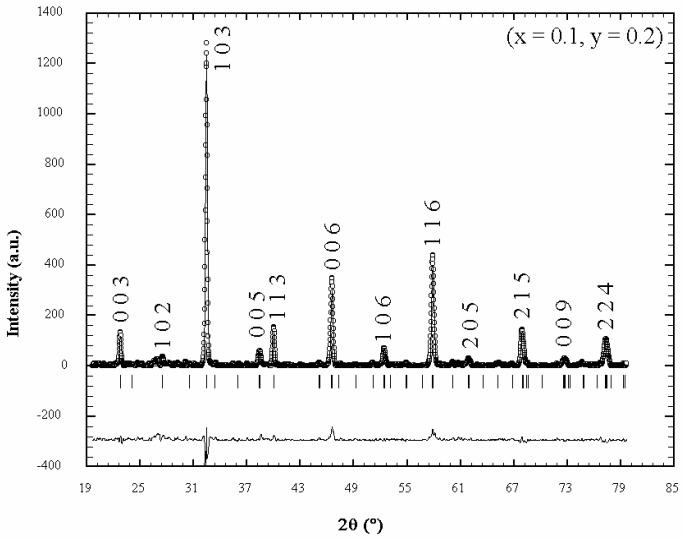

Figure 5.2 (a) Rietveld fitted XRD pattern for LaPrCaBCO, (x = 0.1,y = 0.2) sample

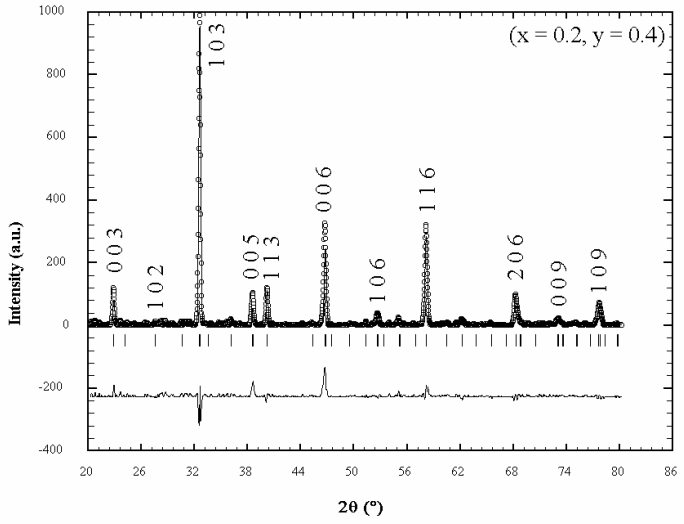

Figure 5.2 (b) Rietveld fitted XRD pattern for LaPrCaBCO, (x = 0.2,y = 0.4) sample

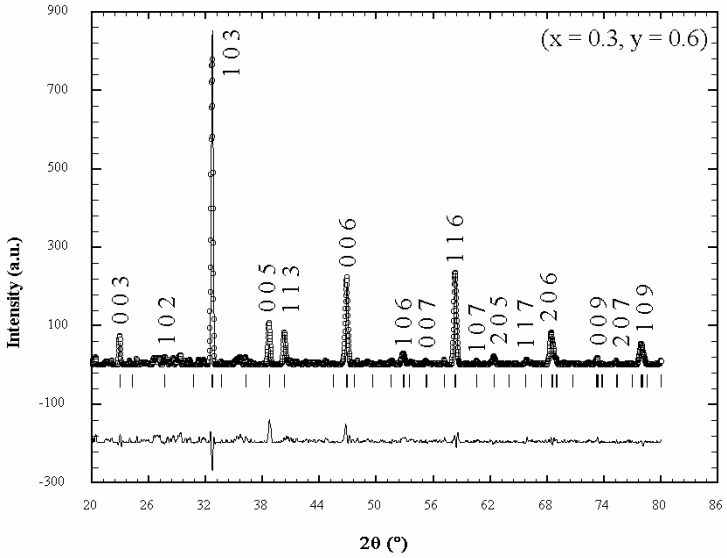

Figure 5.2 (c) Rietveld fitted XRD pattern for LaPrCaBCO, (x = 0.3, y = 0.6) sample

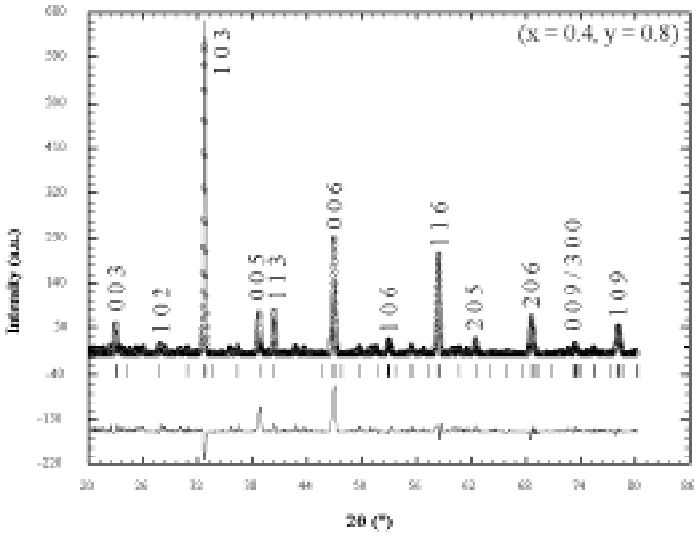

Figure 5.2 (d) Rietveld fitted XRD pattern for LaPrCaBCO, (x = 0.4, y = 0.8) sample

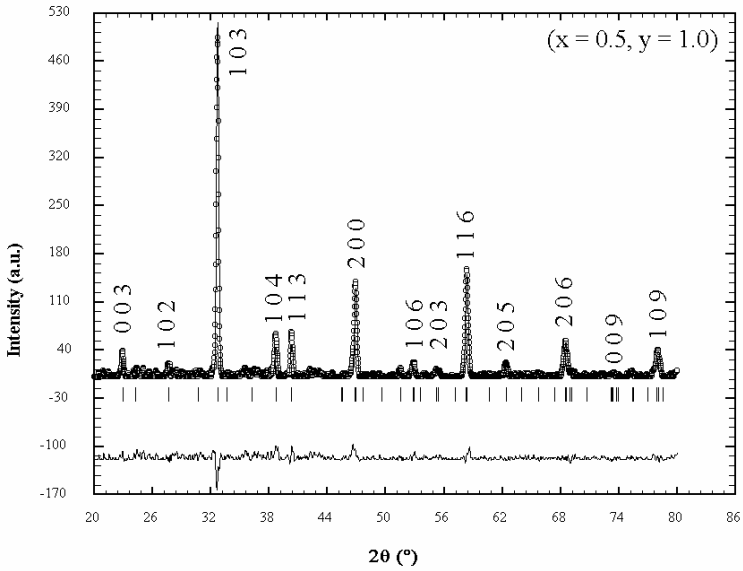

Figure 5.2 (e) Rietveld fitted XRD pattern for LaPrCaBCO, (x = 0.5,y = 1.0) sample

The results of the Rietveld analysis for the LaPrCaBCO samples are tabulated in Table 5.2. The site occupancies, atomic positions, unit cell parameters were varied during the refinement cycle. Since the XRD is insensitive to oxygen, the site occupancy of oxygen was kept fixed and not varied during the refinement. All the other parameters like atomic positions, unit cell parameters, thermal parameters, scale factor, zero shift angle were varied until the refinement cycle converge. The reliable R-values obtained from the converging cycle were taken as final values.

The Table 5.2 lists the values obtained from the Rietveld analysis of the X-ray diffraction data.

Table 5.2 Values obtained from XRD Rietveld analysis

	Sample (x, y)				
Parameters	(0.1, 0.2)	(0.2, 0.4)	(0.3, 0.6)	(0.4, 0.8)	(0.5, 1.0)
Space group	P4/MMM	P4/MMM	P4/MMM	P4/MMM	P4/MMM
a = b (Å)	3.8988 (3)	3.8824 (3)	3.8724 (3)	3.8650 (3)	3.8712 (3)
c (Å)	11.7235 (8)	11.6698 (8)	11.6417 (8)	11.6336 (8)	11.6388 (8)
La/Nd/Ca (½, ½, ½)					
N_{La}	0.821	0.630	0.451	0.476	0.274
N_{Pr}	0.035	0.143	0.184	0.226	0.275
N_{Ca}	0.035	0.094	0.279	0.226	0.395
Ba (½,½, z)					
z	0.1804	0.1830	0.1819	0.1864	0.1868
N	1.433	1.328	1.242	1.255	1.120
La @ Ba (N)	0.505	0.509	0.594	0.505	0.560
Ca @ Ba (N)	0.076	0.090	0.142	0.255	0.180
Cu (1) (0,0,0)					
N	1.000	1.000	1.000	1.000	1.000
Cu (2) (0,0,z)					
z	0.3504	0.3521	0.3535	0.3536	0.3596
N	2.0000	2.0000	2.0000	2.0000	2.0000
O (1) (0,½,0)					
N	1.0562	1.3192	1.0100	0.9415	1.5050
O (2) (0,0,z)					
z	0.1527	0.1687	0.1594	0.1626	0.1575
N	2.0000	2.0000	2.0000	2.0000	1.3903
O (4) (0,½,z)					
z	0.3653	0.3799	0.3687	0.3622	0.3735
N	4.0000	4.0000	4.0000	4.0000	3.1823
Total Oxygen					
(z' – in 123)	7.0562	7.3192	7.0997	6.9415	7.0692
(z – in 2125)	9.8786	10.7348	10.8862	11.1064	11.7820
R-factors					
χ^2	2.18	2.01	2.20	1.96	1.57
R_{wp}	34.6	38.3	44.1	45.3	44.3
R_p	22.8	28.9	30.6	35.2	32.7

5.1.2 ***Transport measurements***: The four probe d.c. resistivity technique was used to study the variation in resistance as a function of temperature which gives the values of transition temperatures. Figure 5.3 shows the normalized resistance versus temperature plots for all LaPrCaBCO samples.

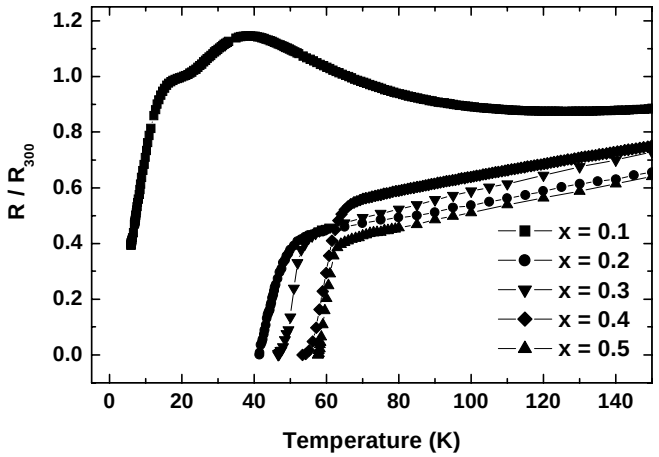

Figure 5.3 Normalized resistance versus temperature plot for LaPrCaBCO system

The maximum transition temperature $T_c^{R=0}$ ~ 58K has been observed in x = 0.5 which is ~ 20 K less than the conventional $La_{1.5}RE_{0.5}Ca_1Ba_2Cu_5O_z$ system.

5.1.3 Magnetic measurements: The d.c. susceptibility measurements were performed on few selected bulk samples of LaPrCaBCO system in order to verify the transition temperatures obtained from electrical method. Figure 5.4 shows the magnetic moment versus temperature plots for LaPrCaBCO system. The susceptibility measurements were performed using the Vibrating Sample Magnetometer (VSM) at TIFR, Mumbai.

The values of the transition temperatures obtained from resistivity and d.c. susceptibility measurements are tabulated in Table 5.3. It can be seen that, both the

values agree fairly well, showing good quality of samples and reliability of measurements.

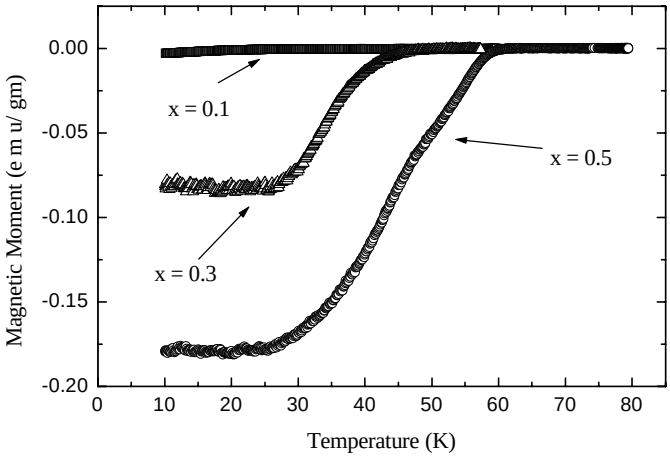

Figure 5.4 Magnetic moment versus temperature plots for LaPrCaBCO system

5.1.4 Iodometric titration: Iodometric double titration has been performed on all the samples of LaPrCaBCO system to determine the oxygen content per unit cell and hence calculate the effective copper valence and hole concentration. Table 5.3 gives the values of oxygen content obtained from iodometric analysis. It can be seen that, oxygen content (z) and hence hole concentration in CuO_2 (p_{sh}) increases with increasing Pr – content.

Table 5.3 Values of T_c, oxygen contents and hole concentration

Pr concentration	Transition temperature (K)		Oxygen content (in 123 & 2125)		Hole concentration	
(x)	$T_c^{R=0}$	$T_c^{M\ ON}$	z'	Z	p	p_{sh}
0.1	--	16	6.6708	9.3391	0.1138	0.0854
0.2	35	--	6.7732	9.9340	0.1821	0.1366
0.3	48	48	6.8405	10.4887	0.2270	0.1702
0.4	54	--	6.8631	10.9810	0.2420	0.1815
0.5	58	59	6.8702	11.4504	0.3800	0.1851

5.2 STUDIES ON LaNdCaBCMoO SYSTEM

5.2.1 ***X-ray Diffraction studies***: The room temperature X-ray diffractograms were recorded on all powdered samples of $La_{1.5}Nd_{0.5}Ca_1Ba_2(Cu_{1-x}Mo_x)_5O_z$ for x = 0.00 – 0.20; (LaNdCaBCMoO) system using the Cu-K_α radiation with λ = 1.5408 Å. Figure 5.5 shows the indexed patterns of LaNdCaBCMoO samples.

It can be seen from the figures that, number of impurity peaks with (*) indication increases with increasing Mo content. These impurity peaks cannot be indexed in La-2125 tetragonal structure, which may be due to un-reacted components or secondary phase formation at higher Mo-doping concentrations. XRD plots of x = 0.15 and x = 0.20 are hence not shown.

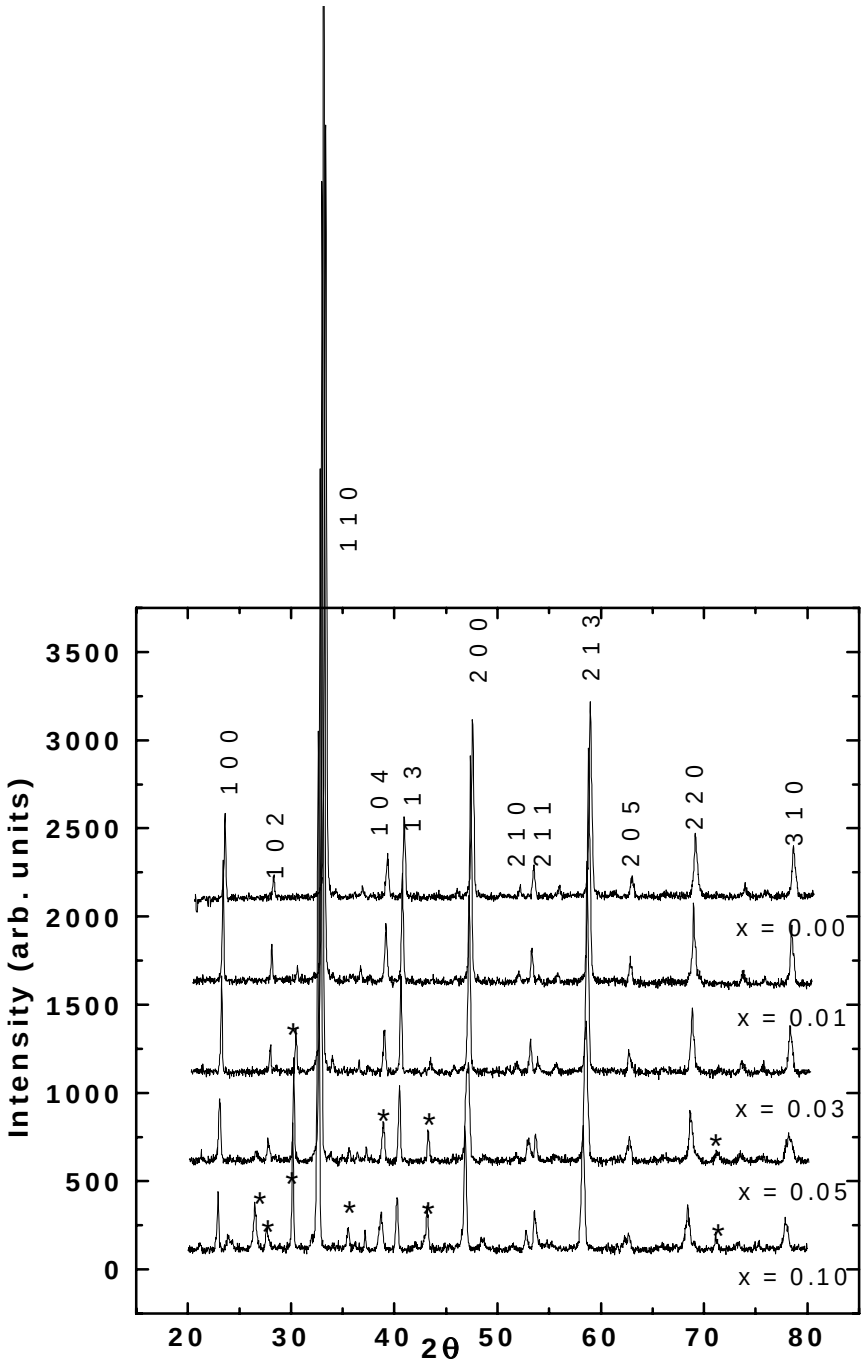

Figure 5.5 Typical XRD patterns for few $La_{1.5}Nd_{0.5}Ca_1Ba_2(Cu_{1-x}Mo_x)_5O_z$ samples

The unit cell parameters were calculated from the XRD patterns for all the samples of LaNdCaBCMoO samples using least square fitting method. The values of unit cell parameters, unit cell volume obtained from XRD analysis have been tabulated in Table 5.4. Increasing the Ca concentration in $La_{1.5-y}Nd_{0.5}Ca_{1+y}(Cu_{1-x}Mo_x)_5O_z$ sample for x = 0.2, y = x, 2x and 3x samples, do not contribute to the superconducting properties, and also do not contribute to structural improvement also. Increase of Ca in the $La_{1.5-y}Nd_{0.5}Ca_{1+y}(Cu_{1-x}Mo_x)_5O_z$; x = 0.2, y = x, 2x and 3x samples leads to multiphase formations having large impurity due to excess Ca-doping and the XRD patterns (not shown) cannot be fitted in La-2125 tetragonal structure.

Table 5.4 ***Unit cell parameters, volume and X-ray densities for LaNdCaBCMoO samples***

Mo concentration (x)	**a = b (Å)**	**c (Å)**	**Volume ($Å^3$)**	**X-ray Density (ρ) (gm / cm^3)**
0.00	3.8677 (3)	11.5998 (8)	173.5226	10.4119
0.01	3.8727 (3)	11.5998 (8)	173.9715	10.4856
0.03	3.8739 (3)	11.5994 (8)	174.0733	10.4798
0.05	3.8664 (3)	11.5703 (8)	172.9649	10.6056
0.10	3.8122 (3)	11.6146 (8)	168.9794	11.0157

5.2.2 ***Resistivity measurements***: D.C. four-probe resistance measurements were carried out on all the LaNdCaBCMoO and $LaNdCa_yBCMoO$ samples in the temperature range, from RT - 20 K using closed cycle cryostat for the determination

of resistive transition temperatures. Values of the $T_c^{R=0}$ obtained from R-T measurements have been tabulated in Table 5.5.

Figs. 5.6 (a) & (b) shows the normalized resistance versus temperature dependence of different Mo doped LaNdCaBCMoO samples. It can be seen from the Figure 5.6 (a) that up to x = 0.10 sample, all the samples exhibit metallic behavior and T_c is suppressed at the rate of 4K / atm % of Mo-doping. Figure 5.6 (b) shows that, samples with x = 0.15 and 0.20 exhibit large resistance and does not show $T_c^{R=0}$.

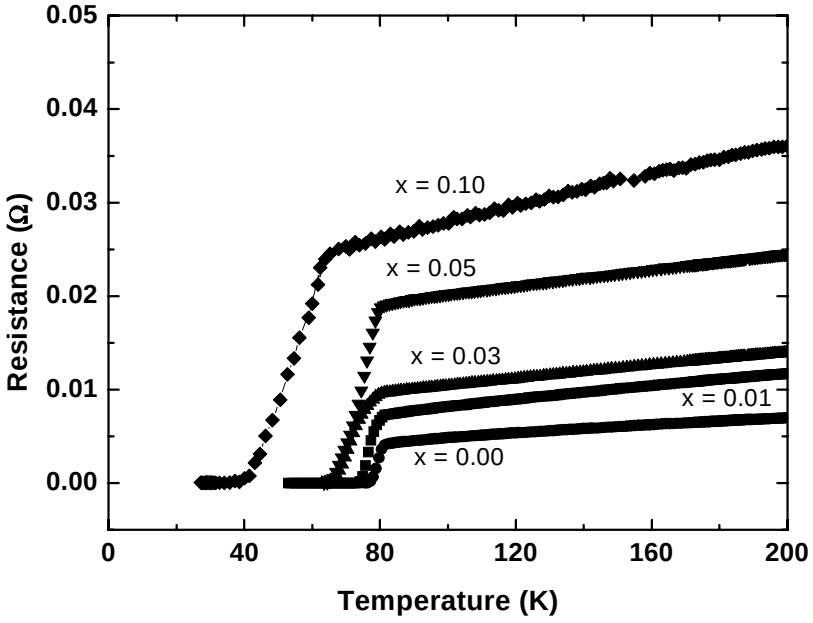

Figure 5.6 (a) R-T plots for $La_{1.5}Nd_{0.5}Ca_1Ba_2(Cu_{1-x}Mo_x)_5O_z$ samples (x = 0.00 – 0.10)

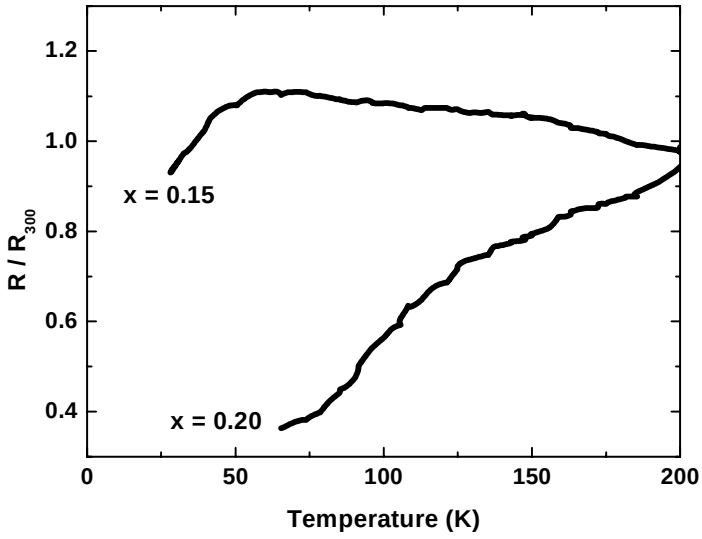

Figure 5.6 (b) R-T plots for $La_{1.5}Nd_{0.5}Ca_1Ba_2(Cu_{1-x}Mo_x)_5O_z$ samples (x = 0.15 & 0.20)

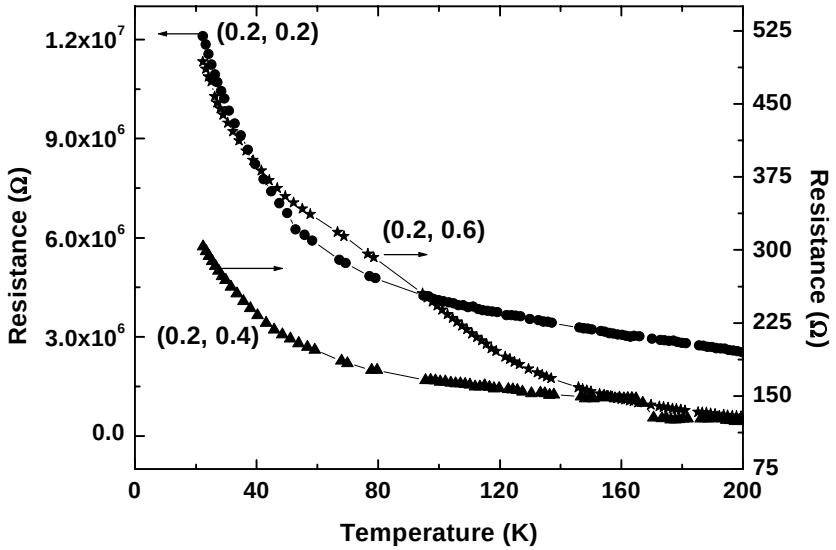

Figure 5.6 (c) R-T plots for $La_{1.5-y}Nd_{0.5}Ca_{1+y}Ba_2(Cu_{1-x}Mo_x)_5O_z$ samples

Figure 5.6 (c) shows that, with increasing Ca in Mo substituted LaNdCaBCMoO system, leads to highly resistive semi-conductive system. For

x = y = 0.20 in $La_{1.5-y}Nd_{0.5}Ca_{1+y}Ba_2[Cu_{1-x}Mo_x]_5O_z$ system, the resistance goes up to Mega-Ohm range but on further increase in Ca (y = 2x, 3x), the resistance decreases to few hundred Ohms, but the system still remains semi-conducting.

Table 5.5 ***Values of T_c, oxygen content, hole concentration of Mo-Ca doped La-2125 system***

Concentration	**Transition temperature (K)**		**Oxygen content (in 123 & 2125)**		**Hole concentration**	
(x, y)	**$T_c^{R=0}$**	**T_c^{Mon}**	**z'**	**z**	**p**	**p_{sh}**
(0.00, 0.00)	78 (1)	77 (1)	6.950 (3)	11.583 (8)	0.300	0.225
(0.01, 0.00)	74 (1)	75 (1)	6.807 (3)	11.345 (8)	0.205	0.153
(0.03, 0.00)	66 (1)	68 (1)	6.793 (3)	11.322 (8)	0.195	0.146
(0.05, 0.00)	64 (1)	65 (1)	6.686 (3)	11.143 (8)	0.124	0.093
(0.10, 0.00)	39 (1)	55 (1)	6.671 (3)	11.119 (8)	0.114	0.085
(0.15, 0.00)	NS	--	6.666 (3)	11.110 (8)	0.1109	0.083
(0.20, 0.00)	NS	--	6.652 (3)	11.087 (8)	0.1015	0.076
(0.20, 0.20)	NS	--	--	--	--	--
(0.20, 0.40)	NS	--	--	--	--	--
(0.20, 0.60)	NS	--	--	--	--	--

NS: Non - superconducting

5.2.3 ***Magnetic measurements***: Few selected samples of LaNdCaBCMoO system were studied for their magnetic properties by d.c.susceptibility and d. c. magnetization using MPMS (Magnetic Property measurement system) at TIFR, Mumbai. The d. c. susceptibility measurements on all the samples studied (M-T) were taken at 20 Oe

field. Figure 5.7 shows the variation in magnetic moments observed as a function of temperature for all the samples investigated. Values of the transition temperature obtained from M – T curves ($T_c^{M^{on}}$) are tabulated in Table 5.5, which agrees well with $T_c^{R=0}$ values.

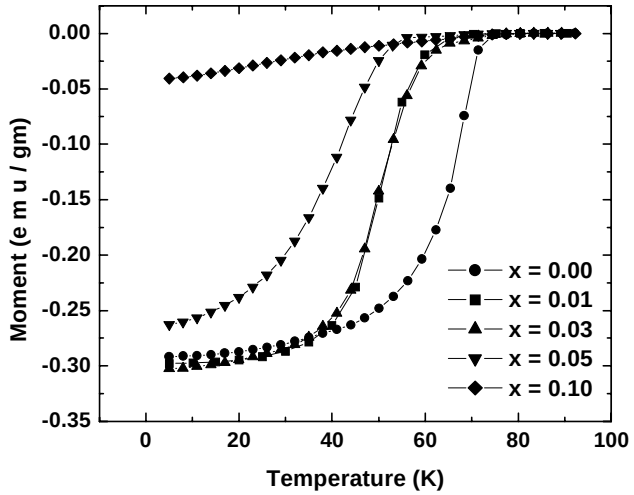

Figure 5.7 M - T plots for $La_{1.5}Nd_{0.5}Ca_1Ba_2(Cu_{1-x}Mo_x)_5O_z$ samples (x = 0.00 – 0.10)

The magnetization measurements as a function of field at different temperatures were performed on few selected samples of LaNdCaBCMoO system in order to determine their current densities. Figures 5.8 (a-d) shows the magnetic hysteresis loops for LaNdCaBCMoO samples with x = 0.00 – 0.05 obtained at different temperatures and fields.

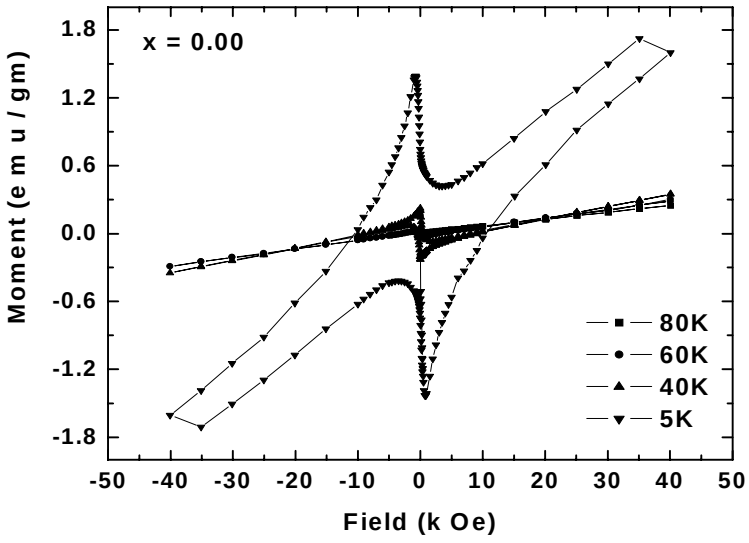

Figure 5.8 (a) M - H loops for $La_{1.5}Nd_{0.5}Ca_1Ba_2(Cu_{1-x}Mo_x)_5O_z$ (x = 0.00) sample

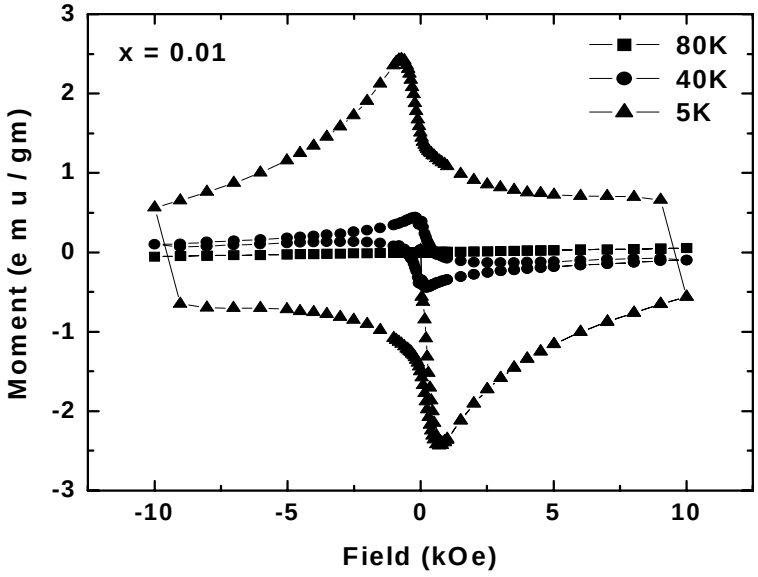

Figure 5.8 (b) M - H loops for $La_{1.5}Nd_{0.5}Ca_1Ba_2(Cu_{1-x}Mo_x)_5O_z$ (x = 0.01) sample

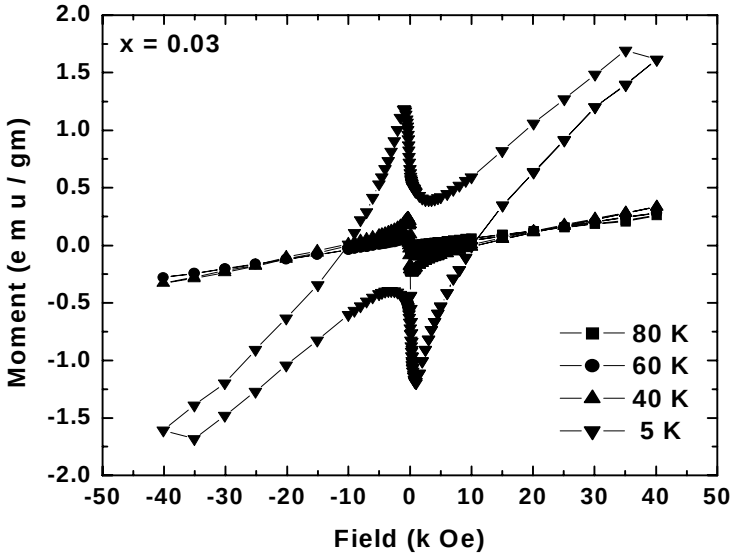

Figure 5.8 (c) M - H loops for $La_{1.5}Nd_{0.5}Ca_1Ba_2(Cu_{1-x}Mo_x)_5O_z$ (x = 0.03) sample

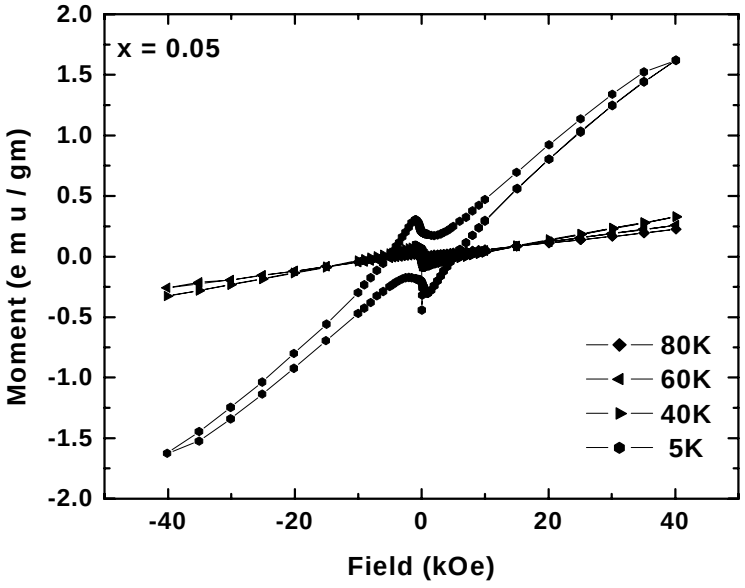

Figure 5.8 (d) M - H loops for $La_{1.5}Nd_{0.5}Ca_1Ba_2(Cu_{1-x}Mo_x)_5O_z$ (x = 0.05) sample

It can be seen from these figures that with increasing Mo concentration, the magnetic hysterisis loop collapses. The current density for each sample has been calculated using Bean's critical state model according to the following formula,

$$J_c = \left(\frac{30\Delta M}{D} \right) * \rho \qquad \ldots (1)$$

Where, J_c = current density in A/cm^2

ΔM = width of the magnetization loop at a particular H

D = average grain size (~ $2.3 * 10^{-4}$ cm)

ρ = X-ray density (g/cm^3)

The values of the magnetic current densities of different Mo-doped samples determined at different temperatures and fields are tabulated in Table 5.6.

Table 5.6 ***J_c values for $La_{1.5}Nd_{0.5}Ca_1Ba_2(Cu_{1-x}Mo_x)_5O_z$ samples***

Sample	Temperature (K)	Field H (kOe)	J_c (X 10^6 A/cm^2)
$La_{1.5}Nd_{0.5}Ca_1Ba_2Cu_5O_z$ (x = 0.00)	05	5.5556	1.1502
		10.0000	0.9448
		13.3300	0.7805
		20.0000	0.6161
		23.8888	0.5304
		30.0000	0.4518
		35.5555	0.3286
$La_{1.5}Nd_{0.5}Ca_1Ba_2Cu_{4.95}Mo_{0.05}O_z$ (x = 0.01)	05	0.9716	3.7755
		2.6372	3.4323
		3.4700	3.0318
		3.5394	3.0032
		4.5112	2.6686
		5.9684	2.2882
$La_{1.5}Nd_{0.5}Ca_1Ba_2Cu_{4.95}Mo_{0.05}O_z$ (x = 0.01)	40	0.4838	0.4970
		1.0483	0.4083
		1.7741	0.2589
		2.0161	0.2485
		3.0645	0.1450
		3.6290	0.1346
		5.1612	0.1035
		8.8710	0.7249
$La_{1.5}Nd_{0.5}Ca_1Ba_2Cu_{4.85}Mo_{0.15}O_z$ (x = 0.03)	05	2.5000	1.5780
		6.9444	1.0777
		15.0000	0.6543
		18.0555	0.6158
		27.2222	0.4618
		33.3333	0.4233
	40	1.6667	0.8467
		2.2222	0.7697
		5.0000	0.3858
		12.7778	0.1539
		27.2222	0.0768

Table 5.6 continued…

Sample	Temperature (K)	Field H (kOe)	J_c (X 10^6 A/cm^2)
$La_{1.5}Nd_{0.5}Ca_1Ba_2Cu_{4.75}Mo_{0.25}O_z$ (x = 0.05)	05	2.2222	0.6080
		3.8880	0.5007
		6.1110	0.3576
		15.227	0.2147
		21.111	0.1788
		32.770	0.1430

5.2.4 ***Iodometric titration***: Iodometric double titration was performed on all the samples of the LaNdCaBCMoO series to determine the oxygen content and hole concentration as a function of increasing Mo concentration. The values of the oxygen content, X-ray density, and hole concentration for all the samples studied are tabulated in Table 5.5.

5.3 DISCUSSION

Results of the experimental investigations on Pr-doped $La_{2-x}Pr_xCa_yBa_2Cu_{4+y}O_z$; (LaPrCaBCO); x = 0.1 – 0.5, y = 2x and Mo-doped $La_{1.5}Nd_{0.5}Ca_1Ba_2(Cu_{1-x}Mo_x)_5O_z$; x = 0.00 – 0.10, (LaNdCaBCMoO) samples studied for their structural, electrical and magnetic properties have been discussed in this section. Rietveld analysis of the XRD data was done to determine the occupancy of dopants at different sites while d.c. four probe method was used to study the R-T behavior for the determination of T_c. D.C. Magnetization measurements performed at different temperatures and fields were used for the determination of magnetic J_c of Mo-doped La-2125 samples.

5.3.1 *Studies on LaPrCaBCO system*

Values of the unit cell parameters and unit cell volume obtained from XRD analysis are given in Table 5.1. Variation of unit cell parameters and volume with increasing Pr-concentration in LaPrCaBCO system is shown in Figure 5.9. It can be seen from the figure that, lattice parameters and hence volume decreases with increasing Pr and Ca content, which may be attributed to the smaller ionic radii ($Pr^{3+/4+}$, r_{Pr} = 0.99 / 0.85 Å and Ca^{2+}, r_{Ca} = 1.00 Å) occupying La^{3+}(r_{La} = 1.03 Å) ion.

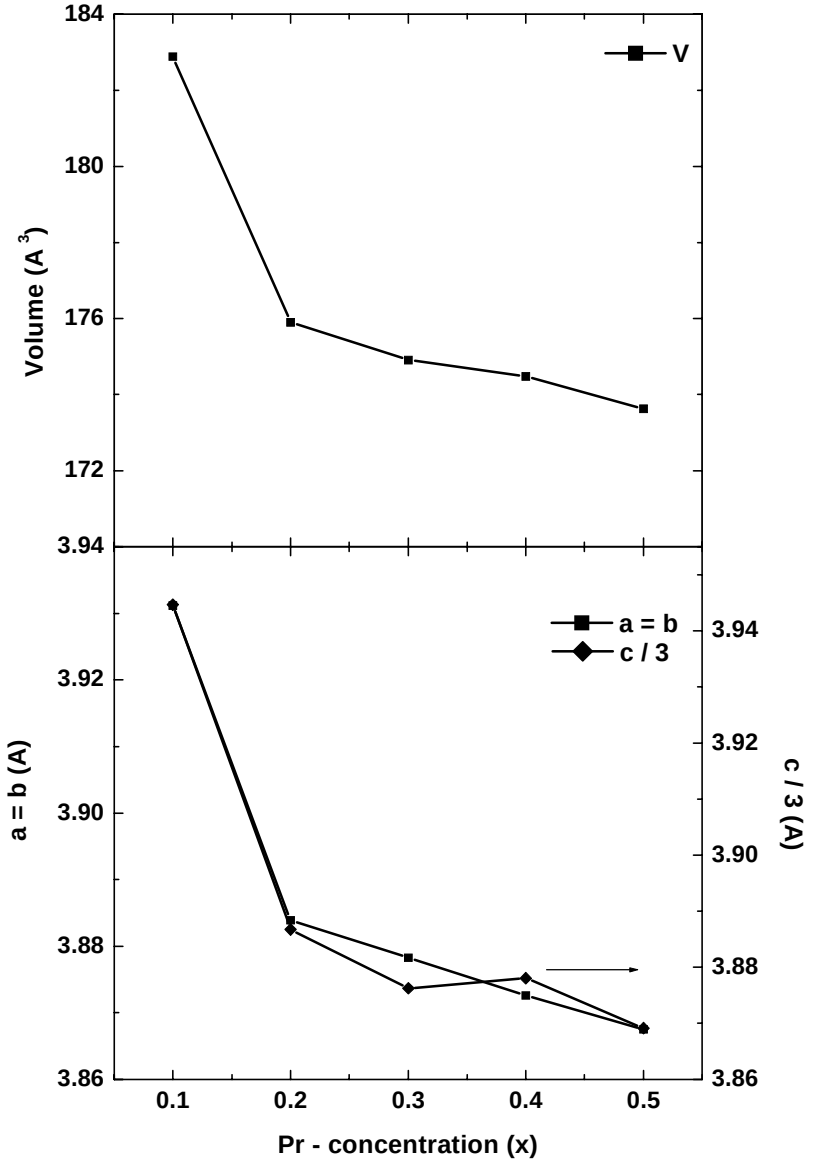

Figure 5.9 ***Variation of unit cell parameters and volume with increasing Pr (x) concentration***

The detailed structural studies were carried out on all the samples of LaPrCaBCO system using the FULLPROF program. The XRD patterns were refined

using RE-123 tetragonal structure as a starting model, which fitted well into the assumed structure with P 4/M M M space group. The results of the Rietveld analysis of the XRD data are given in Table 5.2. It can be clearly seen from the table that, as observed in the analysis of La-Dy-2125 samples, Ca is distributed at both La and Ba sites along with concomitant displacement of La onto Ba site with increasing Pr and Ca concentration. Out of total Ca in the sample, the Ca concentration increases from 35 % (for x = 0.1) to 68% (x = 0.5) at La site. The occupancy of Ca at La site increases from 39% - 41 %.

Figure 5.10 shows increase in hole concentration (in CuO_2 sheets) and oxygen content with increasing Pr-concentration. In the Pr substituted RE-123 samples, the fluctuating valence of Pr ($Pr^{3+/4+}$) plays the role of localizing the mobile holes in the conducting planes thus suppressing superconductivity with increasing Pr content. Various models have been proposed to explain the suppression of T_c by Pr substitution. In the present study, Pr is substituted at La site, which can be considered equivalent to the substitution of Pr at RE site in RE-123 system. But in RE substituted La-2125 systems, the La site is occupied by La, RE and Ca. Hence, the increase in T_c with increasing Pr substitution can be attributed to the hole doping by Ca^{2+}, which overcomes the hole filling by Pr^{4+} at La^{3+} site, resulting into enhancement in T_c.

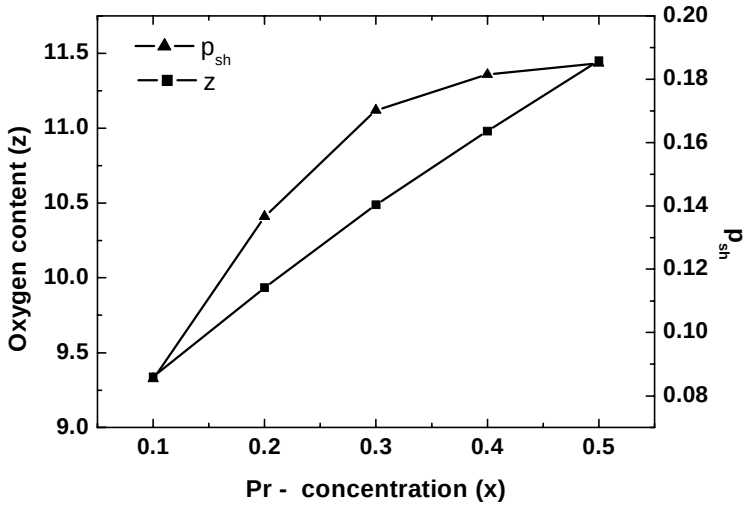

Figure 5.10 Variation in oxygen content (z) and hole concentration in sheets (p_{sh}) as a function of Pr concentration (x)

Figure 5.11 shows the variation of T_c as a function of increasing Pr concentration.

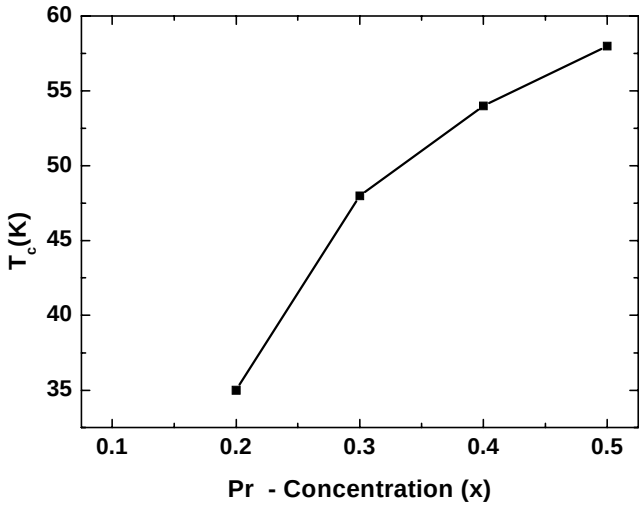

Figure 5.11 Variation in T_c as a function of Pr concentration (x)

Our studies on the $La_{2-x}RE_xCa_yBa_2Cu_{4+y}O_z$, RE = Y, Er, Nd, Dy etc, system establishes the fact that, with increase in RE and Ca (x = 0.0 – 0.5, y = 2x) as per the stoichiometry, there is increase in the hole concentration in the CuO_2 sheets, which is responsible for inducing the superconductivity. The maximum T_c ~ 75 K is achieved for x = 0.5 (i.e., La-Dy-2125 phase) composition [23]. As Figure 5.12 depicts, the LaPrCaBCO system is an exception to these findings. The rate of increase in T_c, with increase in Pr and Ca concentration, is less as compared to Dy or Nd systems. The possible reason for this exception can be due to the fluctuating valence of $Pr^{3+,\ 4+}$ substituting at La^{3+} site and the hole filling by $Pr^{>3+}$ cannot be fully compensated by hole doping by Ca^{2+} at La^{3+}. The holes contributed by Ca helps in de-localizing the mobile charges in the conducting CuO_2 planes. This results into the difference in maximum T_cs achieved for x = 0.5 composition in $La_{2-x}Pr_xCa_yBa_2Cu_{4+y}O_z$ stoichiometry and other RE doped $La_{2-x}(Nd/Dy)_xCa_yBa_2Cu_{4+y}O_z$ systems (Figure 5.12).

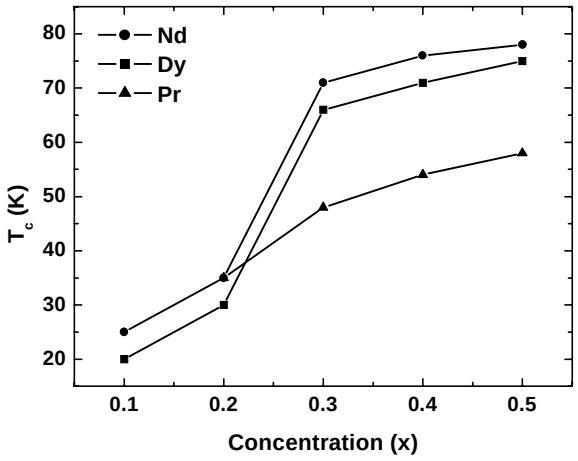

Figure 5.12 Comparison of increase in T_c with increasing RE and Ca in $La_{2-x}RE_xCa_yBa_2Cu_{4+y}O_z$ system

5.3.2 *Studies on LaNdCaBCMoO system*

The variation of unit cell parameters (a, b and c) and unit cell volume for all the samples in the $La_{1.5}Nd_{0.5}Ca_1Ba_2(Cu_{1-x}Mo_x)_5Oz$; x = 0.00 – 0.10 series is shown in Figure 5.13. The figure shows the variation of unit cell parameters with increasing Mo concentration at Cu site. It is important to note here that, the changes in the unit cell parameters can be due to the fluctuating valence of Mo, which exists in $Mo^{3+, 4+, 5+, 6+}$ states. The ionic radii of each respective valence state is 0.69, 0.65, 0.61, 0.59 Å. At lower Mo concentrations, the change in unit cell parameters is very small, but at higher concentrations of Mo, there is sharp change which can be due to the appearance of secondary phases or un-reacted constituents indicated by impurity peaks in the XRD patterns (Figure 5.5).

The Figure 5.14 shows the decrease in oxygen content (z) and hole concentration in CuO_2 sheets (p_{sh}) with increasing Mo concentration (x). The plot clearly shows that, oxygen content and hence hole concentration decreases with increasing Mo-concentration indicating that Mo exists in > 3+ state. The decrease in z and p_{sh} may be attributed to the hole filling by $Mo^{>3+}$ resulting into lowering of charge carriers and hence suppression of superconductivity. This has been shown in the T_c variation with Mo-doping concentration in Figure 5.15.

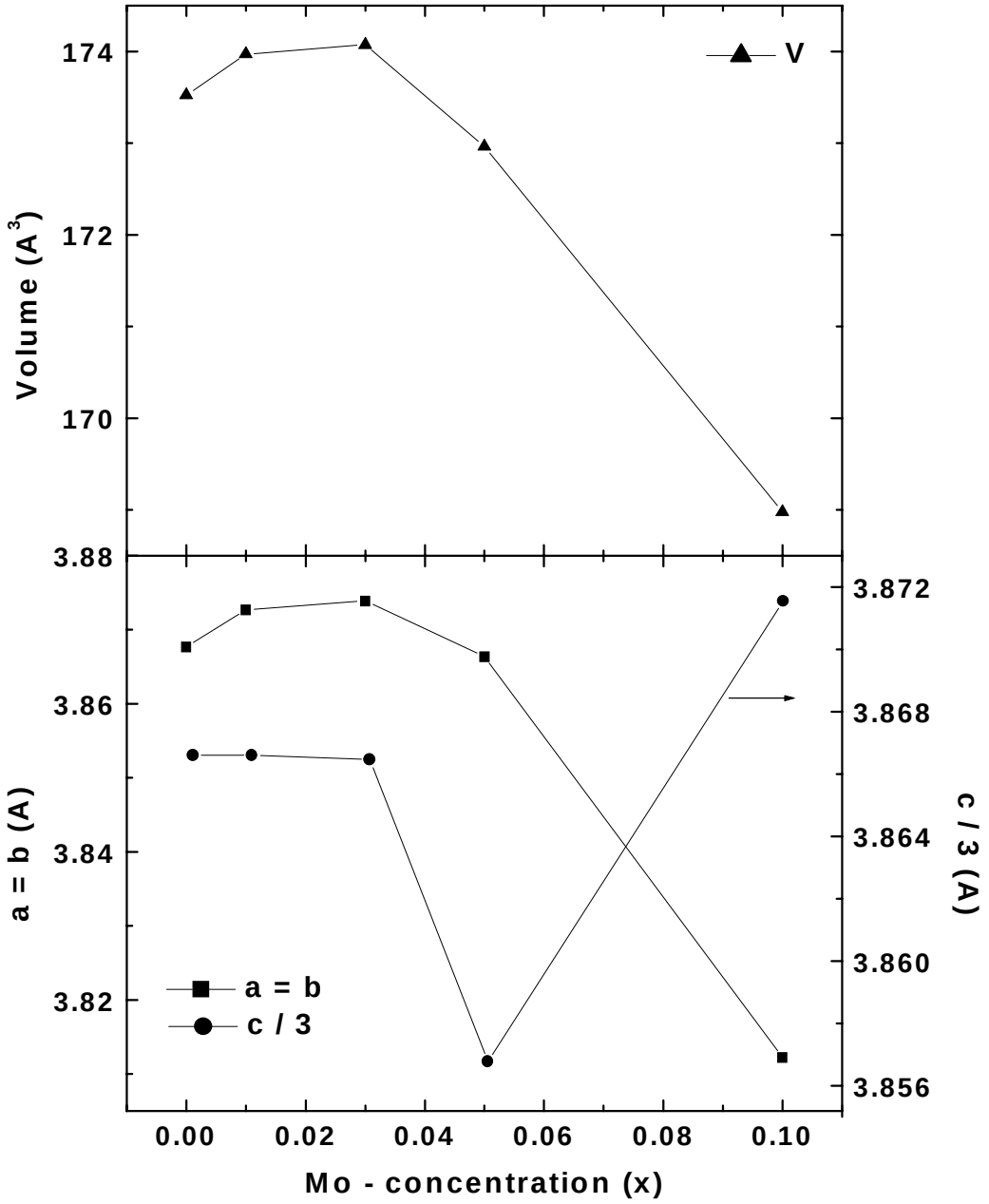

Figure 5.13 ***Variation of unit cell parameters and volume with increasing Mo (x) concentration***

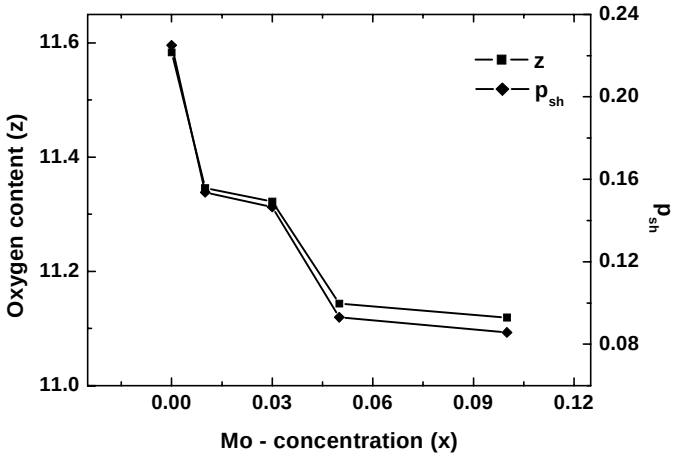

Figure 5.14 *Decrease in z, p_{sh} with increasing Mo concentration in $La_{1.5}Nd_{0.5}Ca_1Ba_2(Cu_{1-x}Mo_x)_5O_z$ samples*

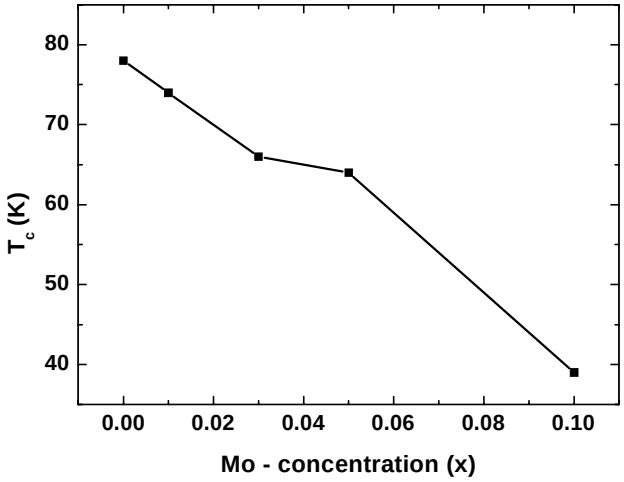

Figure 5.15 *Decrease in T_c with increasing Mo concentration in $La_{1.5}Nd_{0.5}Ca_1Ba_2(Cu_{1-x}Mo_x)_5O_z$ samples*

It is interesting to study the effect of substitution of $Mo^{>3+}$ (r_{Mo} = 0.65Å - 0.59Å) at Cu^{2+} (r_{Cu} = 0.73Å). The mismatch in ionic radii results in introducing the defects in the crystal structure, which acts as flux trapping centers, called 'point

defects'. The Figures 5.16 (a & b) show the current densities measured for few samples of the LaNdCaBCMoO system as a function of applied field at 5 K and 40 K respectively.

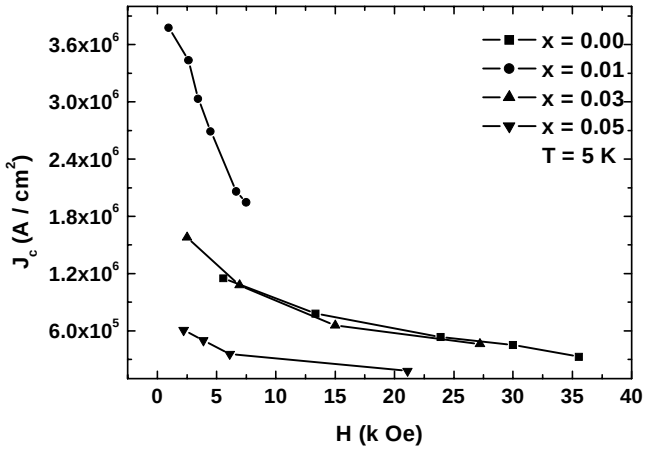

Figure 5.16 (a) Current density for $La_{1.5}Nd_{0.5}Ca_1Ba_2(Cu_{1-x}Mo_x)_5O_z$ samples at 5 K.

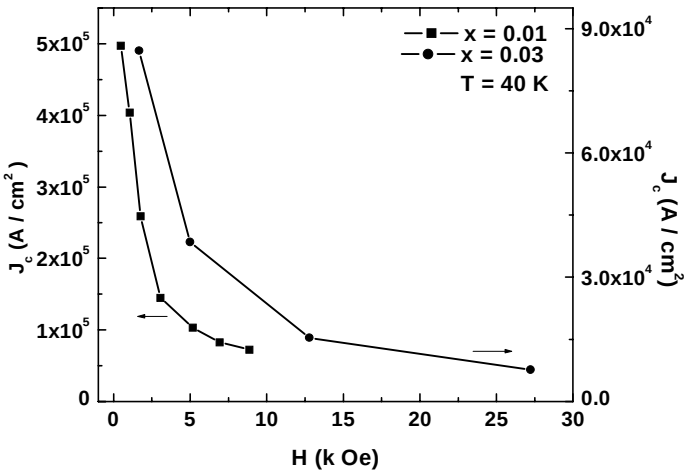

Figure 5.16 (b) Current density for $La_{1.5}Nd_{0.5}Ca_1Ba_2(Cu_{1-x}Mo_x)_5O_z$ samples at 40 K.

Figure 5.17 (a & b) shows the plots $\ln J_c$ vs $\ln H$ at 5 K and 40 K respectively. It can be observed from these figures that, J_c decreases with increasing temperature and field.

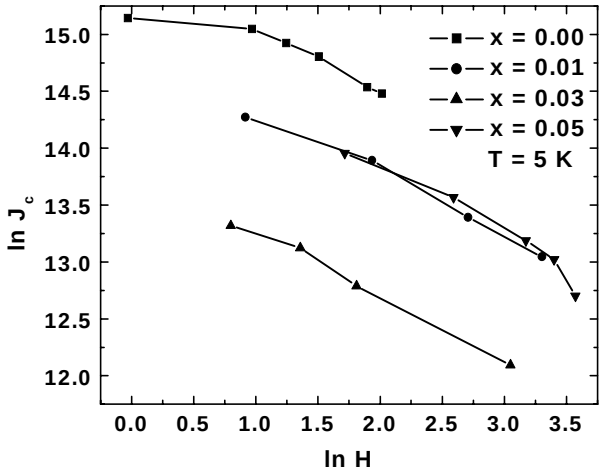

Figure 5.17 (a) $\ln J_c$ versus $\ln H$ for $La_{1.5}Nd_{0.5}Ca_1Ba_2(Cu_{1-x}Mo_x)_5O_z$ samples at 5 K

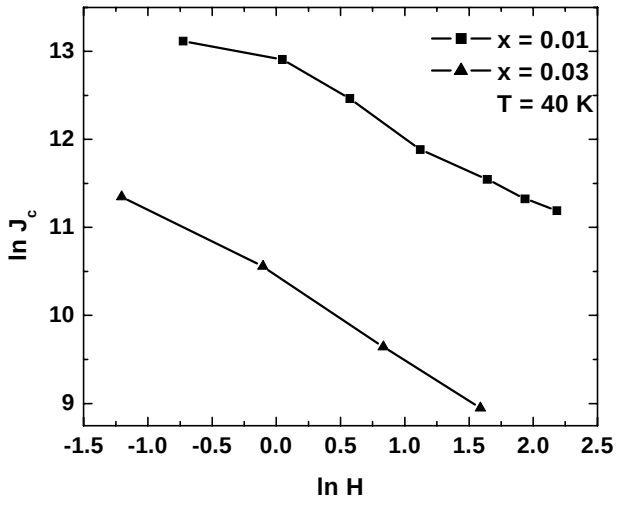

Figure 5.17 (b) $\ln J_c$ versus $\ln H$ for $La_{1.5}Nd_{0.5}Ca_1Ba_2(Cu_{1-x}Mo_x)_5O_z$ samples at 40 K

The flux creep model accounts for the behavior of J_c in magnetic fields. The field dependence of J_c is given by

$$\mathbf{J_c \propto H^{-n}\ (n = 0.5)} \qquad \ldots(2)$$

where, the gradient (-n) of the plots is obtained by the slope of ln J_c vs. ln H plot. Figure 5.18 shows the increase in 'n' as a function of increasing Mo (x) concentration in $La_{1.5}Nd_{0.5}Ca_1Ba_2Cu_{5-x}Mo_xO_z$, the values of which are given in Table 5.7.

Table 5.7 Values of the gradient of slope (-n), with increasing Mo concentration

Mo-concentration (x)	n
0.00	0.3326
0.01	0.3359
0.03	0.5226
0.05	0.5576

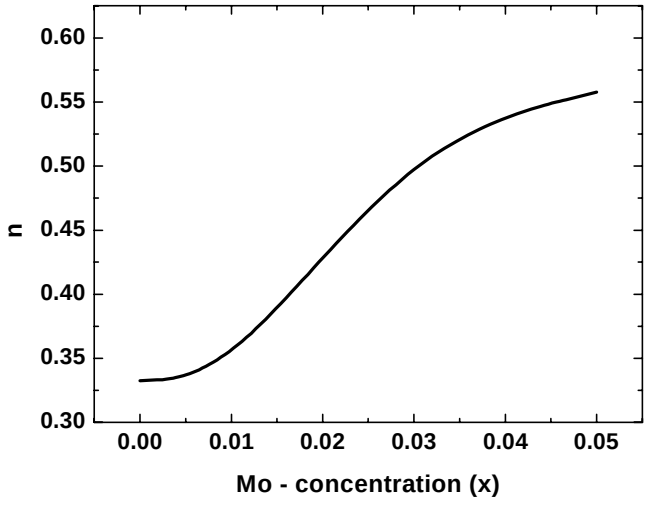

Figure 5.18 Variation in the slope of lnJ_c vs lnH with increasing Mo concentration in $La_{1.5}Nd_{0.5}Ca_1Ba_2(Cu_{1-x}Mo_x)_5O_z$ system

As can be seen from above figure and table, the observed values of the gradients (-n) of the plots are within the limits of the experimental uncertainties and thus the Mo doped La-2125 system can be seen to obey the flux creep model of field dependence of J_c.

The Figure 5.19 shows the current density values for different Mo doped samples at a particular field and temperature (H = 6 k Oe, T = 5 K). The maximum current density has been observed for x = 0.01 (i.e., 1 % Mo substitution at Cu site) sample. With increasing Mo concentration, the current density decreases.

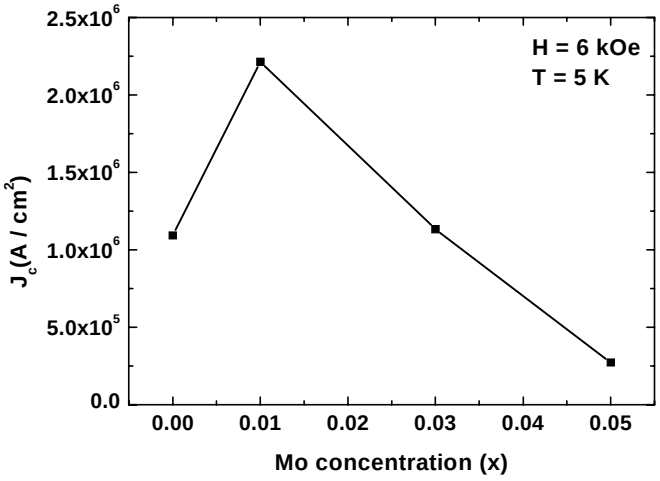

Figure 5.19 Variation of J_c with increasing Mo concentration (x) for $La_{1.5}Nd_{0.5}Ca_1Ba_2(Cu_{1-x}Mo_x)_5O_z$ samples

The studies on Mo-doped RE-123 systems have established the fact that Mo-substitution at low concentrations results in point defects, which act as pinning centers and promote the enhancement of J_c [24].

The comparison of behavior of T_c vs Mo-doping concentration (x) in RE-123 and La-2125 systems has been made in Figure 5.20. Unlike the RE-123 systems, in

which the superconductivity is completely suppressed at around x = 0.08 (~ 8 % of Mo doping), superconductivity is still observed in La-2125 system up to x = 0.10 (~ 10% of Mo doping). The rate of T_c suppression due to Mo-doping in RE-123 superconductors is different than that compared with Mo-doped La-2125 system, which suggest the possibility of different conduction mechanism in La-2125 systems.

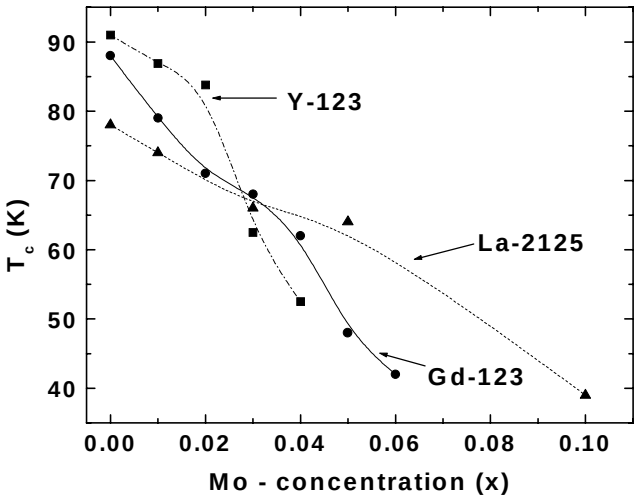

Figure 5.20 Comparison of changes in T_c for RE-123 and La-2125 systems doped with Mo (x)

The behavior of T_c suppression due to Fe substitution at Cu-site in RE-123 superconductors has been explained on the basis of two mechanisms. These are, magnetic pair breaking and hole filling in the CuO_2 planes. In the present course of work, the substitution of $Mo^{>3+}$ at Cu-site in $La_{1.5}Nd_{0.5}Ca_1Ba_2(Cu_{1-x}Mo_x)_5O_z$ system has resulted into the suppression of superconductivity with increasing Mo content, which is shown in Figure 5.15. In order to see whether the T_c suppression due to Mo doping in LaNdCaBCMoO system is due to hole filling or pair breaking mechanism,

the experimental observations on the nature of T_c suppression have been compared with the curve obtained from Abrikosov-Gorkov pair breaking theory [25] of magnetic impurity substitutions in Figure 5.21.

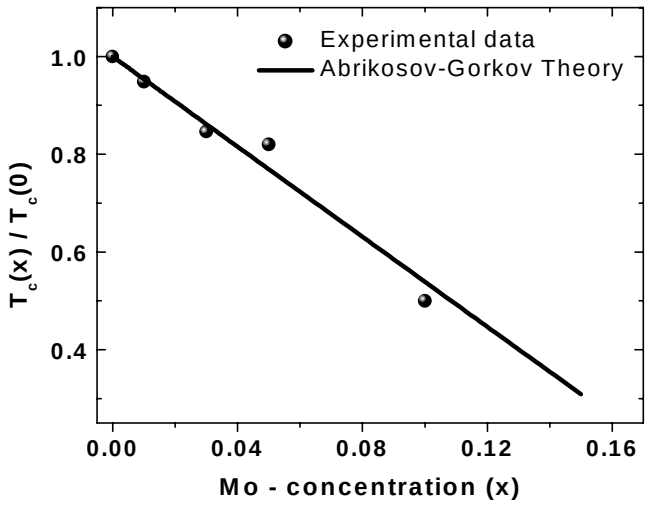

Figure 5.21 Comparison of T_c suppression: experimental data (•) and AG - Theory (—)

The A-G Theory predicts a rapid decrease of T_c, which is given by the universal relation

$$\ln\left[\frac{T_c(x)}{T_c(0)}\right] = \varphi\left(\frac{1}{2}\right) - \varphi\left[\frac{1}{2} + 0.14\left\{\frac{T_c(0)}{T_c(x)}\right\}\right] \qquad \ldots (3)$$

where, x_{cr} corresponds to $T_c = 0$ (complete suppression of superconductivity) and φ is the digamma function. This expression has the linear asymptotic form

$$\frac{T_c(x)}{T_c(0)} = 1 - 0.691\left(\frac{x}{x_{cr}}\right) \qquad \ldots (4)$$

as x → 0 (or small). It is evident from the Figure 5.21 that, there is a agreement between the decrease of normalized T_c value with Mo concentration (x) and it follows the A-G pair breaking model.

This linear dependence of [T_c (x) / T_c (0)] vs. x (for x = 0.00 – 0.15) can be interpreted as evidence for pair breaking mechanism along with hole filling by $Mo^{>3+}$ which suppresses superconductivity in LaNdCaBCMoO system.

CONCLUSIONS

On the basis of the results obtained on the studies on Pr–Ca and Mo–doped La–2125 mixed oxide superconducting systems, the following conclusions are drawn

- Structural studies on Pr–Ca substituted $La_{2-x}Pr_xCa_yBa_2Cu_{4+y}O_z$ samples reveal that, Ca occupies La–site and Ba–site with simultaneous displacement of La on to Ba site.
- The maximum T_c obtained in Pr–Ca doped La–2125 system is ~ 58 K which is lower than, T_c ~ 75 – 78 K obtained for other rare earth dopings like Nd, Dy and Er at La–site which may be correlated to the concentration of holes in CuO_2 sheets having a maximum value of 0.185 (p_{sh}) for La-Pr-2125 as compared to La-Dy-2125 (p_{sh} = 0.235) systems.
- The effect of Ca–addition resulting into the hole doping which increases T_c in Nd/Dy/Er doped La-2125 systems, has been counter balanced by the $Pr^{3+, 4+}$ substitution at La–site which lowers the T_c value probably by hole filling mechanism.
- Structural investigations on Mo doped $La_{1.5}Nd_{0.5}Ca_1Ba_2(Cu_{1-x}Mo_x)_5O_z$ system shows that, the unit cell parameters varies with increasing Mo content due to ionic size effect.
- The decrease in T_c with increasing Mo concentration in LaNdCaBCMoO samples can be explained on the basis of decrease in oxygen content and hence hole concentration in CuO_2 sheets indicating that Mo exists in > 3+ state in the system under investigation, which fills the mobile holes necessary for conduction, thereby suppressing the T_c.

- Comparison of the Mo doping effects, on the T_c suppression in Y - 123, Gd – 123 and La – 2125 systems and to know whether T_c suppression obeys A - G pair breaking theory, shows that, in La–2125 system, Mo–substitution, results into T_c suppression both by hole filling and pair breaking.
- The enhancement of J_c for 1% Mo doping at Cu – site in LaNdCaBCMoO system shows that Mo – substitution at low concentration helps in the enhancement of J_c due to flux pinning effect. The dependence of J_c on applied field for LaNdCaBCMoO samples obeys the flux creep model of field dependence.

SCOPE FOR THE FUTURE WORK

The structural, magnetic and transport studies on La–Dy–2125, Pr–Ca doped La–2125 and Mo–doped La–Nd–2125 systems have revealed many interesting properties which help to understand the cause of superconductivity and mechanism of conduction in these systems.

From the point of view of future work on these systems, it would be interesting to study the structural and superconducting properties of thin films of all the doping concentrations with La–Dy–2125 stoichiometry and study the current density behavior in them. Also, more detailed structural studies on all the La–Dy–2125 samples using low temperature neutron diffraction measurements will help to explore the possibility of structural phase transition if any associated with superconducting transition.

In addition to the above mentioned studies, it will be worthwhile to carry out ERDA (Energy Recoil Dispersive Analysis) measurements on various thin films of La–Dy–2125 samples in order to check the oxygen stability due to ^{16}O, ^{107}Ag or ^{197}Au swift heavy ion irradiation effects. All these future studies on the presently studied La–2125 system will help to understand in more detail the structural and superconducting properties of this newly synthesized mixed oxide superconducting system.

REFERENCES

[1] H. B. Radousky, J. Mater. Res. **7** 1917 (1992)

[2] H. C. I. Kao, F. C. Yu and W. Guan, Physica C **292** 53 (1997)

[3] Y. Xu, W. Guan, Solid State Commun. **80** 105 (1990)

[4] Y. Xu, W. Guan, Phys. Rev. **B 45** 3176 (1992)

[5] J. C. Chen, Y. Xu, M. K. Wu, W. Guan, Phys. Rev **B 53** 5839 (1996)

[6] J. L. Peng, P. Klavins, R. N. Shelton, H. B. Radousky, P. A. Hahn and L. Bernardex, Phys. Rev **B 40** 4517 (1989)

[7] Takashi Ohno, Kuniyuki Koyama, Hiroshi Yasuoka J. Magn. Mag. Mat **177 – 181** 537 (1998)

[8] Kuniyuki Koyama, Takashi Tange, Yasuyuki Kitamura, Takahito Saito and Kiyoshi Mizuno, Physica C **263** 336 (1996)

[9] H. A. Blackstead and J. D. Dow, Phys. Rev **B 54** 6122 (1996)

[10] G. K. Bichile, Smita Deshmukh, D. G. Kuberkar and R. G. Kulkarni Physica C **183** 154 (1991)

[11] D.G.Kuberkar, Nikesh A. Shah, M.V. Subbarao, Amish G. Joshi and R.G. Kulkarni, Mat. Lett. **37** 68 (1998)

[12] D.G.Kuberkar, N.A. Shah, M.R. Gonal, R. Prasad and R.G. Kulkarni J. of Supercond. **13(1)** 37 (2000)

[13] G. K. Bichile, K. M. Jadhav, R. L. Raibagkar, L. Hassan, D. G. Kuberkar and R. G. Kulkarni, Supercond. Sci. Tech. **6** 233 (1993)

[14] G. K. Bichile, K. M. Jadhav, R. L. Raibagkar, J. A. Bhalodia, D. G. Kuberkar and R. G. Kulkarni, Appl. Phys. Lett. **59** 1386 (1991)

[15] E. W. Collings, Applied Superconductivity, Plenum Press, New York (1986)

[16] E. Suard, A. Maignan, V. Cainaert and B. Raveau, Physica C **200** 43 (1992)

[17] R. J. Cava, A. W. Hewat, E. A. Hewat, B. Batlogg, M. Maraczio, K. M. Rabe, J. J. Krajewski, W. F. Peck Jr and L. W. Rupp Jr, Physica C **165** 419 (1990)

[18] I. A. Shaikh, J. A. Bhalodia, G. J. Baldha, D. G. Kuberkar and R. G. Kulkarni, J. Supercond. **7** 853 (1994)

[19] R. G. Kulkarni, Physical and Material properties of high T_c superconductors, Nov. Sci. Publ. (1993) Edited by A. V. Narlikar

[20] K. M. Pansuria, U. S. Joshi, D. G. Kuberkar, G. J. Baldha and R. G. Kulkarni, Solid State Commun. **98** 1095 (1996)

[21] J. A. Bhalodia, I. A. Shaikh, D. G. Kuberkar, G. J. Baldha and R. G. Kulkarni Mater. Res. Bull. **29** 89 (1994)

[22] A. G. Joshi, D. G. Kuberkar, G. J. Baldha and R. G. Kulkarni, Physica C **291** 25 (1997)

[23] S. Rayaprol, Krushna Mavani, C. M. Thaker, D. S. Rana, Keka Chakravorty, S. K. Paranjape, M. Ramanadham, Nilesh Kulkarni and D. G. Kuberkar Pramana – J. of Phys. **58** (No. 5&6), 877 (2002)

[24] D. G. Kuberkar, J. A. Bhalodia, G. J. Baldha, I. A. Shaikh, Utpal Joshi and R. G. Kulkarni, Applied Supercond. **3** 357 (1995)

[25] A. A. Abrikosov and L. P. Gor'kov, JEPT Soviet Phys. **12** 1243 (1961)